Report
R-21-12
September 2022

A combined hydrogeology and radionuclide transport model of the SFL near-field

Diego Sampietro
Elena Abarca
Álvaro Sáinz-García
Jorge Molinero

SVENSK KÄRNBRÄNSLEHANTERING AB

SWEDISH NUCLEAR FUEL
AND WASTE MANAGEMENT CO

Box 3091, SE-169 03 Solna
Phone +46 8 459 84 00
skb.se

SVENSK KÄRNBRÄNSLEHANTERING

ISSN 1402-3091
SKB R-21-12
ID 1925526
September 2022

A combined hydrogeology and radionuclide transport model of the SFL near-field

Diego Sampietro, Elena Abarca,
Álvaro Sáinz-García, Jorge Molinero

Amphos 21 Consulting S.L.

Summary

A research and development model for radionuclide transport in the SFL near-field that consistently couples flow and mass transport to the far-field has been developed. This model includes the discrete fracture network (DFN) of the rock and the porous materials of the engineered barrier system with the objective of improving the system understanding at the interface between the rock and vaults. This interface is critical to improve the quantification of the radionuclide source for the assessment models.

This report includes a simplified model and a vault-scale model of BHA, one of the two vaults of SFL, the planned long-lived low- and intermediate-level waste repository. The simplified model is based on the one reported in Wessely and Shahkarami (2019) and it is used to verify the implementation of the coupling between discrete fractures and continuous porous medium models. The results of the simulations are compared with those obtained with a model where a single fracture is discretized as a 3D porous medium. This model is useful to understand how the release from the vault to the fractured rock changes with flow velocity.

The vault-scale model of BHA is analysed under generic boundary conditions and more realistic boundary conditions extracted from a regional-scale hydrogeological model. The mass flow at the backfill/fracture interface is computed for different inlet Darcy velocities. A modification of the expression proposed by Wessely and Shahkarami (2019) fits the model results over the whole range of groundwater velocity cases. Four regions can be defined according to the main mechanisms limiting the radionuclide release depending on the average groundwater velocity.

Finally, the BHA model is used to evaluate the radionuclide release under the regional groundwater flow field of the study area (Joyce et al. 2019). The transport simulations consider linear sorption in the bentonite backfill and radioactive decay. These simulations describe the release from the waste to the geosphere of four species: ^{36}Cl, one of the main contributors to the dose in SFL, ^{93}Mo as representative of a decaying radionuclide,^{135}Cs as representative of a radionuclide that is strongly sorbed in bentonite, and a non-decaying non-sorbing conservative tracer.

Sammanfattning

En radionuklidtransportmodell har utvecklats för närzonen i det planerade slutförvaret för långlivat låg- och medelaktivt avfall (SFL). Modellen simulerar masstransport mellan förvarssal och berg. Framtagandet av modellen syftar till att förbättra systemförståelsen i gränssnittet mellan berg och förvarssal där berget representeras av ett diskret spricknätverk och barriärerna i förvarssalen representeras av ett poröst medium. Förståelsen för detta gränssnitt är avgörande för att förbättra kvantifieringen av radionuklidutsläpp i säkerhetsanalysen.

Denna rapport omfattar en förenklad modell och en mer detaljerad modell av BHA, en av SFLs två salar. Den förenklade modellen är baserad på den som rapporterades i Wessely och Shahkarami (2019) och används för att verifiera implementeringen av masstransport mellan diskreta spricknätverks-modeller och ekvivalenta kontinuerliga porösa media modeller. Med den förenklade modellen jämförs beräkningar där en enskild spricka representeras som ett 3D poröst medium och som ett diskret 2D objekt. Modellen är användbar för att förstå hur utsläppet från en förvarssal till sprickor i berg påverkas av grundvattenflöden.

Den detaljerade BHA-modellen analyseras för generiska randvillkor och mer realistiskt randvillkor erhållna från en regional hydrogeologisk modell. Masstransporten genom gränssnittet mellan salens återfyllnad och sprickorna i bergssalsväggarna beräknas för olika grundvattenflöden. En modifiering av det uttryck som föreslagits av Wessely och Shahkarami (2019) reproducerar modellresultaten för alla undersökta flödeshastigheter. Fyra flödeshastighetsregimer kan definieras beroende på vilka processer som är utsläppsbegränsande vid olika grundvattenflöden.

Slutligen används den detaljerade BHA-modellen för att utvärdera radionuklidutsläppet för regionala flödesförhållanden (Joyce et al. 2019). Transportsimuleringarna tar hänsyn till linjär sorption i bentonit-återfyllningen och radioaktivt sönderfall. Dessa simuleringar beskriver utsläppet av fyra nuklider från avfallet till berget: ^{36}Cl, en av de viktigaste bidragsgivarna till framtida dosen från SFL, ^{93}Mo som är representativ för en sönderfallande radionuklid, ^{135}Cs som är representativ för en radionuklid som sorberas starkt i bentonit och ett icke-sönderfallande icke-sorberande spårämne.

Contents

1 Introduction

1.1 Background

Possible solutions for the management and disposal of the Swedish long-lived low- and intermediate-level waste were examined in a concept study (Elfwing et al. 2013) for the repository for long-lived waste (SFL). Among the considered alternatives a system was proposed as a basis for further assessment of post-closure safety. According to this concept, SFL is designed as a deep geological repository with two different sections:

- One waste vault, designed with a concrete barrier, BHK, for metallic waste from the nuclear power plants.
- One waste vault, designed with a bentonite barrier, BHA, for the waste from Studsvik Nuclear AB, Cyclife Sweden AB, and AB SVAFO.

A central part of the evaluation of post-closure safety for the proposed repository concept for SFL (SE-SFL) (SKB 2019) is the calculation of the transport of radionuclides from the waste to the accessible environment.

It is proposed that the waste in the vault for the metallic waste (BHK) should be segmented, after which the parts are to be deposited in steel tanks and stabilized with grout. The steel tanks are then to be emplaced in the repository. This section of the repository is to be backfilled with concrete, which acts as a barrier against groundwater flow and contributes to a low diffusion rate and high sorption of many radionuclides. The concrete in the barrier will create an alkaline environment in the repository section, reducing the corrosion rate of the steel and thus limiting the release rate of radionuclides.

The waste in the vault for the legacy waste (BHA) is to be deposited in containers designed for SFL and stabilized with grout. These containers will then be emplaced in the repository. Each section of the vault will be backfilled with bentonite. The bentonite acts as a barrier by limiting the groundwater flow, thereby making diffusion the dominant transport mechanism for radionuclides through the bentonite. Bentonite clay also efficiently filters colloids.

Figure 1-1 shows a schematic representation of the repository design, with the BHA vault in the foreground and the BHK vault in the background.

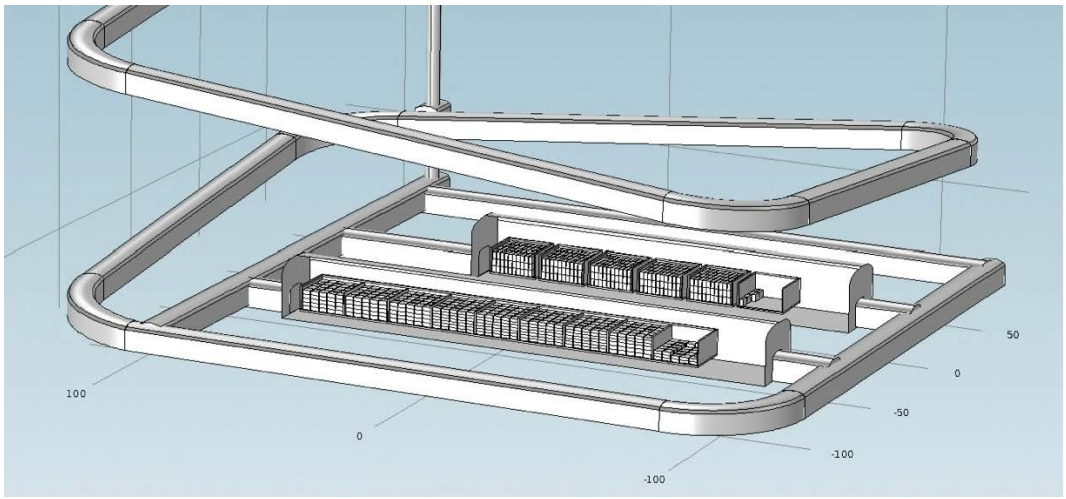

Figure 1-1. *SFL repository design with the BHA vault (front) and the BHK vault (back).*

No site has yet been selected for SFL but site data from the Laxemar site in the Oskarshamn municipality have been used to represent a granitic host rock around the SFL. The area is well characterized with high data density, having been considered as a potential site for the final repository for spent nuclear fuel (SKB 2011). The example location for the SFL repository was selected based on an initial hydrogeological analysis for SE-SFL (Abarca et al. 2016).

1.2 Motivation

The first evaluation of post-closure safety for a proposed repository concept for SFL (SKB 2019) used a radionuclide transport modelling methodology based on the experience from SKB's previous safety assessments (SKB 2010a). Radionuclide transport and dose modelling is performed with a set of mathematical models representing different parts of the repository. The model chain starts with the near-field model that describes the release, transport, and retention of radionuclides in the waste domain and the surrounding engineered barriers. Moreover, the activity release at the waste vault–bedrock interface is calculated and serves as the source function for the far-field hydrological model, which describes the subsequent transport and retention of radionuclides through the bedrock towards the surface.

Therefore, the interface between the fractured rock and the waste vaults is the critical interface between the near-field and the far-field models. This interface controls the distribution over time and space of potentially released radionuclides. The current model development process for radionuclide transport in the near field of SFL (SKB 2019) is a multistep-process (Figure 1-2). Research activities on site characterization and fundamental processes lead to the development of a conceptual model of radionuclide transport from the repository to the geosphere. This conceptual model is then implemented in a series of hydrogeological models that provide input to the assessment models. Thus, the conceptual models are implemented in simplified geometries as a proof of concept focusing on individual processes and generally having a simple geometry. The near-field hydrological models (Abarca et al. 2016, 2019) are repository or vault-scale models with a high resolution in the engineered barrier system and have a heterogeneous equivalent continuous porous media (ECPM) representation of the surrounding rock. The near-field models generate the input to the radionuclide transport simulations performed with compartment models developed for safety assessment (Wessely and Shahkarami 2019). The results from those radionuclide transport simulations are used as the source function for the far-field hydrological model. However, the approaches and assumptions underlying the near-field and far-field models are different (Figure 1-3). The far-field hydrological model (Joyce et al. 2019) integrates the knowledge of the site geology and hydrology at a large-scale and simulates flow in discrete fracture networks (DFN), but the large-scale of these far-field models does not allow them to reproduce the details of the near-field structures.

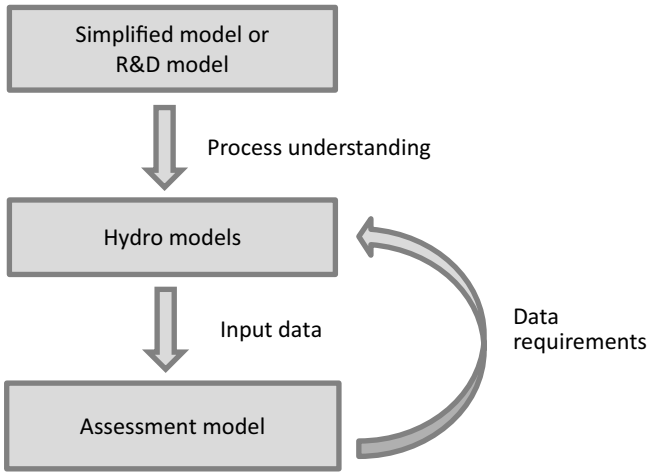

Figure 1-2. *Current model development process for radionuclide transport.*

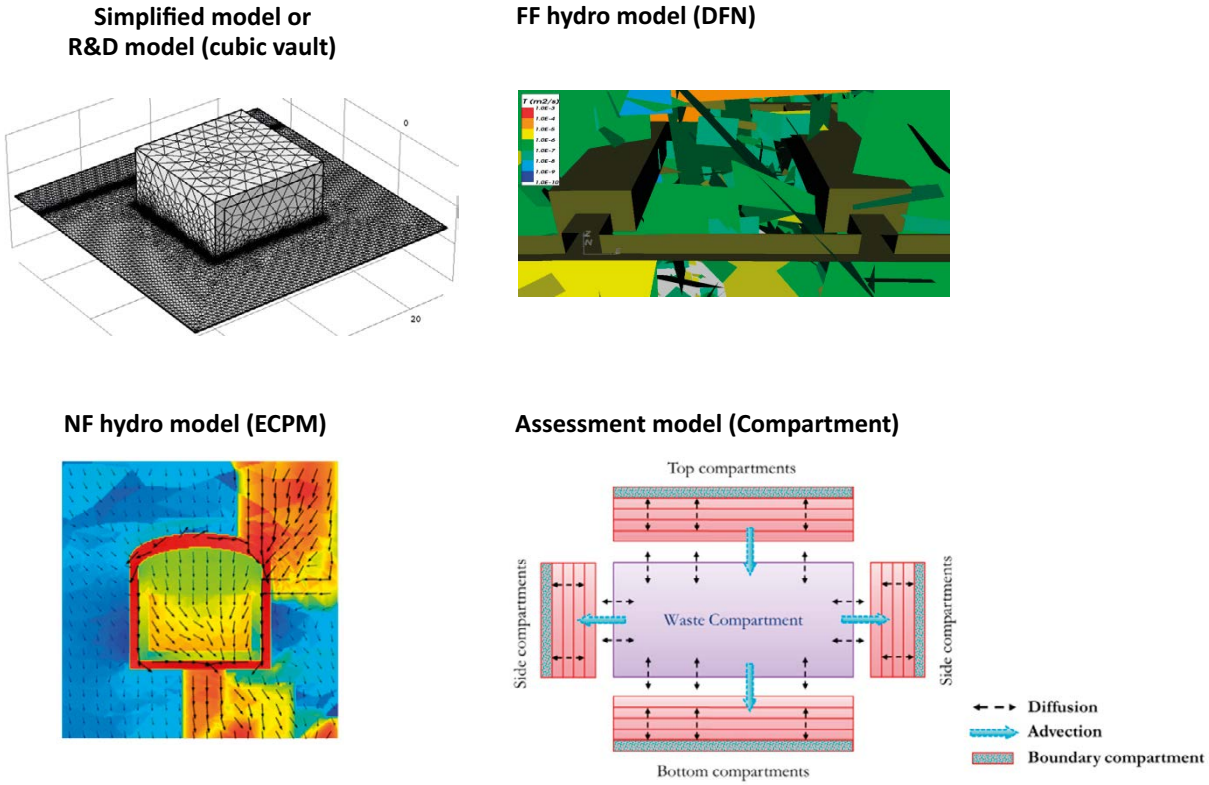

Figure 1-3. *Different concepts behind the multistep-process for simulation radionuclide transport in the near field of SFL (SKB 2019): Simplified or R&D model (Wessely and Shahkarami 2019), Near-Field (NF) hydro (Abarca et al. 2019), Far-Field (FF) hydro (Joyce et al. 2019) and Assessment model (Wessely and Shahkarami 2019).*

Therefore, development efforts are required to improve the understanding and description of the interface between the repository vaults and the fractured rock. The following areas were identified in SE-SFL where there is potential for improvement (SKB 2019):

- The calculations of the diffusive and advective releases of radionuclides rely on different approximations. The diffusive release of radionuclides is calculated using a DFN representation and the advective release is calculated using an ECPM representation
- There is an inconsistent treatment of the tangential and normal components of the flow at the vault-rock interface.

Connecting the discrete fractures in the rock with the continuous representation of the materials in the engineered barriers within the vaults provides a challenge when it comes to modelling groundwater flow and radionuclide transport. Comsol Multiphysics has been used to simulate the groundwater movement in the near field of deep geological repositories (Abarca et al. 2013, 2016, 2019, von Schenck et al. 2015). Recently, the modelling capabilities of Comsol Multiphysics have been developed to allow an extension of the existing repository scale model for near-field hydrology to include:

- Flow in continuous porous media and fracture flow.
- Mass transport in continuous porous media and transport in fractures.

1.3 Objectives

The objective of the project was to develop a model for radionuclide transport in the SFL near-field in Comsol Multiphysics v 5.3a (COMSOL 2017) that consistently couples flow and mass transport to the far-field. This model was to include both the DFN of the fractured rock and the porous materials of the engineered barrier system and was to be able to simulate both the groundwater flow and radionuclide transport. The low permeability rock matrix was not explicitly modelled. The model was required to be fully consistent with the conceptual radionuclide transport models and the far-field hydrological models used in SE-SFL.

A significant part of the work has focussed on improving the system and process understanding at the interface between the rock and vaults and to validating the approximations usually applied at this interface. This interface is critical to defining the radionuclide source for the assessment models. The objective was to develop a near-field model that can calculate parameters relevant for risk assessment such as radionuclide concentrations in fractures and releases of radionuclides. The analysis of the source term from the model should be useful in refining the assessment models.

1.4 Report overview

Chapter 1 presents a short overview of the context of this report and introduces the objectives of the work.

Chapter 2 describes the main modelling approaches for fractured crystalline rock.

Chapter 3 summarizes the modelling strategy and describes the governing equations that were solved, the geometry, boundary and initial conditions that were used and the different outputs presented in the report.

Chapter 4 focuses on the results from a simplified model. This chapter shows the results of groundwater and transport simulations considering a single discrete fracture intersecting a schematic cubic vault. This simplified model is used to test the coupling of the discrete fractures and the continuous porous medium.

Chapter 5 presents the results of a groundwater flow and conservative transport simulation in the near field of the future SFL repository including the discrete fracture network surrounding the repository and the BHA vault. The results are based on generic boundary conditions.

Chapter 6 describes the results of the simulations including the BHA vault with the DFN, using regional groundwater flow conditions, and considering the release of different radionuclides in a transient simulation.

Chapter 7 summarizes the main conclusions presented in chapters 4, 5 and 6.

Appendix A presents a comparison of groundwater flow simulations using the DFN approach and an ECPM. The ECPM is generated using DarcyTools from the same discrete fracture network used in Chapters 5 and 6.

Appendix B presents two benchmark exercises carried out to test the validity of the transport equations for solving transport in porous media of a decay chain of radionuclides subject to linear adsorption.

2 Modelling fractured crystalline rocks

Fractured crystalline rocks can be represented in numerical models following different approaches. The simplest method is to consider a unique material with homogeneous hydraulic and transport properties. This method is known as continuous porous media (CPM) approach. However, this method is not recommended for materials with substantial heterogeneity in their hydraulic and transport properties. To account for such heterogeneity, an improved method, known as the equivalent continuous porous media (ECPM) approach, is more suitable. This method conceptualizes the whole geological media as a porous material with heterogeneous properties. Fractures and deformation zones are represented as high permeable porous materials. This is an extensively used method but has the disadvantage that it requires an extra step to interpret the observed characteristics of the fractured crystalline rock in terms of an ECPM. This step is known as upscaling (Jasinski and Dabrowski 2015). One benefit of this method is that it allows simulation of the groundwater behaviour in larger areas (Joyce et al. 2010a, b, Vidstrand et al. 2010). The ECPM is the most common method used to represent the geosphere in the hydrogeological models used in different studies carried out in the context of deep geological nuclear waste disposal in crystalline fractured rock (Svensson 2001a, Joyce et al. 2010a, b, Vidstrand et al. 2010, Abarca et al. 2019), but the upscaling introduces an extra uncertainty in the modelling process (Renard and de Marsily 1997, Svensson 2001a, b, Follin et al. 2014).

A third method, known as discrete fracture network (DFN) approach, accounts only for the most permeable objects of the geological media, which are the fractures and deformation zones in this case. Some authors (e.g., Flemisch et al. 2018) refer to this approach as a continuous fracture media (CFM) approach. The fractures are usually treated as planar and are represented in the numerical modelling as 2D surfaces inside a 3D domain.

The most comprehensive way of representing the fractured rock is to account explicitly both for the fractures and for the matrix. This is called hybrid method and considers two types of domain: a three-dimensional domain for the porous rock matrix and two-dimensional domains for the discrete fractures or deformation zones. In porous rocks, the matrix, formed by small pores, is represented as a CPM and, in hard crystalline rocks, the matrix is represented as an ECPM resulting from the upscaling of small-scale fracturing which are not feasible to explicitly solve as discrete fractures. The main advantage of the hybrid method is the realistic description of the geology and, therefore, of the flow and transport regime. However, it increases the complexity of the numerical models and the required computational resources. There are some commercial softwares that allow to use the hybrid method in its groundwater flow and transport of dissolved species simulations. Some examples of these softwares are Comsol Multiphysics (COMSOL 2017) or Connectflow (Hartley and Holton 2004). In addition, this type of method has been subject of research in the past years producing innovative numerical methods that uses the hybrid method to model the flow and transport in fractured media. Part of these new numerical methods that uses an hybrid method can be found in Nick and Matthäi (2011), Bazrafkan et al. (2014), Flemisch et al. (2018), Milliotte et al. (2018) and Odsæter et al. (2019).

The following sections focus on two approaches; the discrete fracture network and the equivalent continuous porous media methodologies, which are the ones used in the current report.

2.1 Discrete fracture networks (DFN)

This approach simulates only processes occurring in the fractures. It neglects processes occurring in the rock matrix, which could be a valid assumption for crystalline rocks or materials where the fracture permeability is several orders of magnitude larger than that of the matrix. In more detail, the method consists in conceptualizing each fracture as a surface in the case of 3D models and as a line in the case of 2D models. In general, this method is valid for “Fractured materials” based on the definition given in Berkowitz (2002). However, this assumption is not valid when advection, diffusion or dispersion in the matrix are relevant processes (Bear 1972). Advection and dispersion depend on the movement of the fluid, whereas diffusion is driven by the gradient of concentrations.

Even though the fluid velocity can often be neglected in the matrix, the diffusion of the chemical species in the matrix can be a relevant transport process. Some methods include matrix diffusion in DFN models without explicitly modelling the whole matrix domain. These methods include reacting terms that affect the chemical composition of the fluid in the fracture considering properties of both domains: the surrounding matrix and the fracture. The most common methods are:

- Semi-analytical integrodifferential formulations (Carrera et al. 1998) where the mass transfer to the matrix is represented as the convolution of the concentration with an appropriate memory function over the past history of the system.
- The Multi-Rate Mass Transfer (MRMT) approach (Haggerty and Gorelick 1995), which models the transfer between a mobile region (the fracture) and a finite number of immobile regions (the matrix) as a system of first-order reactions.
- The multi-continuum method, which extends the MRMT method from a finite number of immobile fractions to an infinite number (or a continuum).
- The Continuous Time Random Walk (CTRW)(Berkowitz and Scher 1997, 1998, Dentz and Berkowitz 2003) ,where the movement of solute particles is represented as random walks in time and space. It has been demonstrated that the semi-analytical integrodifferential formulations, the MRMT and the CTRW methods are substantially equivalent (Haggerty et al. 2000, Dentz and Berkowitz 2003, Silva et al. 2009).
- Time Domain Random Walk, which provides a stochastic Lagrangian formalism for including mass transfer to the matrix (Painter et al. 2008).

DFN models generate realistic and accurate groundwater flow results (Jackson et al. 2000). This method has been implemented in different commercial software such as dfnWorks (Hyman et al. 2015), NAPSAC, which now is available within ConnectFlow software (Hartley and Holton 2004) and Fracman (Miller et al. 2001). Solute transport simulations, but not reactive transport, can be undertaken with software packages such as these, although the effect of the matrix on the transport is not implemented in most of them. An example including non-reactive contaminant transport can be found in Hadgu et al. (2017).

The main benefit of this method is the accuracy of the results. However, it becomes inefficient to simulate regional domains with several millions of fractures due to the complex geometrical representation of the fractures (Lei et al. 2017), which implies the generation of very refined meshes and requires high computational resources (Jackson et al. 2000).

2.2 Equivalent continuous porous media (ECPM)

An alternative to the DFN models is the continuum porous medium (CPM) approach. As mentioned before, this type of model represents the whole fractured medium as a continuous porous medium with homogeneous properties. However, for the CPM model to represent an underlying DFN model, it needs to become a heterogeneous model called an equivalent continuous porous medium (ECPM) model. The term equivalent refers to the various properties of the heterogeneous porous medium that should be equivalent to the underlying DFN in terms of flow resistance or transport.

An ECPM model represents equivalent properties of the fractures for each element of the model grid. Properties are anisotropic and differ between elements to represent the underlying structure and properties of a fracture network model (Hartley and Holton 2004). This methodology requires first the generation of a DFN that will serve as a basis for the generation of the ECPM.

These models are computationally feasible for regional-scale calculations. However, such a model requires the upscaling from a DFN to an ECPM, which diminishes the accuracy of the solution compared with the other methods. The various codes available differ in the upscaling method employed to elaborate the ECPM and in the resolution of the resulting ECPM.

The upscaling process has been well studied and tested for hydraulic parameters. There are two main methods to perform upscaling of hydraulic parameters. One method is geometric upscaling, which is the method used by Darcytools (Svensson and Ferry 2010). The second method is hydraulic upscaling (Jackson et al. 2000), used, e.g., in ConnectFlow (Hartley and Holton 2004). Geometric upscaling computes the hydraulic conductivity of a cell as function of the volume of the fractures intersecting the cell volume (Svensson 2001a, b). This method ensures the consistency of the geometry, but not necessarily of the flow characteristics. In contrast, hydraulic upscaling estimates an equivalent hydraulic conductivity of the cell that ensures that the flow crossing the cell volume is the same as the one flowing along the fracture in the DFN model. This method preserves the mass balance in each cell volume (Jackson et al. 2000).

The upscaling of transport parameters involves obtaining equivalent parameters such as porosities, dispersivities and effective diffusivities. Even though the upscaling of transport properties, from the fundamental point of view, has been a subject of recent research, the applicability of these upscaling methods in commercial software is not yet clear. This research is mainly focused on improving the accuracy of the ECPM method to simulate the transport of dissolved species. The Task 9 of the Äspo modelling task force focused on modelling different transport processes such as diffusion and sorption in crystalline fractured rocks (Soler et al. 2022, Trinchero et al. 2020). Some methodologies to upscale the porosity geometrically are presented in Svensson (2001a, b) and Svensson and Ferry (2010).

The generation of heterogeneous property fields is implemented in software such as SGeMS (Remy et al. 2009), geostatistical software that can generate heterogeneous domains, ConnectFlow and DarcyTools. In addition to these, there are other codes that cannot generate ECPM but can perform simulations using it, such as MODFLOW (Harbaugh et al. 2000), FEFLOW (Diersch 2014) and Comsol Multiphysics (COMSOL 2017).

3 Methodology

3.1 Modelling strategy

This report considers two different models:

1. A generic model, hereafter called the simplified model.
2. A vault-scale model of BHA, hereafter called the BHA model. Two types of boundary conditions were applied to this model:
   a. Generic boundary conditions.
   b. Boundary conditions extracted from a regional-scale hydrogeological model.

The simplified model is used to verify the implementation of the groundwater flow representation and the advection-diffusion equation (ADE) in discrete fracture networks. The results of the simulations are compared with the ones obtained with the simplified model where the single fracture is discretized as a 3D porous medium. The model is based on the one reported in Wessely and Shahkarami (2019). This model is also useful to understand how the transport of dissolved species changes with flow velocity.

The vault-scale model of BHA is solved using two types of flow boundary conditions. One set of simplified groundwater flow boundary conditions and a second set of boundary conditions constructed from the pressure field obtained from a regional hydrogeological model. The first set of boundary conditions translates the knowhow obtained in the simplified model to the repository scale model. It includes the implementation of the groundwater flow and ADE representations verified in the simplified model. This model is solved under simple groundwater flow boundary conditions and is used to evaluate the transport of radionuclides and a conservative tracer under a well-defined groundwater flow field. The second repository scale model evaluates the behaviour of the radionuclides and conservative tracer under the regional groundwater flow field of the study area. It focuses on the characteristics of the groundwater flow field and the radionuclide release near the interface between a fracture and the vault.

The transport simulations consider linear sorption and radioactive decay. Three radionuclides are considered:

- ^{36}Cl because it is one of the main contributors to the dose in SFL. It behaves almost as a conservative tracer, i.e., its sorption in bentonite is extremely limited and its decay is slow.
- ^{93}Mo as representative of a decaying radionuclide. It has a relatively short half-life and does not absorb in bentonite.
- ^{135}Cs as representative of a radionuclide that is strongly sorbed in bentonite and has a long half-life.

Table 3-1 shows the half-life of the three radionuclides. The sorption of ^{135}Cs in bentonite is simulated using a linear sorption coefficient. The value of the distribution coefficient, K_d, for caesium in the bentonite used in the modelling is 0.11 m^3/kg.

Table 3-1. Half-life for the different radionuclides considered in the simulations.

Isotope	Half-life (y)
^{36}Cl	301 000
^{93}Mo	4 000
^{135}Cs	2 300 000

3.2 Governing equations

3.2.1 Groundwater flow

Groundwater flow in porous medium

Flow in porous media is described by combining Darcy law (Darcy 1856) with the continuity equation and the equation of state for the pore fluid (Bear 1972). Darcy law is a phenomenological law that relates the specific discharge, or the Darcy velocity, to the hydraulic gradient and the hydraulic conductivity. The resulting equation governs the fluid pressure.

Darcy law states that the fluid velocity is related to the pressure gradient, fluid viscosity and the porous medium properties. The equation can be written as

$$\vec{u} = -\frac{\overleftrightarrow{k}}{\mu}\left(\vec{\nabla}p + \rho g\vec{\nabla}z\right), \tag{3-1}$$

where $\vec{u}$ is the Darcy velocity or the specific discharge vector (m/s), $\overleftrightarrow{k}$ is the permeability of the porous medium (m^2), μ is the fluid dynamic viscosity (Pa·s), p is the fluid pressure (Pa), ρ is the fluid density (kg/m^3), g is the gravitation acceleration (m/s^2) and z (m) refers to the elevation.

The continuity equation for saturated flow in a porous medium is

$$\frac{\partial(\rho\phi)}{\partial t} + \vec{\nabla}\cdot(\rho\vec{u}) = Q_m, \tag{3-2}$$

where, ϕ is the porosity (m^3_{pores}/m^3_{medium}) and Q_m is a mass source term ($kg/m^3/s$). By combining equations (3-1) and (3-2), we obtain the generalized governing equation

$$\frac{\partial(\rho\phi)}{\partial t} + \vec{\nabla}\cdot\left[-\frac{\overleftrightarrow{k}\rho}{\mu}\left(\vec{\nabla}p + \rho g\vec{\nabla}z\right)\right] = Q_m. \tag{3-3}$$

The time derivative can be expanded. By defining porosity and density as function of pressure and applying the chain rule, the first term can be written as

$$\frac{\phi\partial\rho}{\partial t} + \frac{\rho\partial\phi}{\partial t} = \phi\frac{\partial\rho}{\partial p}\frac{\partial p}{\partial t} + \rho\frac{\partial\phi}{\partial p}\frac{\partial p}{\partial t}, \tag{3-4}$$

where the first term is due to compressibility of the fluid in the pores and the second is due to compressibility of the bulk aquifer material. By inserting the definition of fluid and matrix, compressibility, X_f, and X_p, respectively.

$$X_f = \frac{1}{\rho}\frac{\partial\rho}{\partial p} \;\; and \;\; X_p = \frac{1}{1-\phi}\frac{\partial\phi}{\partial p} \tag{3-5}$$

and rearranging, the generalized equation takes the form

$$\rho S\frac{\partial p}{\partial t} + \vec{\nabla}\cdot\left[-\frac{\overleftrightarrow{k}\rho}{\mu}\left(\vec{\nabla}\mathrm{p} + \rho g\vec{\nabla}z\right)\right] = Q_m, \tag{3-6}$$

where the storage coefficient (1/Pa) is $S = \phi X_f + (1-\phi)X_p$, which includes contributions due to compressibility of the bulk aquifer material and the fluid in the pores.

Groundwater flow through discrete fractures

The equation solved in the discrete fractures is a modification of Equation (3-3). This equation is based on a tangential version of the Darcy's law, i.e., the flow is driven by the gradient restricted to the tangential plane of the fracture, ∇_T,

$$\overrightarrow{u_f} = -\frac{\overleftrightarrow{k_f}}{\mu}d_f\left(\overrightarrow{\nabla_T}p + \rho g\overrightarrow{\nabla_T}z\right), \tag{3-7}$$

where u_f is the volume flow rate per unit length in the fracture ($m^3_{water}/m_{fracture}/s$), k_f is the fracture permeability (m^2), d_f is the aperture of the fracture (m). The mean Darcian fluid velocity within

fracture is $v_f = u_f/d_f$. The flow is driven by the pressure gradient tangential to the fracture surface $\overrightarrow{\nabla_T} p$. A single equation for the pressure can be obtained by combining Equation (3-7) with the continuity equation. To restrict the continuity equation to the tangential plane of the fracture, the equation is integrated over the fracture aperture. This gives:

$$d_f \frac{\partial}{\partial t}(\phi_f \rho) + \overrightarrow{\nabla_T} \cdot (\rho \overrightarrow{u_f}) = d_f Q_f, \tag{3-8}$$

where ϕ_f is the fracture porosity (m^3_{pores}/m^3_{medium}), Q_f ($kg/m^3/s$) is the mass source term. In the case of fractures, it is common to speak in terms of transmissivity (T_f). This is the integral of the hydraulic conductivity over the thickness of the fracture. For a fracture with constant hydraulic conductivity K, we obtain

$$\overleftrightarrow{T_f} = \overleftrightarrow{K} \cdot d_f. \tag{3-9}$$

3.2.2 Conservative transport

Transport of diluted species in porous media

The transport of solutes in a variably saturated porous medium is described through the advection diffusion -dispersion equation (ADE) (Bear 1972):

$$(\phi + \rho_b K_{d,i}) \frac{\partial c_i}{\partial t} + \vec{u} \cdot \vec{\nabla} c_i = \vec{\nabla} \cdot \left[\left(\overleftrightarrow{D_D} + \overleftrightarrow{I} D_e \right) \cdot \vec{\nabla} c_i \right] + R_i \tag{3-10}$$

where c_i is the concentration of species i in solution (mol/m^3), u is the Darcy velocity field (m/s), ϕ is the porosity of the rock (m^3/m^3), ρ_b is the dry bulk density (kg/m^3), $K_{d,i}$ (m^3_{water}/kg_{solid}) is the distribution coefficient of the adsorbed species i, D_D is the dispersion tensor (m^2/s), which depends on the longitudinal and transversal dispersivities, I is the identity matrix, D_e (m^2/s) is the effective liquid phase diffusion coefficient and R_i ($mol/m^3/s$) is a sink/source term that describes the production or consumption of species i. The Darcy velocity field is evaluated in the groundwater flow Equation (3-1). For an isotropic porous medium, the dispersion tensor depends on the longitudinal (α_L) and transversal dispersivity (α_T) (m). In a Cartesian coordinate system, the dispersion tensor can be written as

$$\left(\overleftrightarrow{D_D}\right)_{mn} = \alpha_T |\vec{u}| \, \delta_{mn} + (\alpha_L - \alpha_T) \frac{u_m u_n}{|\vec{u}|}, \tag{3-11}$$

where δ_{mn} is the Kronecker delta, $m,n \in \{x,y,z\}$ and u_m is the m:th field component of the Darcy velocity. Dispersivity is a scale-dependent parameter (Gelhar et al. 1992) and, in heterogeneous media, it depends on the correlation scale of heterogeneities (Gelhar and Axness 1983).

The radioactive decay is included in the equation as a source/sink term

$$R_i = -\lambda_i c_i (\phi + \rho_b K_{d,i}) + \lambda_j c_j (\phi + \rho_b K_{d,j}), \tag{3-12}$$

where λ_i (1/s) is the decay constant of species i and the variable j refers to the parent radionuclide of species i (if it is considered in the model).

Transport of diluted species in fractures

The equation to solve the mass transport of a species c_i in a fracture embedded in a porous medium is

$$d_f \left[(\phi + \rho_b K_{d,i}) \frac{\partial c_i}{\partial t} + \overrightarrow{\nabla_T} \cdot \left(\overleftrightarrow{I} D_e \overrightarrow{\nabla_T} c_i \right) + \vec{u} \cdot \overrightarrow{\nabla_T} c_i \right] = d_f R_i + n_o, \tag{3-13}$$

where d_f is the fracture thickness (m), D_e is the effective diffusivity, and n_o corresponds to out-of-plane flux from the neighbouring porous domain ($mol/m^2/s$). $\overrightarrow{\nabla_T}$ is the gradient tangential to the fracture surface. The normal gradient is assumed to be negligible small in comparison to the tangential and therefore:

$$\vec{\nabla} c_i \approx \overrightarrow{\nabla_T} c_i. \tag{3-14}$$

3.2.3 Physics coupling

Groundwater flow coupling

The models presented here consider the coupling between DFN and CPM models (Figure 3-1). In a combined DFN/CPM model the coupling is carried out with boundary conditions that give continuity of pressure or conservation of mass at the interface between the DFN and CPM domains. In our approach, the coupling is carried out by a Cauchy-type boundary condition that ensures mass conservation at the interface.

The Cauchy boundary condition specifies that the mass flow per unit length of the intersection (q^{int}) is proportional to the pressure difference between the pressure in the fracture (p_f) and the pressure in the porous domain (p_m), that is

$$\begin{cases} q_f^{int} = -\alpha(p_m - p_f) \ \ in \ \ L_{int} \\ q_m^{int} = \ \ \alpha(p_m - p_f) \ \ in \ \ L_{int} \end{cases} \tag{3-15}$$

where L_{int} is the length of the intersection where the discrete fracture and the porous media are coupled. q_f^{int} is the flow from the fracture to the porous medium and q_m^{int} is the flow from the porous medium to the fracture. The coefficient of proportionality α (s) is referred as conductance or leakage coefficient in groundwater flow codes. Figure 3-2 shows the behaviour of the boundary condition as a function of α. The Cauchy boundary condition can cover the range between a prescribed pressure boundary condition ($\alpha=\infty$) and a no flow boundary condition ($\alpha = 0$).

For values of α larger than a threshold α_p, the boundary condition behaves as a prescribed pressure (Dirichlet) boundary condition and the flow through the interface is independent of the value of α. For values of α lower than α_p, the boundary condition behaves as a prescribed flow (Neumann) boundary condition. The value of the flow in those cases depends on the value of α. As a result, there is a pressure discontinuity between the discrete fractures and the porous medium at the interface.

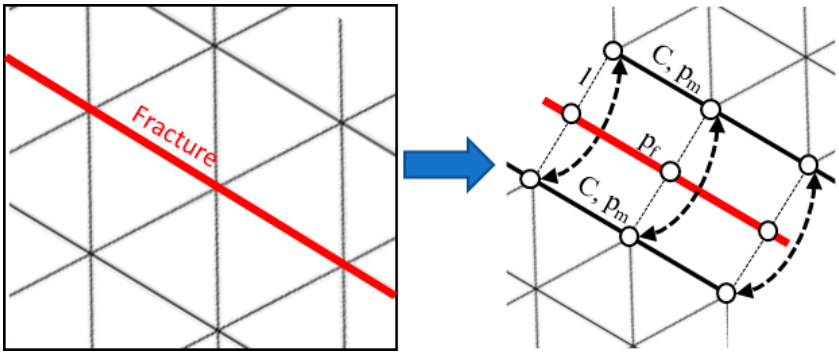

Figure 3-1. *Scheme of a finite element mesh showing the numerical representation of the fracture/matrix exchange term for the groundwater flow and conservative transport coupling.*

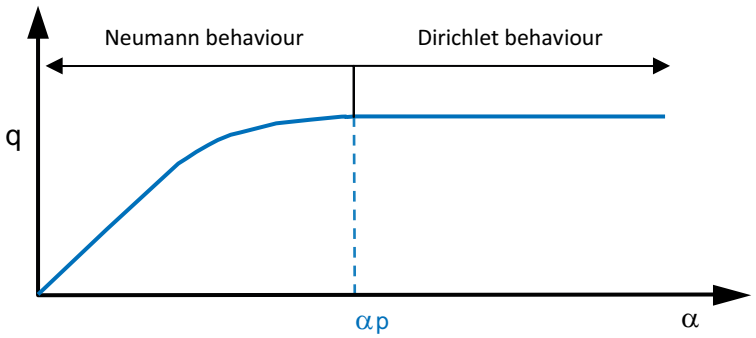

Figure 3-2. *Behaviour of the Cauchy boundary condition as a function of the conductance α. The flow increases with the value of α until a threshold value (α_p) is reached. For values larger than α_p, the flow remains constant and the pressure in the fracture and in the matrix is equal in the shared nodes.*

Assuming that there is a physical interface or layer between the porous medium and the fracture that is not explicitly modelled, the physical meaning of the coefficient of proportionality α can be extracted from Darcy's law integrated over the fracture aperture d_f (m),

$$u_f = -d_f \frac{\rho k_{int}}{\mu} \left|\vec{\nabla}\, p\right| = -d_f \frac{\rho k_{int}}{\mu} \frac{\Delta p}{b_{int}} = -\overbrace{d_f \frac{\rho k_{int}}{\mu b_{int}}}^{\alpha} (p_f - p_m), \tag{3-16}$$

Where ρ is the fluid density (kg/m^3), k_{int} (m^2) is the permeability of the interface between the matrix and the fracture and b_{int} the thickness of the layer between the porous medium and the fracture. The flow exchanged at the boundary depends on the properties of the interface. Thus, α is proportional to the permeability of the interface between the porous medium and the fracture, k_{int}, and inversely proportional to the thickness of the layer, b_{int}.

In the applications presented in this report, the α value is selected so that the boundary condition behaves as a Dirichlet boundary condition. That way the boundary condition provides both conservation of mass and continuity of pressure at the interface between the DFN and CPM domains. The boundary condition is applied over the intersections between the discrete fractures and the porous domain (Figure 3-3).

Conservative transport coupling

In a similar way, the coupling between the transport of species in solution in the fractures and the transport of diluted species in the porous medium ensures mass conservation. The solute mass flow per unit length of intersection, (mol/m/s) entering the fracture, j_f^{int}, equals the solute mass flow per unit length of intersection leaving the porous medium, j_m^{int}, or vice versa.

$$j_f^{int} + j_m^{int} = 0, \tag{3-17}$$

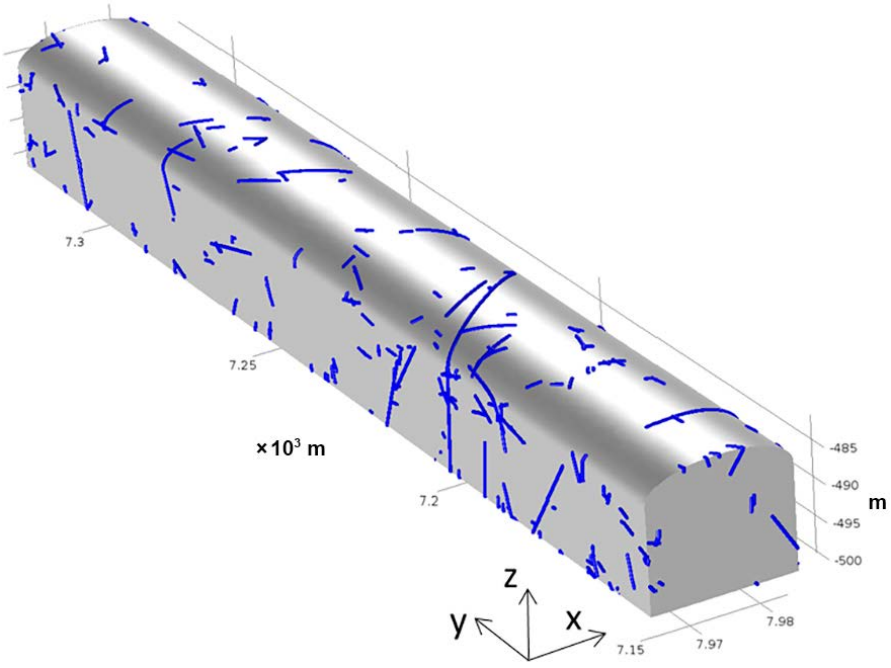

Figure 3-3. *Blue lines showing the intersection between the fractures and the BHA vault.*

The coupling is carried out using a Cauchy-type boundary condition that specifies that the solute mass flow per unit length of intersection ($j_{f,m}^{int}$) is proportional to the concentration difference between the concentration in the fracture (c_f) and the concentration in the porous domain (c_m), that is

$$\begin{cases} j_f^{int} = -\beta\left(c_m - c_f\right) \ in \ L_{int} \\ j_m^{int} = \ \ \beta\left(c_m - c_f\right) in \ L_{int} \end{cases}, \tag{3-18}$$

where L_{int} is the length of the intersection where the discrete fracture and the porous media are coupled. The proportionality coefficient β (m^2/s) is the mass transfer coefficient. There are different expressions for β in the literature. Here, the physical meaning of β can be extracted from Fick's law integrated over the fracture aperture d_f and applied to the length of the intersection between the porous medium and the discrete fractures L_{int}

$$j^{int} = -d_f D_{int} \left|\overrightarrow{\nabla_{\mathrm{n}}} c\right| = \ -d_f D_{int} \frac{\Delta c}{b_{int}} = -\frac{\overbrace{d_f D_{int}}^{\beta}}{b_{int}} \left(c_f - c_m\right), \tag{3-19}$$

β is proportional to the diffusion coefficient through the interface between the porous medium and the fracture, D_{int}, proportional to the fracture aperture d_f and inversely proportional to the thickness of the layer, b_{int}.

As in the groundwater flow coupling, if this parameter is large enough, the coupled set of equations will yield similar concentration values for the fracture and the porous medium. In that case, the Cauchy or mixed boundary condition behaves as a Dirichlet-type boundary condition. Then, the mass exchange between the matrix and fracture is well defined and does not depend on the value of β. However, if β is lower than a given threshold, the exchange term behaves as a Neumann-type boundary condition. Then, the mass exchange between the two domains strongly depends on β and the tracer concentrations in the porous domain and at the fracture nodes diverge, i.e., there is no concentration continuity at the fracture-matrix interface. The mass exchange is bounded between zero, when β is zero and the maximum mass exchange value, reached when β tends to infinity.

Even though the boundary allows for the full range of β values, for the applications presented in this work, the value of β is selected so that the boundary condition behaves as a Dirichlet boundary condition. Thus, the boundary condition provides both conservation of mass and continuity of concentration at the interface between the DFN and CPM domains.

3.3 Description of the simplified model

The simplified model is based on the model reported in Wessely and Shahkarami (2019). This model was used to increase the understanding of the behaviour of the radionuclides released from the waste. It represents a simplified deep geological nuclear repository with a low permeable engineered barrier surrounding the nuclear waste. The repository is intersected by a permeable fracture representing a fracture in the host rock. The fracture is treated in Wessely and Shahkarami (2019) as a 3D domain, therefore, there is a continuum between the repository and the 3D fracture. For this application, the dimensions of the model have been modified to account for fractures that do not have a large extent laterally. For that reason, the model presented in Wessely and Shahkarami (2019) was modified and re-run with the new fracture dimensions.

In addition, we reproduce the results of the continuum model with a combined fracture/CPM model using the flow and transport coupling described in Section 3.2.3. The simplified repository is represented by a CPM and the fracture is represented as a 2D feature that intersects the CPM. One objective of this exercise was to test the coupling of a discrete fracture and the CPM domain by comparing the results with those of a fully coupled model with a fracture treated as a 3D domain.

3.3.1 Geometry and materials

The model represents a cubic vault composed of a homogeneous waste domain surrounded by a low permeability backfill acting as engineered barrier. The surrounding rock is an impermeable rock crossed by a square horizontal fracture of high permeability that intersects the vault (Figure 3-4). Assuming

that the groundwater flow through the rock domain is restricted to fractured zones, the model includes explicitly only the horizontal fracture as a 2D feature. The aperture of the fracture is 0.1 m to be consistent with the dimensions of 3D representation of the fracture in Wessely and Shahkarami (2019). Thus, the model is formed by three domains: the waste compartment, the low permeability backfill and a single 2D fracture. The dimensions of the simplified model are reported in Table 3-2. The cube has its corner located at the centre of coordinates and is intersected by a horizontal planar fracture.

Table 3-2. Dimensions of the simplified model.

Domain	Height (m)	Width (m)	Length (m)
Waste	10	10	10
Backfill	15	15	15
Fracture	-	17	27

Table 3-3 lists the values of the flow and transport parameters for the three domains. The density of the fluid is set to 1 000 kg/m^3. In this case, the K_d value used for the caesium tracer in the bentonite is 0.11 m^3/kg and the dry bulk density of the bentonite is 1 570 kg/m^3.

Table 3-3. Hydraulic and transport parameters of the different domains involved in the simplified model. Parameters taken from Wessely and Shahkarami (2019).

Domain	Hydraulic conductivity (m/s)	Transmissivity (m^2/s)	Diffusivity (m^2/s)	Porosity (-)
Waste	1.0×10^{-7}	-	1.0×10^{-9}	1
Backfill	1.0×10^{-10}	-	1.0×10^{-10}	1
Fracture	-	1.0×10^{-5}	2.5×10^{-10}	0.25

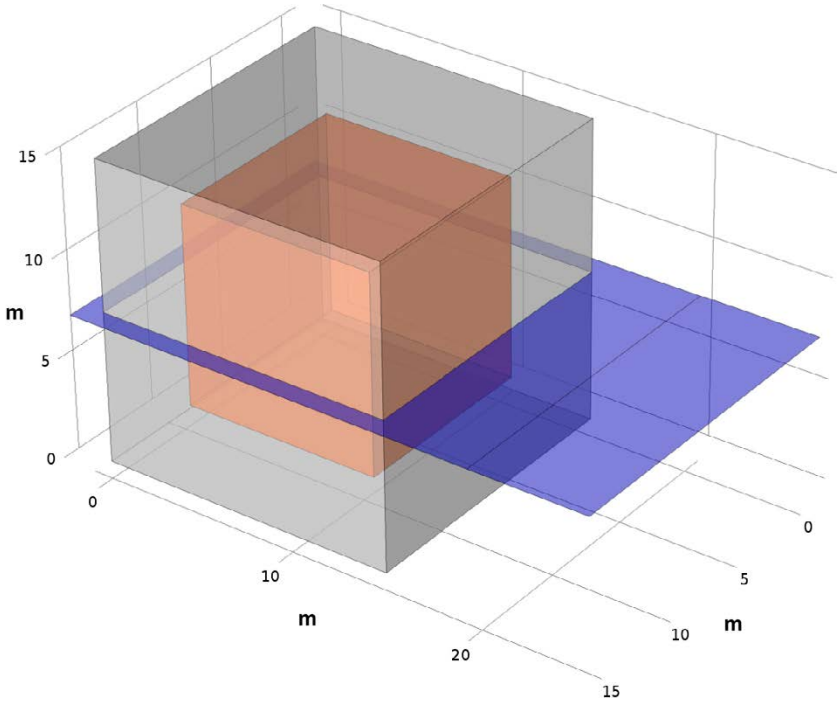

Figure 3-4. *Geometry of the simplified model. The cube is formed by the waste domain (in orange) surrounded by the low permeability backfill (in grey). The discrete horizontal fracture is shown in blue.*

3.3.2 Spatial and temporal discretization

The discrete fracture was discretized using 51 256 triangular elements and the vault using 333 897 tetrahedral elements. Figure 3-5 shows the finite element mesh used in the simulation.

The sensitivity of the solution to the spatial discretization was analysed by performing the same simulations as described in the following Section 3.3.3 with different meshes and comparing the results of the mass flow across the backfill/fracture interface (Figure 3-6). The mesh size was reduced until the total mass flow through the backfill/fracture interface had converged to three significative digits.

For the transient transport simulations, the time step is adaptative according to the algorithm implemented in Comsol to ensure that the Courant criterion is met.

3.3.3 Boundary conditions

Groundwater flow

The groundwater flow in the simplified model is solved in steady state conditions. The model imposes a prescribed head equal to 0 at the outlet boundary of the fracture (red line in Figure 3-7) and a prescribed flow boundary condition at the inlet boundary of the fracture (blue line in Figure 3-7), as described in Wessely and Shahkarami (2019). The prescribed flow boundary condition forces flow into the repository.

The expressions of the boundary conditions are

$$\begin{cases} h(x, y_1) = 0 \\ -n \cdot \rho u(x, y_0) = \rho U_o \end{cases}, \tag{3-20}$$

where h is the hydraulic head and U_0 is the inlet Darcy velocity (m/s). y_0 and y_1 refer to the coordinates where the boundary conditions are assigned, which in this case are equal to 26 and −1 respectively.

The model is solved for a set of inlet Darcy velocities at the fracture: 1×10^{-13}, 1×10^{-12}, 1×10^{-11}, 1×10^{-10}, 1×10^{-9}, 1×10^{-8}, 1×10^{-7}, 1×10^{-6}, 1×10^{-5} and 1×10^{-4} m/s. The transport velocity can be calculated by dividing the Darcy velocity by the fracture porosity (0.25, see Table 3-3).

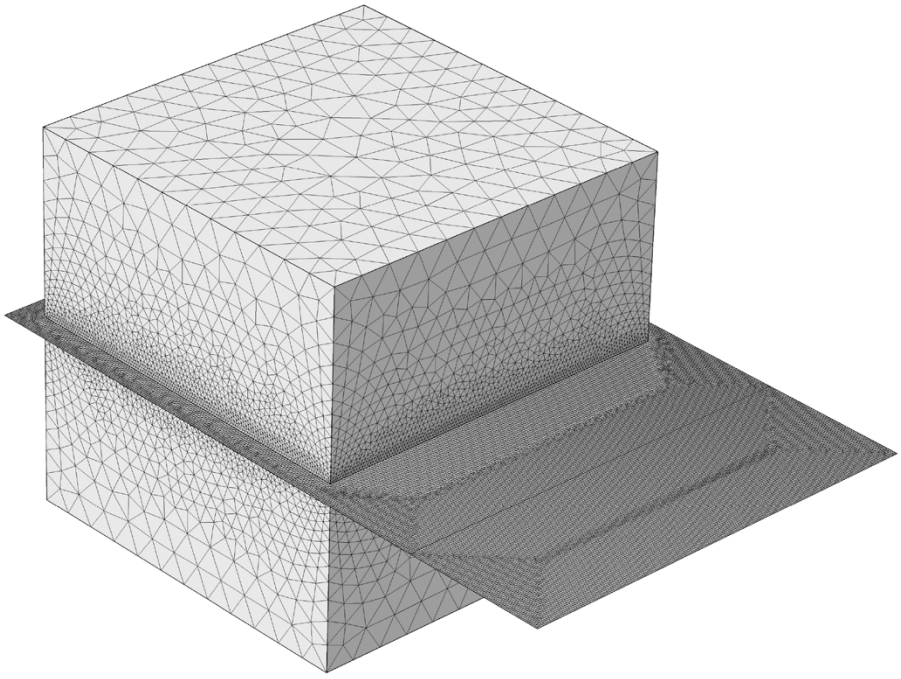

Figure 3-5. *Finite element mesh formed by tetrahedral and triangular elements. Tetrahedral elements are used to discretize the porous materials and triangles for the discrete fracture.*

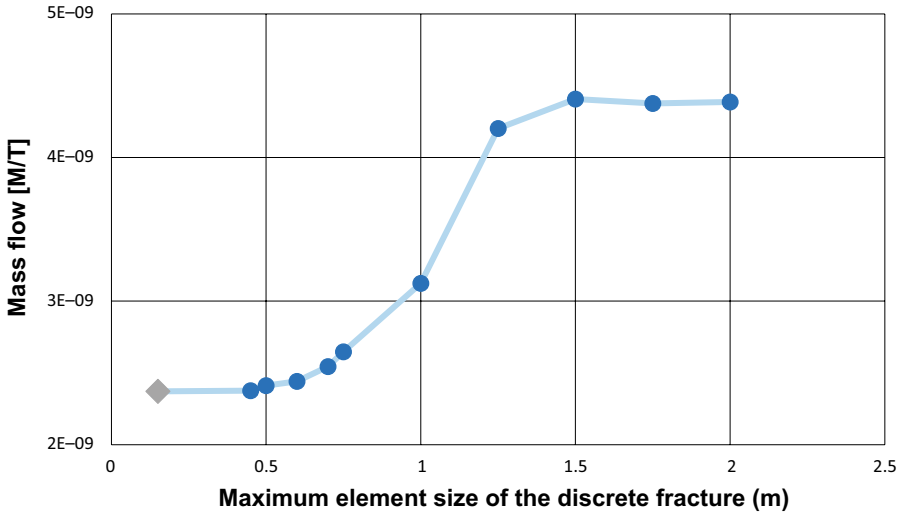

Figure 3-6. *Mass flow across the backfill/fracture intersection for different mesh discretization. The grey diamond shows the final mesh used in the simulations.*

Transport

The transport of a conservative, non-decaying tracer and several radionuclides is solved both under steady and transient states:

- In the steady state simulation, the radionuclides and tracer are released from the waste. The source of radionuclides is modelled using a Dirichlet boundary condition. A normalized concentration equal to 1 is imposed at the interface waste/backfill (orange surface in Figure 3-7). A normalized concentration equal to 0 is imposed both at the fracture inlet and outlet.
- The transient simulation considers a normalized initial concentration of tracer and radionuclides equal to 1 in the waste domain (Figure 3-7) and a concentration equal to 0 mol/m^3 is imposed both at the fracture inlet and outlet.

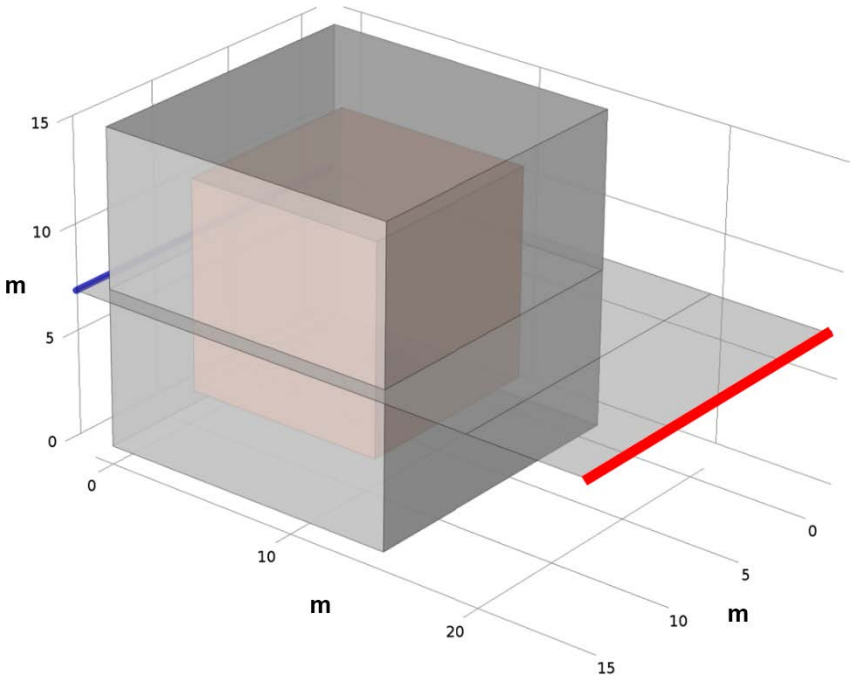

Figure 3-7. *Model domain showing the location of the flow and transport boundary conditions. The waste/backfill interface coloured in orange, the fracture inflow and outflow boundary conditions are marked with blue and red line, respectively.*

3.4 Description of the BHA model

Two storage vaults are planned for SFL: one vault for legacy waste (BHA), and one vault for the metallic waste from the nuclear power plants (BHK). Here, we only consider the BHA vault. Waste containers are emplaced in concrete structures that serve as radiation barriers during operation. The BHA vault will be backfilled with bentonite. The present work uses the same layout of the BHA that was used for the initial modelling of the SFL near-field hydrology (Abarca et al. 2016, 2019).

The model is formed by the BHA vault surrounded by its crystalline host rock. The BHA is located in the middle of a cube of 400 meters edge length representing the host rock.

3.4.1 Geometry and material properties

Engineered structures (BHA vault)

Apart from the host rock, the BHA vault is the only structure in the model. The access tunnels and other waste vaults are excluded for simplicity. The model simplifies the vault as a structure formed by two materials: the waste and the bentonite backfill. Figure 3-8 shows a schematic cross-section of BHA showing the waste domain composed of the waste packages, grout and concrete structure surrounded by the bentonite backfill.

Figure 3-9 shows the geometry of the BHA vault implemented in the model. The vault is formed by two domains: One is the bentonite backfill and the second material considered is a homogenised waste which is surrounded by the backfill. The values of the hydraulic conductivity, permeability, effective diffusivity, and porosity of the vault materials are given in Table 3-4.

Table 3-4. Repository material properties for the base case calculation.

Description	Material	K (m/s)	k (m^2)*	D_e (m^2/s)	ϕ	Reference
Waste domain	Homogenized	1.0×10^{-7}	2.0×10^{-14}	3.5×10^{-10}	0.30	(SKB 2014))
BHA vault backfill	Bentonite	1.0×10^{-13}	2.0×10^{-20}	1.4×10^{-10}	0.43	(SKB 2010b)

* Calculated assuming ρ = 1 000 kg/m^3 and μ = 0.002 Pa · s.

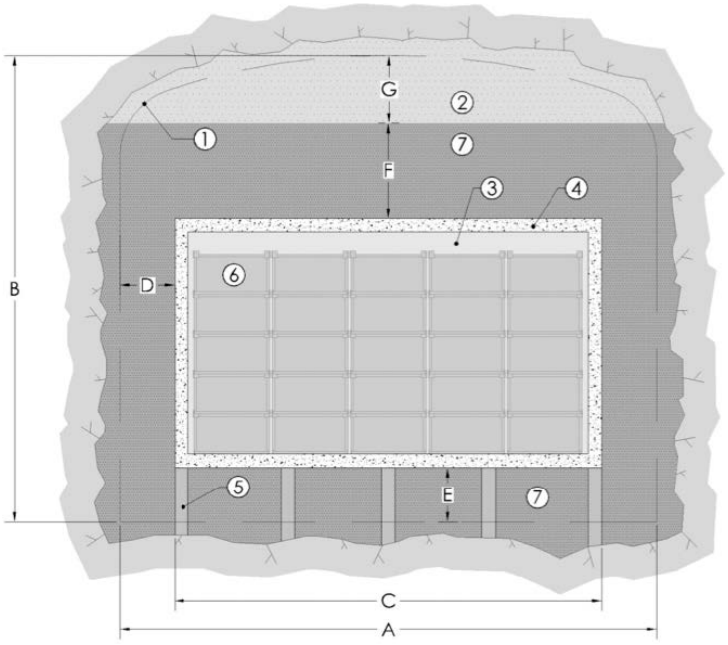

Figure 3-8. *Schematic cross-sectional layout of BHA (from Elfwing et al. 2013). Legend: 1.) Theoretical tunnel contour. 2) Bentonite pellets. 3) Grout. 4) Concrete structure (0.5 m). 5) Granite pillars. 6) Waste packages. 7) Bentonite blocks. Approximate dimensions: A = 20.6 m, B = 18.5 m, C = 16 m, D = 2.3 m, E = 2.4 m, F = 4 m, G = 3.7 m.*

The bentonite backfill acts as a barrier to the groundwater flow due to its low permeability, and to the release of some radionuclides due to its high sorption capacity. In this study, we consider three different radionuclides: ^{36}Cl, ^{93}Mo and ^{135}Cs. The bentonite is assumed to not have sorption capacity for the chloride and molybdenum but has a high retention capacity for ^{135}Cs.

Rock properties

Geological data from Laxemar were used to represent the host rock surrounding the modelled repository. This is a well-studied area because it was considered as a potential area for the construction of the Swedish repository for spent nuclear fuel (SFK). This area belongs to a geological unit called the Transscandinavian Igneous Belt, which is formed by igneous intrusive rocks affected by different deformation structures from ductile to brittle generated during multiple strain events. Highly permeable materials in this area are associated to the deformation zones, which have been conceptualized in several studies as discrete fractures (Joyce et al. 2010a, b, Vidstrand et al. 2010). The models presented in this report represent the host-rock using a subset of the discrete fracture network reported in Joyce et al. (2019) and generated stochastically based on comparisons with Posiva Flow Log (PFL) tests.

The DFN includes both deterministic deformation zones and stochastic fractures. A subset of fractures was produced by SKB using a script (CF2DT2COMSOL). The script reads the DFN generated in ConnectFlow and imports it into DarcyTools where a filtering is carried out to remove internal dead-end clusters. The dead-end clusters connected either to the BHA or to the outer cube of 400 meters edge length were not filtered out. As a result, the resulting DFN contains the connected fractures plus dead-end fractures connected to the BHA and the outer box boundary. The equivalent radii of the fractures range from decimetres to hundreds of meters. The resulting DFN is stored in an external file that is read in a Comsol application to generate the Comsol geometry (Figure 3-10). Two deformation zones from the deformation zone model and 7 084 stochastic fractures were included in the fab file. Originally, the stochastic fractures were squares but they were divided into two triangles forming each square. This results approximately in 14 100 geometrical entities. The final Comsol geometry (Figure 3-10) removes the fractures outside a box of 400 x 400 x 400 m^3. Only a small part of one of the deformation zones fits into the box and it is located in the lowermost +y corner. The final model in Comsol is formed by a total of 7 125 rectangular fractures with sizes that go from decimetres to hundreds of meters. The intersection between the BHA and the fractures is illustrated, showing the complexity of contacts between the vault and the rock fractures that intersect the engineered structure (Figure 3-9).

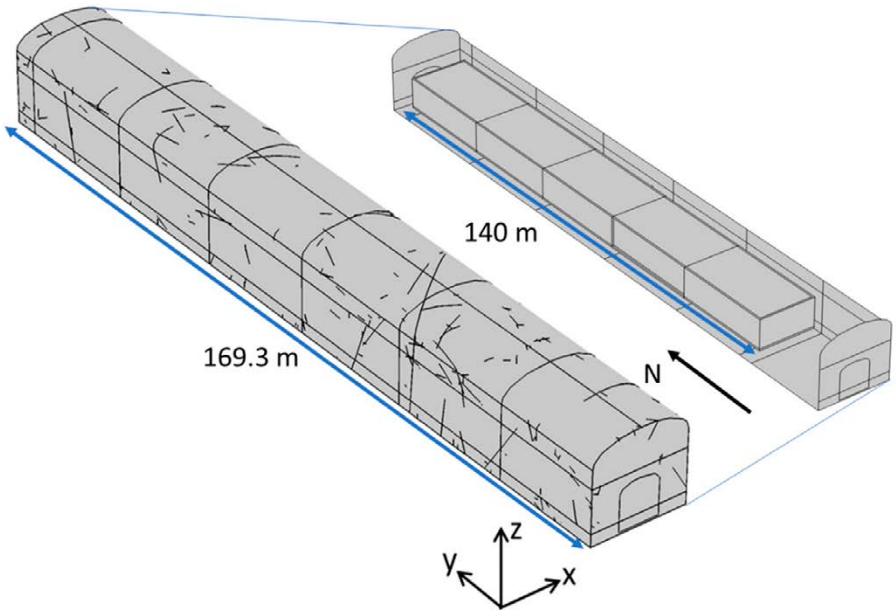

Figure 3-9. *BHA vault as is implemented in the Comsol model. The illustration shows the lines generated by the intersection between the fractures and the outer surface of BHA.*

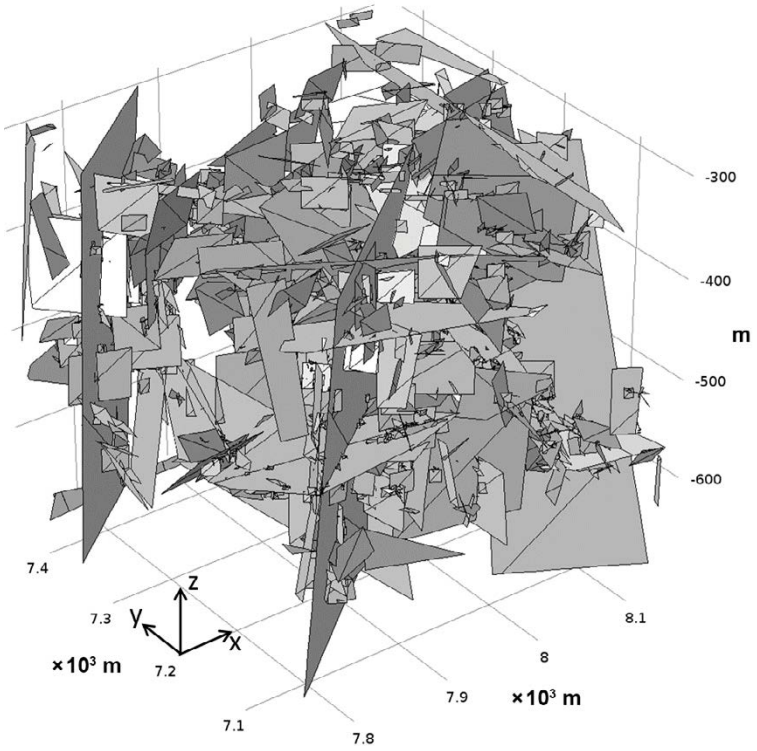

Figure 3-10. *Model domain with the DFN of the fractures connected to the BHA vault imported into Comsol. The model considers a cubic domain of 400 meters length on each side with the BHA vault placed in the centre of the domain. The coordinate corresponds with the local system presented in Abarca et al. (2019).*

The DFN is imported together with the hydraulic properties for each fracture: hydraulic transmissivity, aperture and storativity. Figure 3-11 and Figure 3-12 show the transmissivity (m^2/s) of the fractures on a logarithmic scale and their apertures, respectively.

The transmissivity of the stochastic fractures varies between 1.66×10^{-10} and 2.33×10^{-5} m^2/s. The figure also shows that the density of fractures decreases with depth. The aperture of the deformation zone in the modelled area is 0.15 meter. The range of apertures varies from 8×10^{-5} to 9×10^{-3} m in the stochastic fractures. The relation between transmissivity and aperture for the stochastic factures is the one reported in Hjerne et al. (2010):

$$a = 0.67 \cdot T^{0.4}, \quad (3\text{-}21)$$

where T is transmissivity (m^2/s) and a is the fracture aperture (m).

The properties of the deformation zones are calculated with a depth-dependent stochastic trend conditioned on borehole measurements (Joyce at al 2019). The transmissivity of the only deformation zone included in the model domain, and located at a depth of about 700 m, is 3.76×10^{-8} m^2/s. This moderate value is consistent with some measured transmissivities (based on PFL-f) in borehole KLX11A (Figure 2-11 in Joyce et al. 2010a). This deformation zone is restricted to a bottom corner of the domain. Therefore, its role in the flow at the interface vault/rock would be minimal.

The properties of the deformation zones are calculated with a depth-dependent stochastic trend conditions on borehole measurements with a depth trend (Figure 3-1 in Joyce et al. 2019). The range of T values is large, but the moderate value is consistent with some measured transmissivities (based on PFL-f) in the fracture domain HRD_W (Figure 2-11 in Joyce et al. 2010a), where the BHA is located.

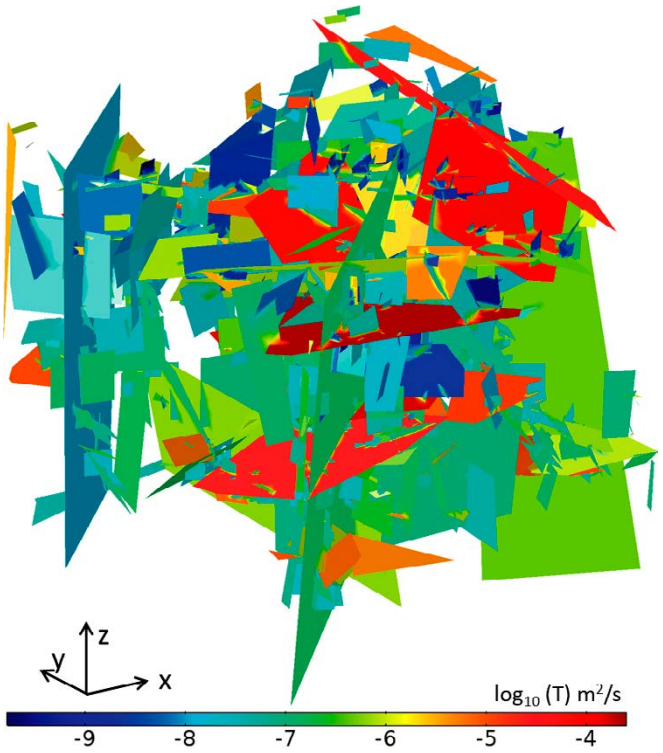

Figure 3-11. *Transmissivity of the discrete fractures considered in the model (logarithmic scale).*

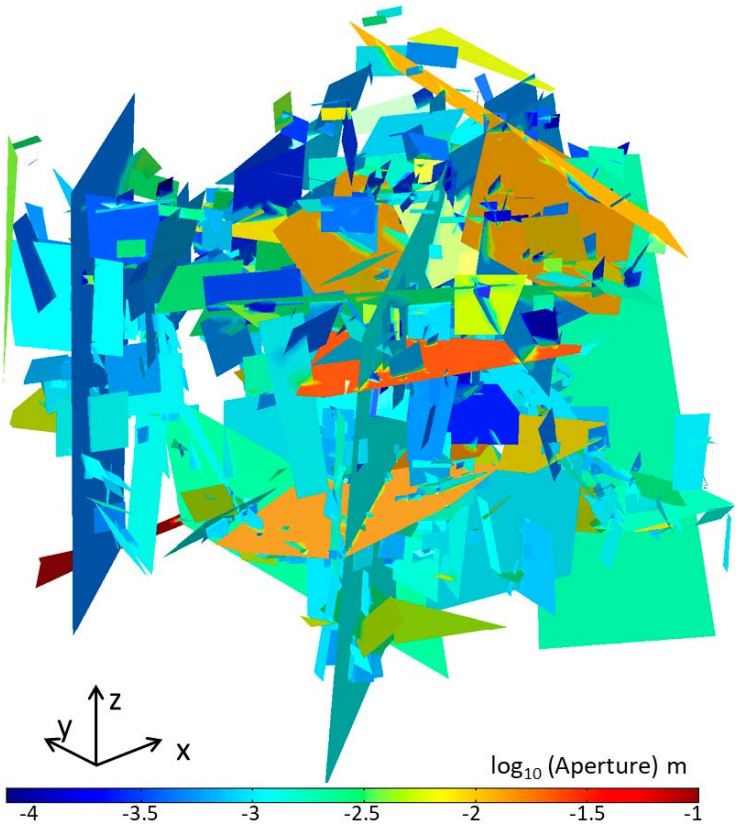

Figure 3-12. *Logarithm of the aperture for the discrete fracture network considered in the model.*

Groundwater density and viscosity

The chemical composition of the natural groundwater of the Laxemar area is well described in Laaksoharju et al. (2009). The authors distinguish 5 different types of waters based on depth. The fluid salinity increases with depth (Laaksoharju et al. 2009). For that reason, the density ranges between 1 001.17 kg/m^3 and 1 014.82 kg/m^3 in the domain of our model (Figure 3-13). The higher density is found in a bottom corner of the domain (-x +y -z corner). For the simulations carried out in this work, the salinity effects are disregarded given that the high density is restricted to a corner and that the variation of density is not large. The simulations performed with the near-field model assume a constant fluid density equal to 1 004 kg/m^3, which is the density value at repository depth.

The water dynamic viscosity field from the ConnectFlow model in Joyce et al. (2019) presents values that range between 0.0017 and 0.002 Pa·s in the BHA model domain. For the simulations performed in this work, a value of 0.002 Pa·s was used. This value was also used in Abarca et al. (2016, 2019).

3.4.2 Spatial and temporal discretization

Figure 3-14 shows the finite element mesh used in the simulation with the DFN. The discrete fractures have been discretized using triangular elements and the BHA vault using tetrahedra. The sensitivity of the solution to the spatial discretization has been evaluated by repeating simulations using different levels of discretization to ensure that the results do not vary with the mesh. The mesh size was reduced until the groundwater flow through the domain varied less than 1 %.

For the transient transport simulations, the time step was adaptive according to the algorithm implemented in Comsol to ensure that the Courant criterion was met.

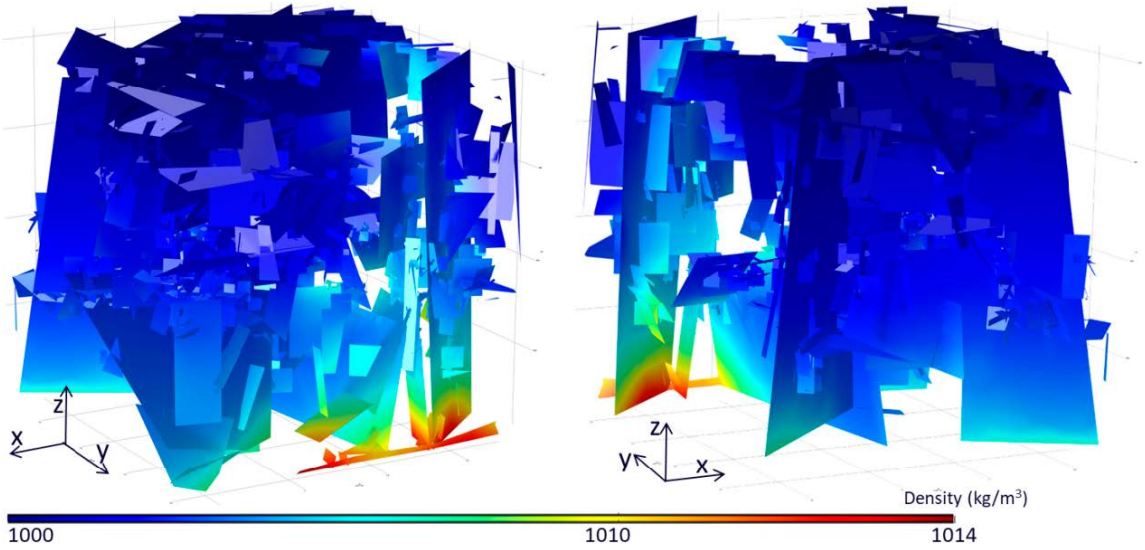

Figure 3-13. *Density field resulting from the simulation by Joyce et al. (2019) imported over the current BHA model domain. The two plots show two different perspectives.*

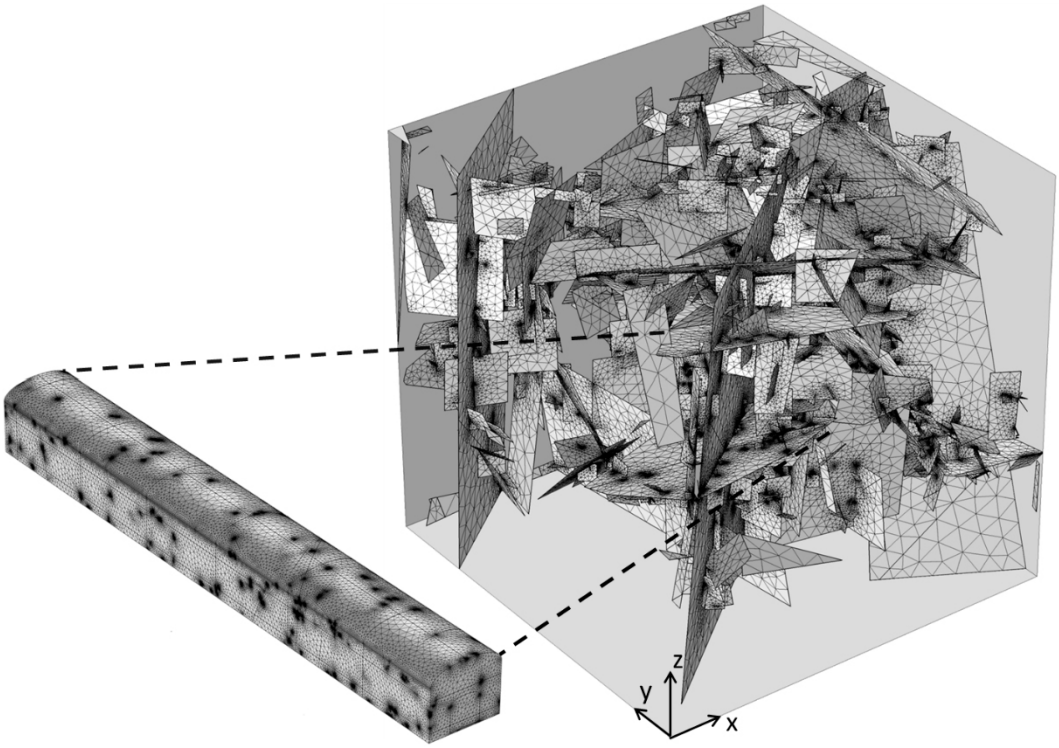

Figure 3-14. *Finite element mesh used in the model. The mesh is formed by 1 801 850 triangular elements for the fractures and 1 963 025 tetrahedral elements for the porous medium.*

3.4.3 Boundary and initial conditions

Groundwater flow

Two sets of steady state flow simulations were considered for the repository scale model depending on the applied groundwater flow boundary conditions:

- **BHA model with generic boundary conditions**: This applied generic boundary conditions that result in a directional groundwater flow field (e.g., prescribed pressure gradients between the northern/southern boundaries and no flow at the rest of the boundaries).
- **BHA model with boundary conditions from the regional model**: The results of the regional hydrogeological simulation performed by Joyce et al. (2019) using ConnectFlow were imposed as boundary conditions. The regional hydrogeological simulation reproduces the groundwater flow field in the Laxemar area (Sweden). The residual pressure from the regional simulation was imported into Comsol and a linear interpolation was performed over the finite-element mesh of the Comsol model in order to assign the pressure field. The imported residual pressure from ConnectFlow, p_{CF} (Pa), was converted into total pressure by adding the gravitational term, assuming a reference density of ρ_0 = 1 001.74 kg/m^3,

  $$p^* = p_{CF} - \rho_0 g z, \tag{3-22}$$

  Note that z, the vertical coordinate, is negative in the modelled area. The pressure p^* is used to define the initial pressure in the model domain and to prescribe pressure at the model boundaries. The pressure at the fracture outer edges (Figure 3-15) is specified in Comsol using a Dirichlet boundary condition

  $$p = p^*. \tag{3-23}$$

The regional model (Joyce et al. 2019) simulates coupled groundwater flow and solute transport, with varying fluid density. However, the simulations performed with Comsol assumed a constant fluid density equal to 1 004 kg/m^3 and a viscosity value of 0.002 Pa·s (Section 3.4.1).

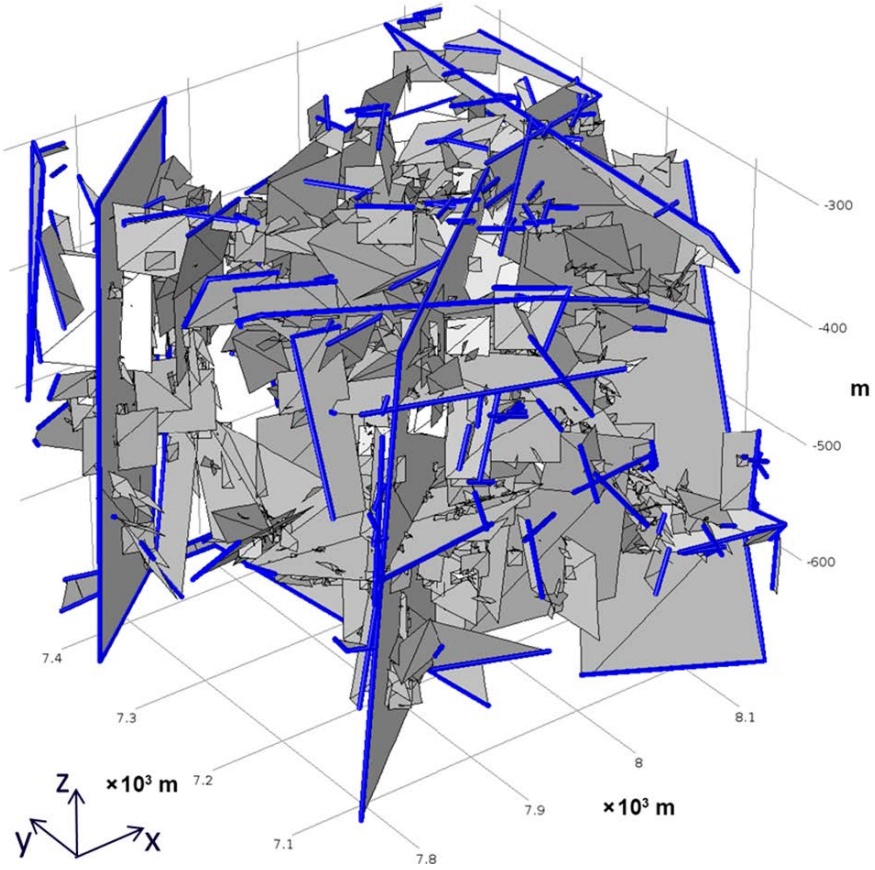

Figure 3-15. *Outer fracture edges where the boundary conditions are applied.*

Transport

Radionuclide transport was studied by means of both steady state and time dependent transport simulations.

- In the steady state simulations, an infinite and non-decaying source of radionuclides in the waste was considered. The source of radionuclides was modelled using a Dirichlet boundary condition. A normalized concentration equal to 1 was imposed at the interface between the waste and the backfill. A normalized concentration equal to 0 was imposed at the outer edges of the DFN (Figure 3-15).
- The transient simulation considered a normalized initial concentration equal to 1 in the waste domain. At the outer boundaries of the DFN (Figure 3-15), the following boundary condition was applied

$$\begin{cases} c\overrightarrow{u_f} \cdot \vec{n} = c_o \overrightarrow{u_f} \cdot \vec{n} \quad \text{for } \overrightarrow{u_f} \cdot \vec{n} < 0 \\ (D_e \overleftrightarrow{I}\, \vec{\nabla} c) \cdot \vec{n} = 0 \quad \text{for } \overrightarrow{u_f} \cdot \vec{n} \geq 0 \end{cases} . \tag{3-24}$$

3.5 Observables

Groundwater flow entering the model domain

The total flow, Q_{domain} (m^3/yr), entering and leaving the domain was calculated by integrating the positive or the negative values of the normal Darcy flow over the edges of the fractures at the model boundaries:

$$\begin{cases} Q_{domain\_out} = \sum \int_{(\vec{q}\cdot\vec{n})>0}^{L} \overrightarrow{u_f} \cdot \vec{n}\, d_f\, dL \\ Q_{domain\_in} = \sum \int_{(\vec{q}\cdot\vec{n})<0}^{L} \overrightarrow{u_f} \cdot \vec{n}\, d_f\, dL \end{cases}, \tag{3-25}$$

where d_f is the fracture aperture (m) and L refers to the length of the edges.

The flow simulations were performed in steady state. Therefore, the computed inflow should be equal to the outflow. So, the mass balance closing error, e can be calculated by comparing the positive values with the negative ones as follows:

$$\varepsilon = \frac{Q_{domain\_out} - Q_{domain\_in}}{Q_{domain\_in}}, \tag{3-26}$$

Mass release leaving the model domain

The mass leaves the modelled domain through the fracture edges formed by the intersection between the fractures and the borders of the domain. The mass flow (mol/s) leaving the domain can be computed as:

$$M_i = \int^L \left[c_i \overrightarrow{u_f} + \left(\overleftrightarrow{D_D} + \overleftrightarrow{I} D_e\right) \cdot \vec{\nabla} c_i\right] \cdot \vec{n}\, d_f\, dL, \tag{3-27}$$

Therefore, the mass flow is computed as the integration over the fracture edges length (L) of the concentration of the dissolved species multiplied by the aperture of the fractures and by the flow normal to the surface.

Groundwater flowing from the fractures to the backfill

Groundwater enters the backfill through the fractures that intersect the vault. The flow entering or leaving the backfill, Q_{tunnel_inflow} (m^3/yr), can be evaluated directly by adding up the flow through the intersections between the fractures and the vault. The flow through a single fracture is calculated by integrating the boundary condition (3-15) that couples the CPM with the fracture domains divided by the fluid density over the length of the intersection, L_{int}:

$$\begin{cases} Q_{tunnel\_inflow} &= \sum \int_{(-\alpha(p_m - p_f))>0}^{L_{int}} -\dfrac{\alpha(p_m - p_f)}{\rho}\, dL_{int} \\ Q_{tunnel\_outflow} &= \sum \int_{(-\alpha(p_m - p_f))<0}^{L_{int}} -\dfrac{\alpha(p_m - p_f)}{\rho}\, dL_{int} \end{cases}, \tag{3-28}$$

Average flow from the fractures to the backfill

The average flow velocity into the backfill (m/s) can be evaluated by dividing the groundwater flow into the backfill (Equation (3-28)) by the integral of the aperture, d_f, over the length of the intersections with inflowing water, L_{int}:

$$\bar{u}_{in} = \frac{Q_{tunnel\_inflow}}{\sum \int_{(-\alpha(p_m - p_f))>0}^{L_{int}} d_f\, dL_{int}}. \tag{3-29}$$

Mass release from the backfill to the fractures

The mass released from the vault to the fractures (mol/s) is computed by integrating the boundary condition (3-18) over the length of the intersection, L_{int}.

$$\begin{cases} M_{tunnel\_inflow} &= \sum \int_{(-\beta(c_m - c_f))>0}^{L_{int}} -\beta(c_m - c_f) dL_{int} \\ M_{tunnel\_outflow} &= \sum \int_{(-\beta(c_m - c_f))<0}^{L_{int}} -\beta(c_m - c_f) dL_{int} \end{cases}, \tag{3-30}$$

Temporal distribution of the mass balance

For the transient simulations, the mass balance is composed of several terms: the mass in the vault (M_v), the mass in fractures (M_f), the accumulated mass lost through the outflow boundaries (M_{outlet}) and the accumulated mass lost by radioactive decay (M_{decay}). The addition of these terms equals the initial mass in the system (M_0):

$$M_o = \iiint^{\psi} c_i \left(\phi + \rho_b K_{d,i}\right) d\psi \qquad at\ t = 0, \tag{3-31}$$

The initial mass (M_0) is calculated as the volume integration of the concentration over the whole porous domain (ψ). The waste is the unique domain with a concentration different than zero at the beginning of the simulation.

The mass balance at a given time t is computed as the sum of the different terms:

$$M_o = M_f + M_v + M_{outlet} - M_{decay}, \quad (3\text{-}32)$$

The mass in the fractures (3-33) is computed as the surface integration of the dissolved mass over the surface of the discrete fractures (S).

$$M_f = \iint_0^S c_i \, \phi_f \, d_f \, dS, \quad (3\text{-}33)$$

The mass in the vault (3-34) is computed by integrating the dissolved and the adsorbed (left and right term in Equation (3-34), respectively) over the vault volume ψ.

$$M_v = \iiint^{\psi} c_i \, \phi \, d\psi \; + \iiint^{\psi} \left(K_{d,i} \, \rho_b\right) c_i \, d\psi, \quad (3\text{-}34)$$

The accumulated mass that has left the system through the outflow model boundaries (3-35) is computed by integrating in time the radionuclide mass flow through the length of the fracture edges (L) defined as outer boundaries. M_v does not account for potential decaying processes that may reduce the mass once it flows outside the model domain.

$$M_{outlet} = \int_0^t \int^L \left[c_i \overrightarrow{u_f} + \left(\overleftrightarrow{D_D} + \overleftrightarrow{I} D_e\right) \cdot \vec{\nabla} c_i\right] \cdot \vec{n} \, d_f \, dL \, dt, \quad (3\text{-}35)$$

The accumulated mass lost by radioactive decay within the modelled domain (3-36) is computed by integrating in time the decay term of the dissolved and the adsorbed mass in the porous and fractured domains.

$$M_{decay} = \int_0^t \iiint^{\psi} \lambda_i \, c_i \left(\phi + \rho_b K_{d,i}\right) d\psi + \int_0^t \iint^S \lambda_i \, c_i \, \phi_f d_f \, dS \, dt. \quad (3\text{-}36)$$

4 Results from the simplified model

This section contains the results of the simulations performed using the simplified model described in Section 3.3.

4.1 Groundwater flow

The model was solved for a set of ten inlet Darcy velocities at the fracture: 1×10^{-13}, 1×10^{-12}, 1×10^{-11}, 1×10^{-10}, 1×10^{-9}, 1×10^{-8}, 1×10^{-7}, 1×10^{-6}, 1×10^{-5} and 1×10^{-4} m/s. Figure 4-1 shows the results of the flow field calculated with an inlet velocity equal to 1×10^{-8} m/s. The results on the left (A) are calculated with a modified version of the model described by Wessely and Shahkarami (2019), which treats the fracture as a 3D porous medium. The results on right were calculated with a combined fracture/CPM model using the flow and transport coupling described in Section 3.2.3.

Both models give the same hydraulic head distribution with high gradients located upstream of the interface between the backfill and the fracture because of the low permeability of the backfill. Most groundwater flow bypasses the backfill, which is less permeable than the fracture.

4.2 Conservative transport

Two types of transport simulations were carried out with the simplified model. The first was a steady state transport simulation of a non-reactive tracer with a prescribed concentration equal to 1 at waste backfill interface. A transport simulation was carried out for each of the flow velocity fields previously calculated and described in the section above. The mass release from the vault to the fractures (mol/s) was computed for each velocity field at the backfill/fracture interface (Equation (3-30). The resulting mass flow will be the same as if computed at the outlet of the domain (Equation (3-27)).

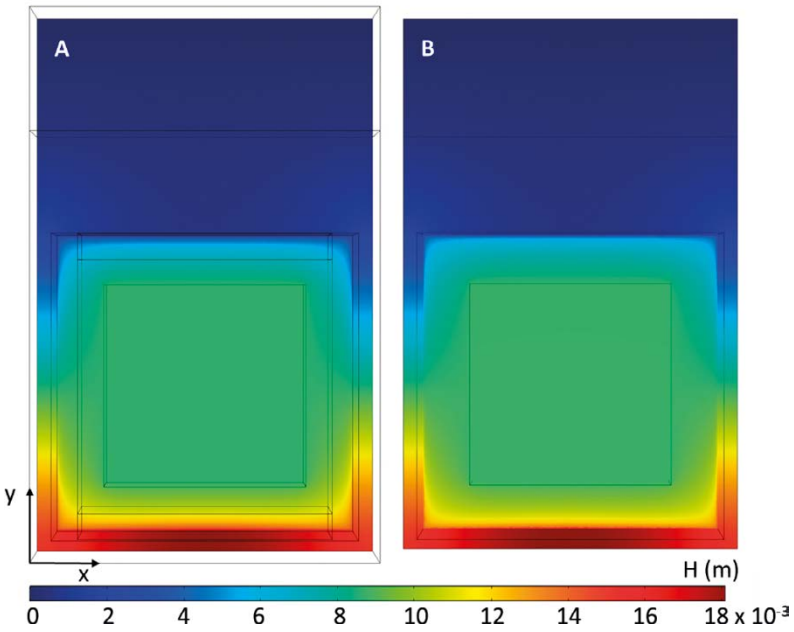

Figure 4-1. *Hydraulic head in a horizontal plane that includes the fracture (blue in Figure 3-4) computed for an inlet velocity equal to 1×10^{-8} m/s. Plot A refers to the model where the fracture is conceptualized as a 3D domain and B to the model with the combined fracture/CPM model using the coupling described in Section 3.2.3.*

Figure 4-2 shows the spatial distribution of the concentration at steady state computed with the fracture conceptualized as a 3D porous medium (A) and the fracture represented as a 2D discrete plane (B). The figure shows the equivalence in terms of spatial distribution for the concentration computed with both models. Note that the concentration is plotted at the centre of the 3D fracture in A. Transport is advection dominated in the fracture, whereas the release of mass through the low permeability backfill is diffusion dominated. Figure 4-3 shows the mass flow computed at the backfill/fracture interface eq. (3-30) for the different inlet Darcy velocities (red dots).

Wessely and Shahkarami (2019) proposed a semi-analytical expression to evaluate the mass flow released from the backfill through the fracture. Although the release of the solute through diffusion does not involve water replacement it can be represented using an effective flow that gives the same solute release. The total effective amount of water released per time unit can be estimated using the expression

$$Q_{tot} = \left(Q_{waste} + \frac{1}{Res + \frac{1}{Qeq}} \right), \tag{4-1}$$

where Q_{waste} (m^3/s) is the flow of water through the waste, Res (s/m^3) is the diffusive transport resistance of the backfill and Q_{eq} (m^3/s) is the capacity of groundwater in the fracture to carry away a solute. The equivalent flow rate Q_{eq} (m^3/s) has been proposed in previous studies (Neretnieks 1980, Neretnieks et al. 1987) as the flow magnitude of water in the rock near a repository vault that becomes contaminated by out-diffusing radionuclides. Originally it was developed under the assumption that the rock can be described as a porous medium. In Joyce et al. (2010), the equations for a DFN model were derived. Using the previous expression (4-1), the release of solute from the repository in steady state, N, is in Wessely and Shahkarami (2019) approximated as

$$N = Q_{tot} \cdot c \approx \left(C \cdot v_{in} + \frac{1}{A + \frac{1}{B \cdot v_{in}^2}} \right) \cdot c, \tag{4-2}$$

where the advective term Q_{waste} is the water inlet velocity in the fracture v_{in} times a fitting parameter C (m^2), the diffusive term Q_{eq} is also a function of the water inlet velocity times a fitting parameter B ($m^2(m/s)^{1/2}$). The diffusive transport resistance of the backfill, Res, is not dependent on the fluid velocity and it is represented by the fitting parameter A (s/m^3).

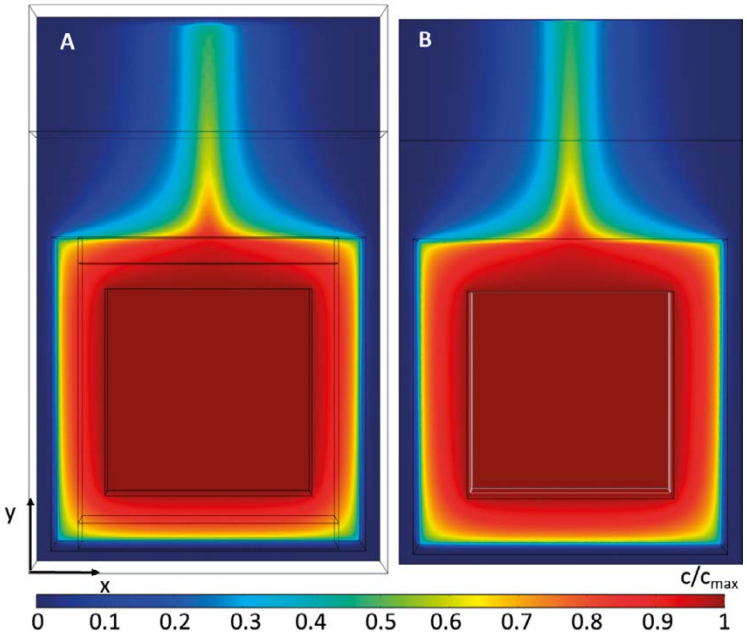

Figure 4-2. *Normalized tracer concentration at steady state for an inlet velocity equal to 1×10^{-8} m/s. A refers to the model where the fracture is conceptualized as a 3D domain and B to the model with the fracture discretised as a 2D discrete fracture.*

Figure 4-3 shows the best fit obtained for the Expression (4-2) with the values of the parameters given in Table 4-1 (green line). The advective term, $C \cdot v_{in}$ (blue dashed-line), the diffusive term, $B \cdot v_{in}^{1/2}$ (grey dashed-line) and the resistance term *(1/A)* are plotted to facilitate the interpretation. Although the expression reproduces the release at high groundwater velocities, the expression by Wessely and Shahkarami (2019) fails to represent the observed behaviour in the case of low groundwater flow velocities.

Table 4-1. Fitted values of the constants in Equation (4-2).

Parameter	Fitted value	Units
A	3.25×10^{8}	s/m^3
B	5.00×10^{-5}	$m^2(m/s)^{1/2}$
C	9.08×10^{-4}	m^2

We propose a modification of the expression proposed by Wessely and Shahkarami (2019) to fit the model result over a wider range of groundwater velocity cases. The proposed expression is

$$N = Q_{tot} \cdot c \approx \left(C \cdot v_{in} + \frac{1}{A + \left(\frac{1}{D \cdot v_{in}} \right)} \right) \cdot c + E \cdot c, \qquad (4\text{-}3)$$

Note that this expression differs in the term that originally depended on Q_{eq}, which, in the modified expression, appears as a term dependent on Q_{eq}^2. In addition, a base diffusion flux $E \cdot c$ is added to account for the diffusive flux between the source and the outlet boundary in the absence of flow

Figure 4-4 shows the resulting mass fluxes (green line) calculated using Equation (4-3) and the fitting parameters given in Table 4-2. The advective term, $C \cdot v_{in}$ (blue dashed-line), the diffusive term, $D \cdot v_{in}$ (grey dashed-line), the resistance term *1/A* (orange dashed-line), and the base diffusive flux *E* (purple dashed-line) are plotted to facilitate the interpretation.

Four regions can be differentiated according to the water inlet velocity. The values of the fluid velocities that define the four regions can be estimated theoretically based on the fitting parameters in Table 4-2

$$v_{in_1} = \frac{E}{D}; \qquad v_{in_2} = \frac{1}{AD}; \qquad v_{in_3} = \frac{1}{AC}. \qquad (4\text{-}4)$$

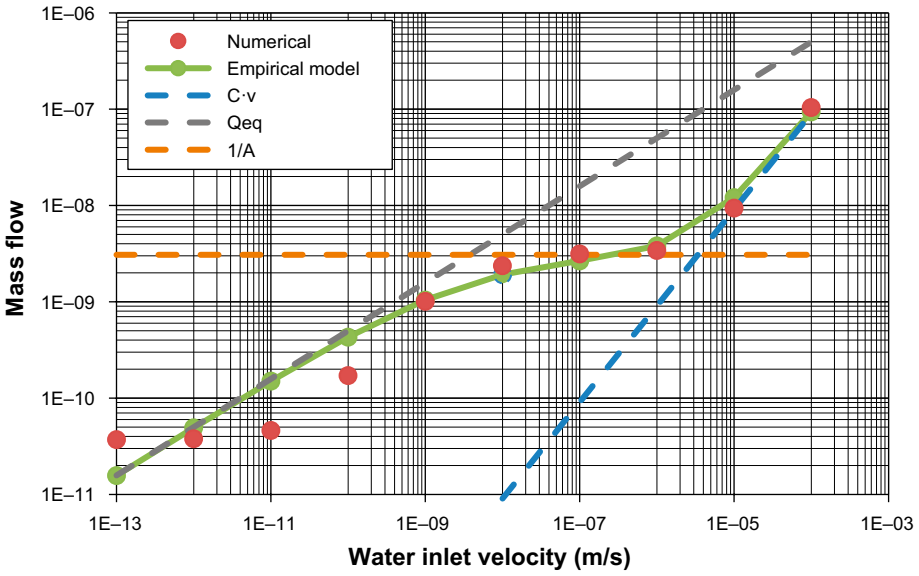

Figure 4-3. *Mass flux computed (red dots) for different water inlet velocities. The green line shows the mass fluxes calculated using Equation (4-2) and the dashed lines illustrate the different terms of the expression.*

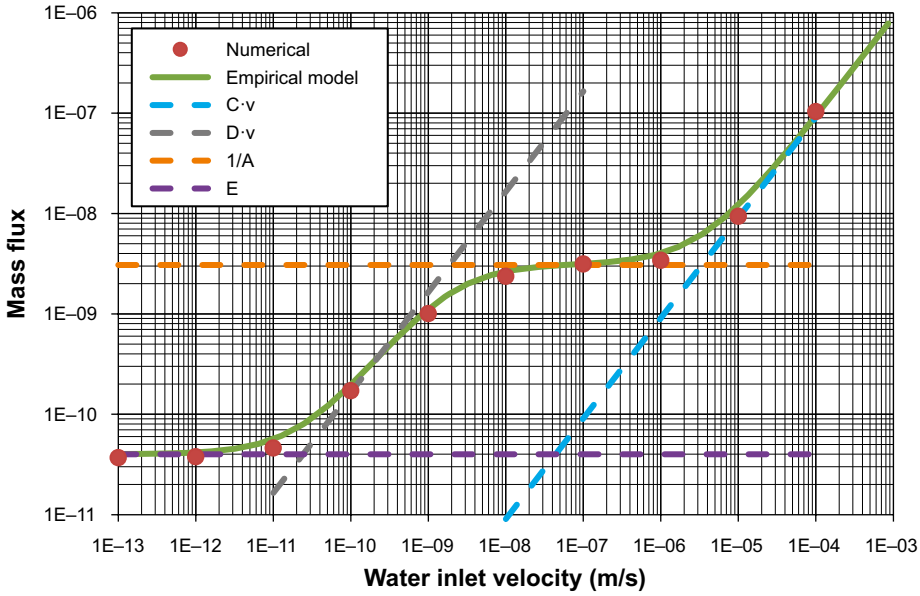

Figure 4-4. *Mass flow computed (red dots) for different water inlet velocities. The green line shows the mass flows calculated using Equation (4-3) and the dashed-lines illustrate the different terms of the expression Table 4-2.*

Table 4-2. Fitted values of the constants in Equation (4-3).

Parameter	Fitted value	Units
A	3.25×10^{8}	s/m^3
C	9.08×10^{-4}	m^2
D	1.65	m^2
E	4×10^{-11}	m^3/s

For fluid velocities lower than 2.4×10^{-11} m/s the resulting mass flux corresponds to a velocity independent diffusive flux between the source and the boundary. If the distance between the source and the boundary tends to infinity, this flux would approach zero. However, for the application presented here, the distance is of the order of meters, therefore, there is a diffusive flow forced by the model boundary conditions. The fitted parameter, *E* corresponds to the diffusive mass flux from the waste to the closest boundary, i.e., the inlet boundary, through the 0.1 m wide fracture, given that the waste has unit concentration.

The second region corresponds to the range of water velocities between 12.4×10^{-11} and 2×10^{-9} m/s. In this region the mass flow increases linearly with the water velocity. The conceptual model for this velocity range corresponds to the concept of Q_{eq} as defined in previous studies (Neretnieks 1980, Neretnieks et al. 1987) . The Q_{eq} is given by the magnitude of the water flow in the fracture around the backfill that advectively transports radionuclides diffusing into the fracture. However, the concept of Q_{eq} has previously been defined for infinitely large fractures, which is not the case of the model presented here. For small fractures with low water flow velocity the Q_{eq} is to a good approximation given by the flow of water through the fracture. For this simplified model where the water flow through the inlet is the same as the flow that bypasses the buffer, the value of the fitted parameter *D* corresponds to the cross-sectional area of the fracture at the inlet.

The third region corresponds to the range of water velocity between 2×10^{-9} and 3.4×10^{-6} m/s. In this region, the transport is limited by the diffusion through the backfill, and therefore, the mass flux is almost independent of the water flow velocity. The fitted parameter, *A* corresponds to the transport resistance of the backfill (*Res*).

For fluid velocities higher than 3.4×10^{-6} m/s, the mass flux is driven by the water flow through the waste. The fitted parameter *C* corresponds to the flow of water through the waste divided by the inlet flow velocity.

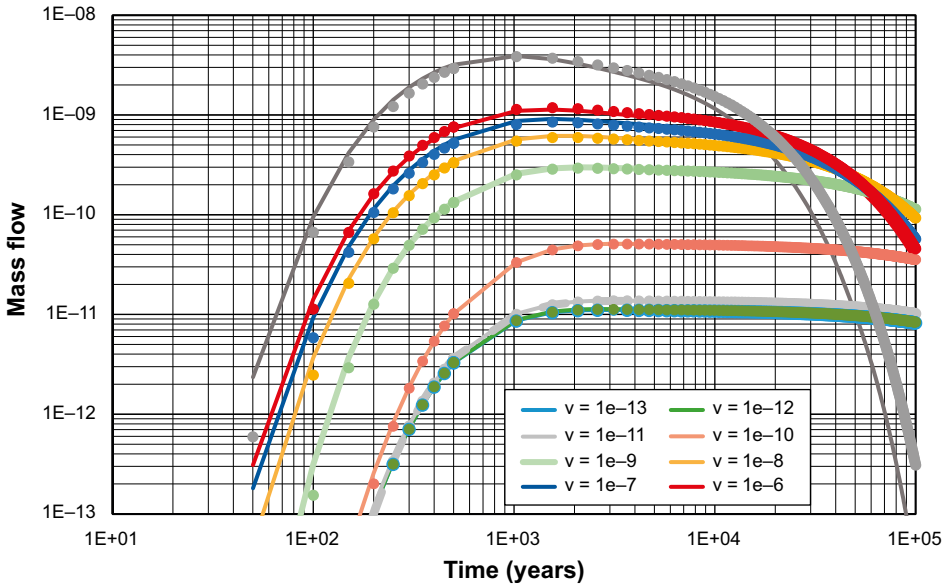

Figure 4-5. *Breakthrough curves evaluated at the backfill/fracture interface for different inlet velocities. Lines show the results from the simplified model where the fracture is represented as a 3D porous medium whereas the dots show the results for the fracture represented as a 2D object.*

In addition to the analysis of the tracer release at steady state, a set of transient simulations were carried out both with the fracture conceptualized as a 3D porous medium and the fracture represented as a 2D discrete plane. The breakthrough curves are the releases from the repository evaluated at the backfill/fracture interface for the different inlet velocities (Figure 4-5).

4.3 Radioactive decay

The simplified model has been used to test the implementation of first-order decay in the case of the fracture represented as a 2D discrete plane. For verification, the simulations were performed using both the model that represents the fracture as a 2D surface and the model that represents the fracture as a 3D domain. The simulation considers two radionuclides (^{36}Cl and ^{93}Mo) and a non-decaying tracer. The transport simulations were performed using the flow field obtained with an inlet velocity equal to 1×10^{-6} m/s. Figure 4-6 shows the evolution of the radionuclide mass within the vault computed as defined in Equation (3-34). Note that in this case there is no adsorption and thus the right term is zero. As expected, the total mass decreases with time not only due to advection and diffusion but also due to radioactive decay. The differences in the temporal evolution of the mass between the tracer and the two radionuclides are caused by the different half-lives of the radionuclides. As expected, the mass of ^{93}Mo decreases faster than that of ^{36}Cl due its shorter half-life. The effect of the decay can be hardly observed in the simulation due to the ^{36}Cl long half-life. Figure 4-6 also compares these results with those obtained from the model where the fracture is conceptualized as a 3D porous medium. For ^{93}Mo both cases give the same results, confirming that the implementation of first-order decay in the model where the fracture is represented as a 2D discrete plane is consistent with that of a 3D porous medium.

The effect of the decay can also be observed in the breakthrough curves evaluated at the backfill/fracture interface, see Figure 4-7. In Figure 4-7 the breakthrough curves obtained from both the 2D and the 3D models are shown and the results are in good agreement wuth each other. The curves show that the decay of the radionuclides within the repository reduces the release especially for ^{93}Mo due to its short half-life. The breakthrough curve of ^{36}Cl and the tracer practically overlap each other but start to differ at large times due to the decay of the long lived ^{36}Cl[6] (half-life 301 000 years).

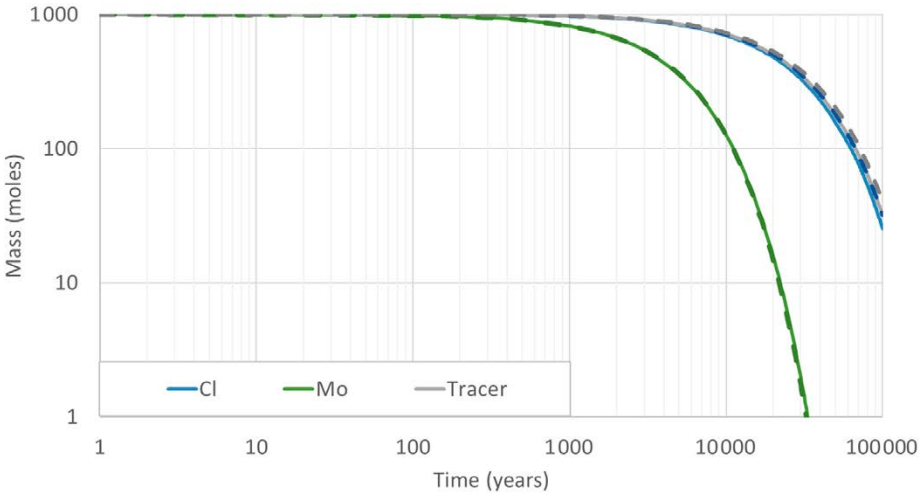

Figure 4-6. *Temporal evolution of the mass of ^{36}Cl, ^{93}Mo and the non-reactive tracer in the vault and comparison between the porous medium approach model, where the fracture is conceptualized as a 3D porous medium (solid lines), and the discrete fracture approach (dashed lines).*

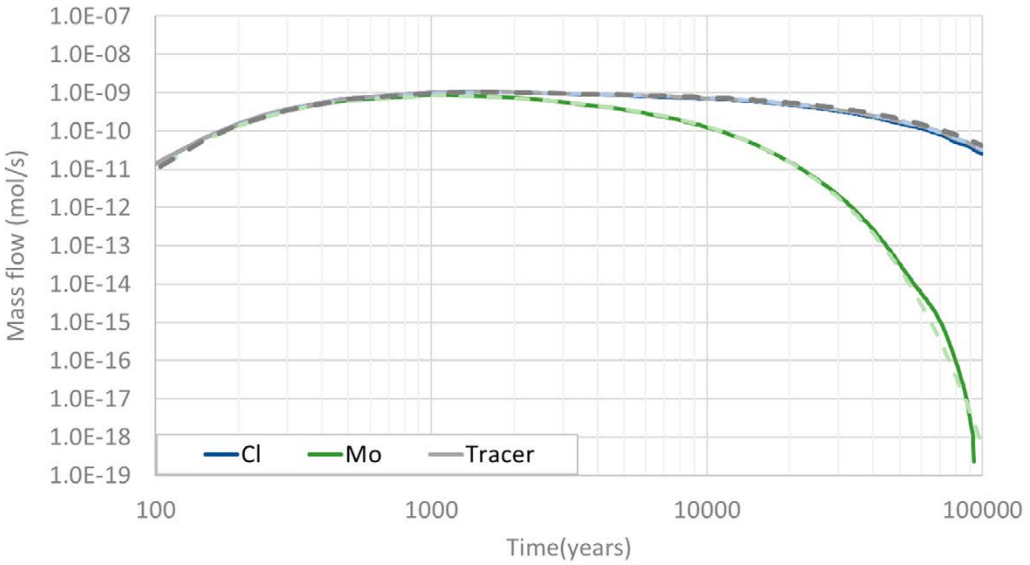

Figure 4-7. *Breakthrough curves calculated at the backfill/fracture interface for a conservative tracer, ^{36}Cl and ^{93}Mo obtained using the 3D (solid lines) and the 2D (dashed lines) representations of the fracture.*

5 Results from the BHA model with generic boundary conditions

This section contains the results of the simulation performed using the BHA model described in Section 3.4 applying generic boundary conditions.

5.1 Groundwater flow

In the groundwater flow simulations, the hydraulic gradient is horizontal. The horizontal gradient is defined by applying a fixed pressure difference between the west and east boundaries (Figure 5-1, left) in one set of simulations and between the north and south boundaries (Figure 5-1, right) for another set. The remaining edges are no flow boundaries. The case with the W-E gradient simulates a regional groundwater flow transverse to the BHA vault. The case with the N-S gradient results in a regional groundwater flow parallel to the BHA. The heterogeneity of the fractures can locally modify the direction of the flow.

Simulations were performed with a wide range of pressure gradients to cover a wide range of flow magnitudes. In these simulations, the pressure difference between the two boundaries ranged between 3 Pa and 3.0×10^{9} Pa, which correspond to average hydraulic head gradients of 7.6×10^{-7} and 764 m/m over the model domain, respectively. The extreme values may seem unrealistic in natural conditions. However, they are needed to later simulate the radionuclide release in cases with almost no flow (low values) and in cases with extremely high flow in which water is forced through the low permeability bentonite backfill.

The case with a pressure difference of 30 000 Pa between the boundaries, which corresponds to an average hydraulic head gradient of 0.0076 m/m over the domain, is selected to describe the flow results. This case corresponds to reasonable natural conditions.

The W-E gradient results in a total groundwater flow of 69.7 m^3/y crossing the model domain. The N-S gradient results in a flow of 537 m^3/y, which is almost 8 times higher than with the W-E gradient. In this DFN realization, the large difference in total flow is caused by a high density of fractures with high transmissivity and connectivity in the N-S direction.

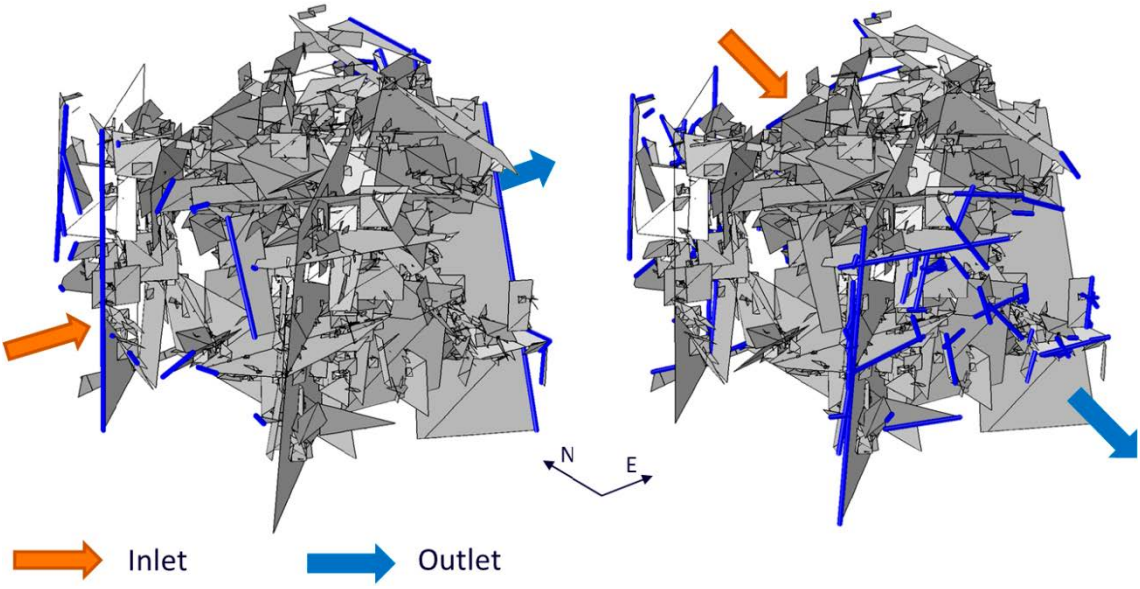

Figure 5-1. *Model domain indicating the position of the boundary conditions (blue edges) for the case where groundwater flows from west to east (left) and from north to south (right).*

The W-E gradient yields a flow of 0.091 m^3/y through the BHA vault, whereas the N-S gradient gives a total flow through the vault of 0.14 m^3/y. Although the water flowing through the domain is almost 8 times higher, the resulting flow entering the vault is only 1.5 times larger for the N-S gradient (parallel to the vault) than for the W-E gradient (perpendicular to the vault).

Figure 5-2 shows the fluid pressure distribution in the steady state case for the W-E gradient (left) and the N-S gradient (right). The fluid pressure at the rock/BHA interface is illustrated in Figure 5-3. The pressure field shows an inversion of the flow direction through the vault depending on the gradient direction. In the W-E gradient case (Figure 5-3, left), the main inflow occurs through the fractures intersecting the southern part of the vault and the outflow through fractures in the northern part. Even though the regional groundwater flow has a west-east direction, the groundwater flows from south to north in the BHA subject to the connectivity of the fractures that intersect the vault. The fractures intersecting north part of the vault are well connected to the fractures that reach the east boundary and the fractures intersecting the southern part are well connected with the west boundary. In the N-S gradient case, groundwater flows through the vault from north to south according to the imposed regional groundwater flow. Note that some fractures that intersect the vault are not connected to the boundary of the model and have no influence over the water flow field. The inflow occurs in a cross-sectional area of 0.68 m^2 and 0.55 m^2 for the W-E and N-S gradient cases, respectively.

Figure 5-4 shows the magnitude of the Darcy velocity (on a logarithmic scale) for the W-E gradient (left) and the N-S gradient (right). The lowest values of the Darcy velocities, lower than 1×10^{-18} m/s, are observed in the fractures that are not connected to the fracture network. In the W-E gradient case, the highest velocities occur in the fractures near the top of the model with NNE and NSE direction whereas in the N-S gradient case, the highest velocities are in the fractures with a north and NNW direction.

The magnitude of the Darcy velocity at the rock/vault interface is illustrated in Figure 5-5. The high flow velocities are located at the same edges independently of the direction of the gradient. The edges with lower Darcy velocities are intersections with dead end fractures. The density of isolated fractures is higher in the centre than at the northern and southern ends of the vault.

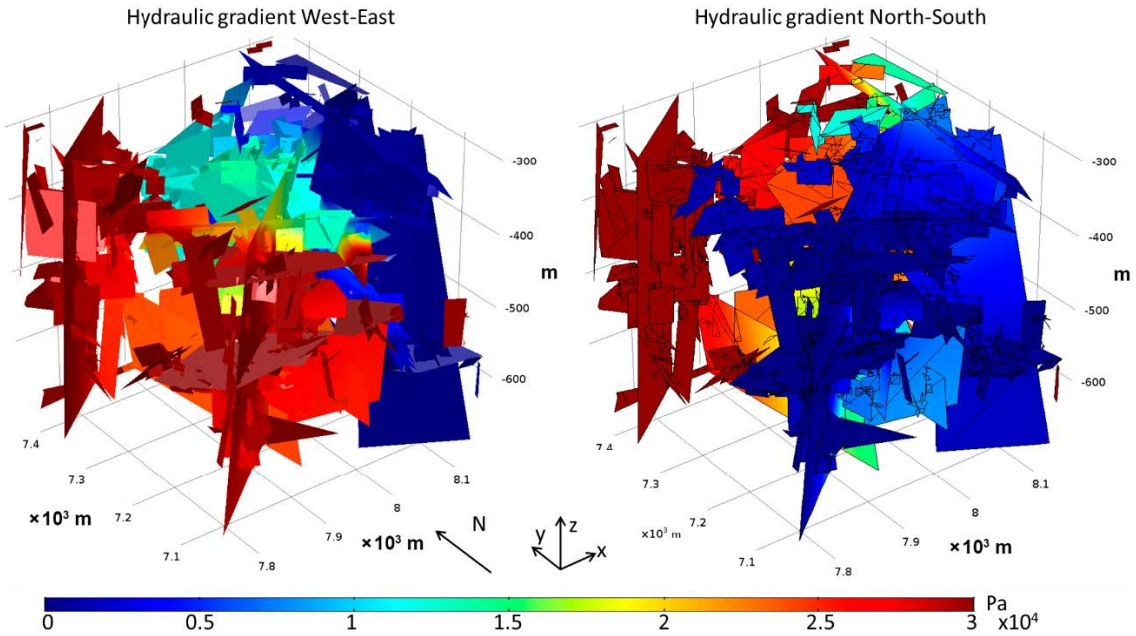

Figure 5-2. *Computed pressure distribution in the fractures for a steady state simulation with a pressure difference of 30 000 Pa between the west and east boundaries (left) and between the north and south boundaries (right).*

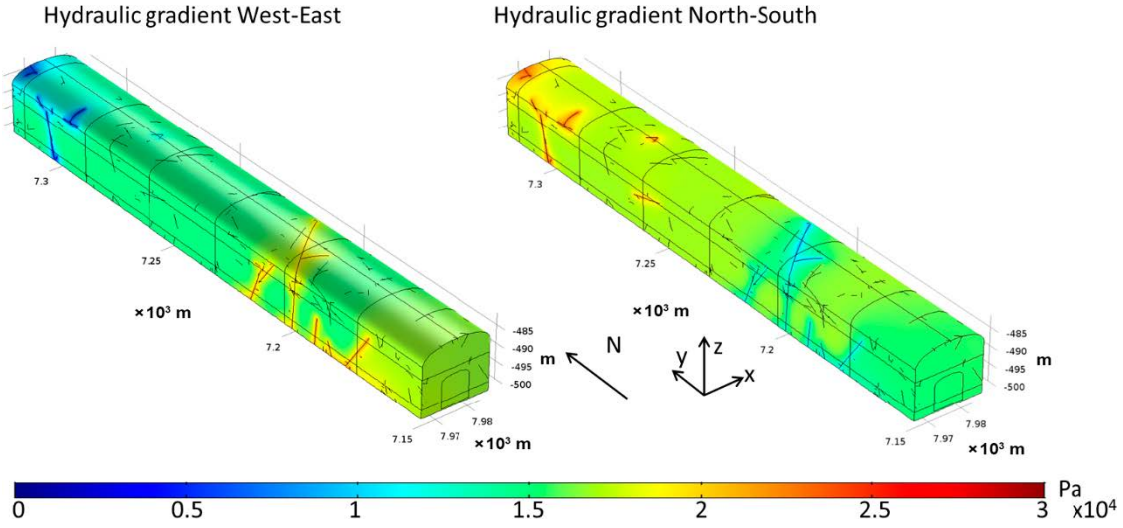

Figure 5-3. *Computed pressure distribution in the vault for a steady state simulation with a pressure difference of 30 000 Pa between boundaries from west to east (left) and from north to south (right).*

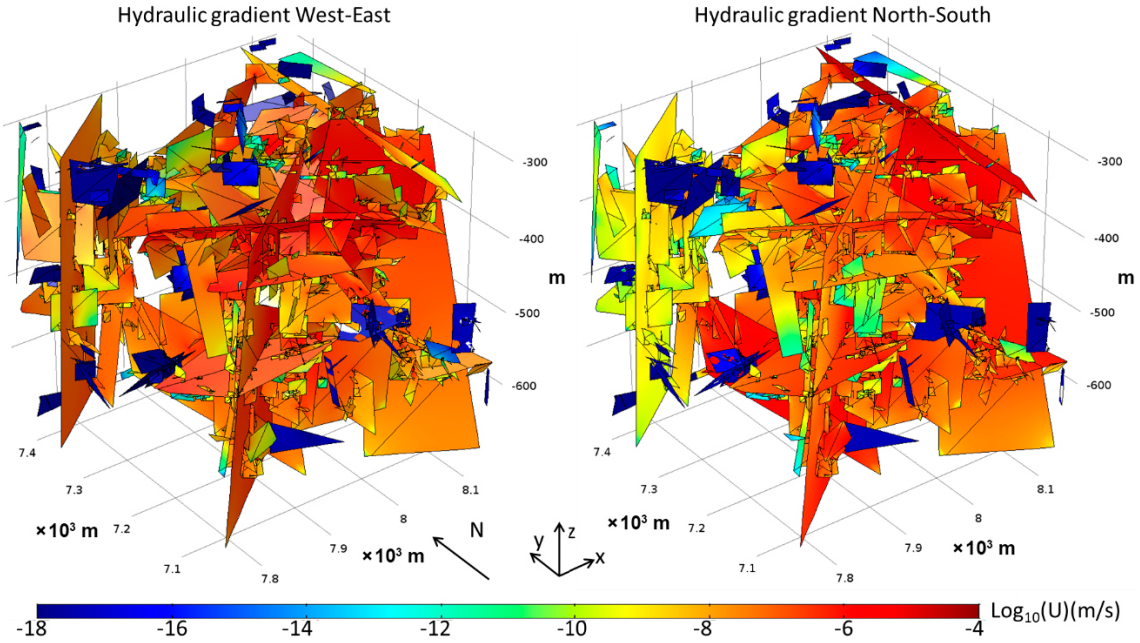

Figure 5-4. *Distribution of the magnitude of the Darcy velocity in the fractures for a steady state simulation with a pressure difference of 30 000 Pa between the west and east boundaries (left) and between the north and south boundaries (right).*

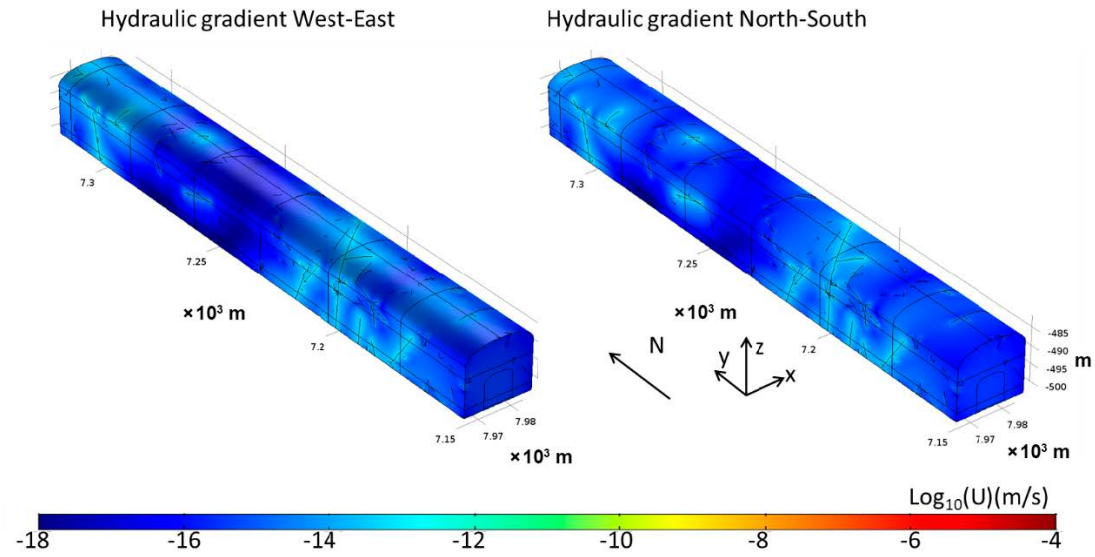

Figure 5-5. *Distribution of the magnitude of the Darcy velocity at the rock/BHA interface for a steady state simulation with a pressure difference of 30 000 Pa between the west and east boundaries (left) and between the north and south boundaries (right).*

The calculated groundwater flow entering the BHA vault obtained using Equation (3-28) in Section 3.4.4 for the different pressure boundary conditions are summarized in Table 5-1. The inflow to the BHA varies linearly with the pressure gradient. The groundwater flow through the BHA vault is 1.56 times higher in the N-S gradient case, when the vault is parallel to the regional gradient.

Table 5-1. Computed flow entering the BHA vault.

Pressure difference between boundaries	Flow m^3/y case W-E	Flow m^3/y case N-S
3.0×10^{9}	9.11×10^{3}	1.42×10^{4}
3.0×10^{8}	9.11×10^{2}	1.42×10^{3}
3.0×10^{7}	9.11×10^{1}	1.42×10^{2}
3.0×10^{6}	9.11	1.42×10^{1}
3.0×10^{5}	9.11×10^{-1}	1.42
3.0×10^{4}	9.11×10^{-2}	1.42×10^{-1}
3.0×10^{3}	9.11×10^{-3}	1.42×10^{-2}
3.0×10^{2}	9.11×10^{-4}	1.42×10^{-3}
1.5×10^{2}	1.82×10^{-4}	2.84×10^{-4}
3.0×10^{1}	9.11×10^{-5}	1.42×10^{-4}
1.5×10^{1}	1.82×10^{-5}	2.84×10^{-5}
3.0	9.11×10^{-6}	1.42×10^{-5}

This work employs a discrete representation of the fractured rock. However, Appendix A presents an exercise of comparison of groundwater flow simulations using this DFN model and an ECPM model obtained through upscaling using DarcyTools (Svensson and Ferry 2010) over different resolution grids. Flow simulations with the ECPM are performed with DarcyTools. When analysing the flow results through the BHA vault, a slight flow reduction is observed with increasing mesh resolution in the DFN model. However, the ECPM model shows an unexpected behaviour. Flow through the BHA decreases when reducing the element size from 25 to 3.125 m. With a grid size of 3.125 m, there is a good agreement with the DFN's results (Figure A-7). However, the water inflow increases in the ECPM model as the element size decreases from 3.125 m. A set of changes in the DarcyTools model configurations were carried out to analyse whether these results were a consequence of a numerical artefact (see Appendix A for details), but all simulations resulted in similar vault inflow values.

So, no clear explanation has been found for this unexpected increase of water inflow with a very high-resolution upscaling. It may relate to a change in connectivity along a fracture due to upscaling when the element size is too small. As a result, the cells representing the fracture may become hydraulically disconnected.

5.2 Conservative transport

Steady state transport simulations were carried out under the set of flow fields presented in the section above. The objective was to find a relation between the radionuclide release from the vault and the groundwater flow under steady-state conditions. In these simulations the radionuclide concentration at the waste-backfill interface was prescribed as 1 (see Section 3.4.3 for details). Depending on the fluid velocity, the solute transport in groundwater will be dominated by diffusion or advection. The wide range of pressure differences used (Section 5.1) was selected to cover the whole range of diffusion and advection-controlled transport.

Figure 5-6 shows the computed steady state distribution of conservative, non-decaying tracer for the lowest groundwater flow velocities (case A), one with the highest velocities (case C) and an intermediate case (case B). Case A is characterized by small groundwater flow velocities and hence the transport is governed by diffusion. The tracer has diffused through most of the DFN. Even fractures located upstream of the vault show high values of concentration, evidencing that diffusion has a larger effect than the dilution by the inflowing water. Case C shows the opposite, high flow velocities generate a dilution effect that reduces the concentration in the fractures. The exception is dead-end fractures, which are fractures connected to the vault but separated from the main fracture network. These fractures reach a concentration equal to 1 due to diffusion. These isolated fractures do not affect the groundwater flow, but they can have an important retardation effect on solute transport due to their storage capacity. Diffusion in the intergranular pore space is not accounted for here and it can have an effect as well. In the intermediate case B (Figure 5-6) both diffusion and advection play a role and the contaminant is distributed in the downstream part of the DFN. The dilution effect caused by mixing with the incoming water is evident in the upstream fractures. Regarding the concentration within the vault, simulations A and B show that almost all the bentonite backfill has unit tracer concentration suggesting that diffusion is the governing transport process inside the repository. Cases B show some dilution near the inflow areas and for case C the tracer concentration near the inflow areas is reduced by more than an order of magnitude, indicating that advection gives a significant contribution to tracer transport inside the repository. Thus, for case B, the transport through the DFN depends on the regional groundwater flow, whereas the transport inside the vault is governed by diffusion due to the low permeability of the bentonite backfill. The resulting system with a low permeability porous medium intersected by fractures follows the conceptual model described for the simplified model (Chapter 4), which in summary consists of a low permeability porous domain in contact with a high permeability fracture.

The analysis of the mass flows (Equation (3-30)) evaluated at the backfill/fracture interface for the wide range of groundwater flow velocities (Figure 5-7) shows a behaviour consistent with the observations from the simplified model. The average groundwater flow velocity is calculated using to Equation (3-29). The curve is similar for both regional groundwater flow orientations (W-E and N-S).

The equivalent flow rate Q_{eq} (m^3s^{-1}) has been proposed in previous studies (Neretnieks 1980, Neretnieks et al. 1987) as the flow magnitude of water in the rock near a repository vault that becomes contaminated by out-diffusing radionuclides. The mass flow results presented in Figure 5-7 are computed with a normalized concentration at the waste backfill interface and its magnitude should in some sense be similar to the concept of Q_{eq} .Wessely and Shahkarami (2019) proposed a semi-analytical expression to evaluate the mass flow released from the backfill through a single fracture (see Chapter 4) by introducing an effective flow that gives the same solute release. The total effective amount of water released per time unit can be estimated using Equation (4-1). Using this expression, the release of solute from the repository in steady state is in Wessely and Shahkarami (2019) approximated as Equation (4-2).

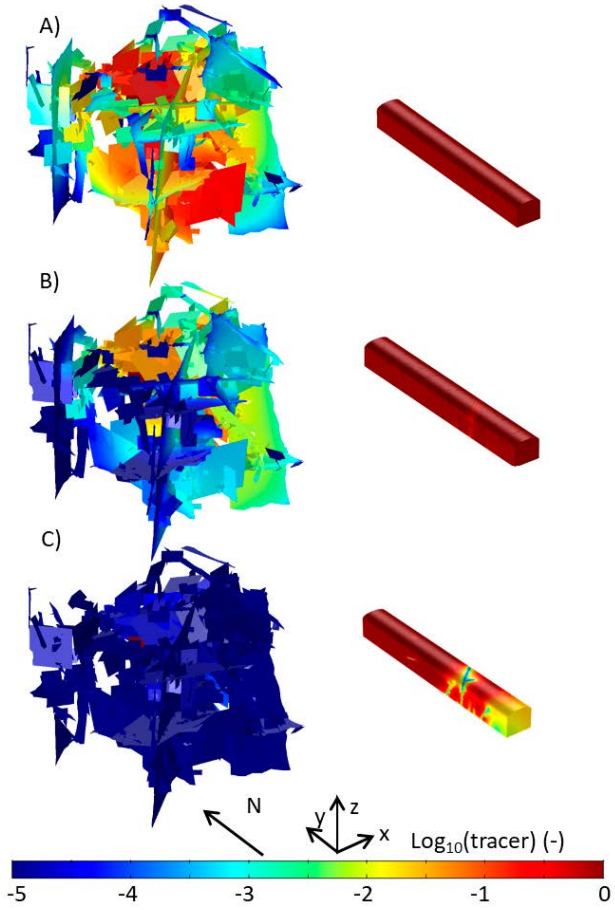

Figure 5-6. *Tracer distribution (in log scale) in the DFN (left) and in the BHA (right) for three groundwater flow fields: A) case with 3 Pa pressure difference between boundaries, B) case with 30 000 Pa pressure difference between boundaries and C) case with 3.0×10^8 Pa pressure difference. The pressure gradient is from west to east in the three cases.*

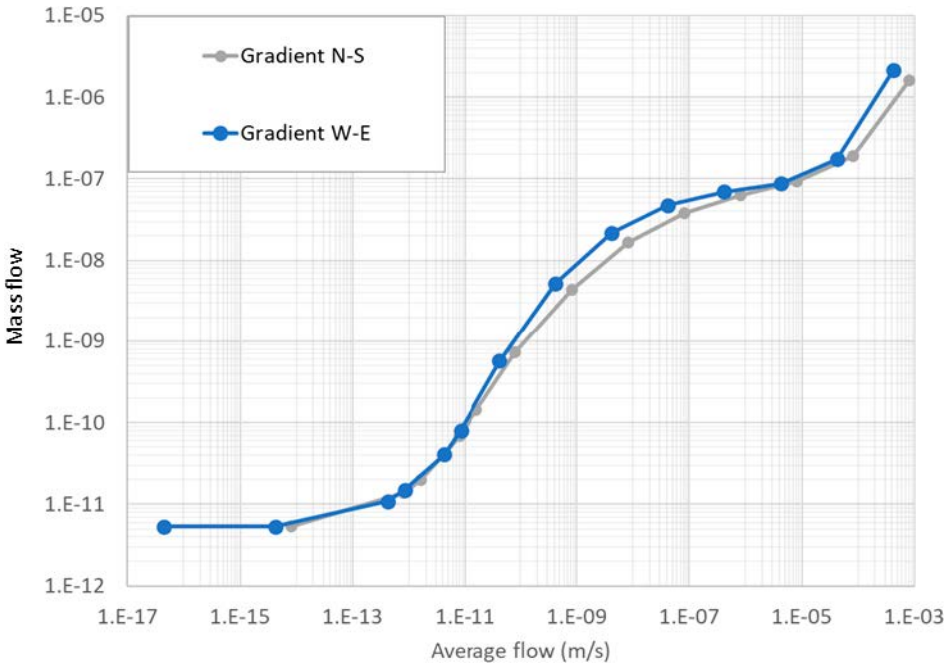

Figure 5-7. *Mass flow evaluated at the backfill/fracture interface versus the average water inflow for the cases of W-E gradient (blue) and the N-S gradient (grey).*

The best fit for the expression (4-2) is obtained for the values of the parameters A, B and C in Table 5-2. The resulting expression is plotted against the model results in Figure 5-8 (green line). The advective term, $C \cdot v_{in}$ (blue dashed-line), the diffusive term, $B \cdot v_{in}^{1/2}$ (grey dashed-line) and the resistance term $1/A$ are plotted to facilitate the interpretation. The expression reproduces well the release at high groundwater velocities. However, the empirical expression fails to represent the observed behaviour in the case of low groundwater flow velocities.

The reason of this divergence is in the assumptions of the empirical solution. It assumes that mass flow is governed by the Q_{eq} for low velocities. The concept of Q_{eq} assumes that the fractures connected to the vault have sufficient capacity to carry all the solute that leaves the repository to ensure a very small concentration of solute in the fractures not directly connected to the vault. This assumption is valid when the fractures have a sufficient flow of water to dilute the solute concentration diffusing from the backfill. However, in the BHA model the fractures intersecting the vault do not have an infinite extent and the water volume flowing through them is limited. In this case, the dilution is not as efficient as assumed by the Q_{eq} term. Therefore, the concentration gradient within the fractures connected to the vault is smaller than that estimated using the Q_{eq} concept and the resulting mass release is reduced. This effect explains the steeper slope of the numerical results compared with the fitted expression in Figure 5-8.

Table 5-2. Fitted values for the constants in Equation (4-2) for the BHA model.

Parameter	Fitted value	Units
A	1.35×10^{7}	s/m^3
B	6×10^{-4}	$m^2(m/s)^{1/2}$
C	4.75×10^{-3}	m^2

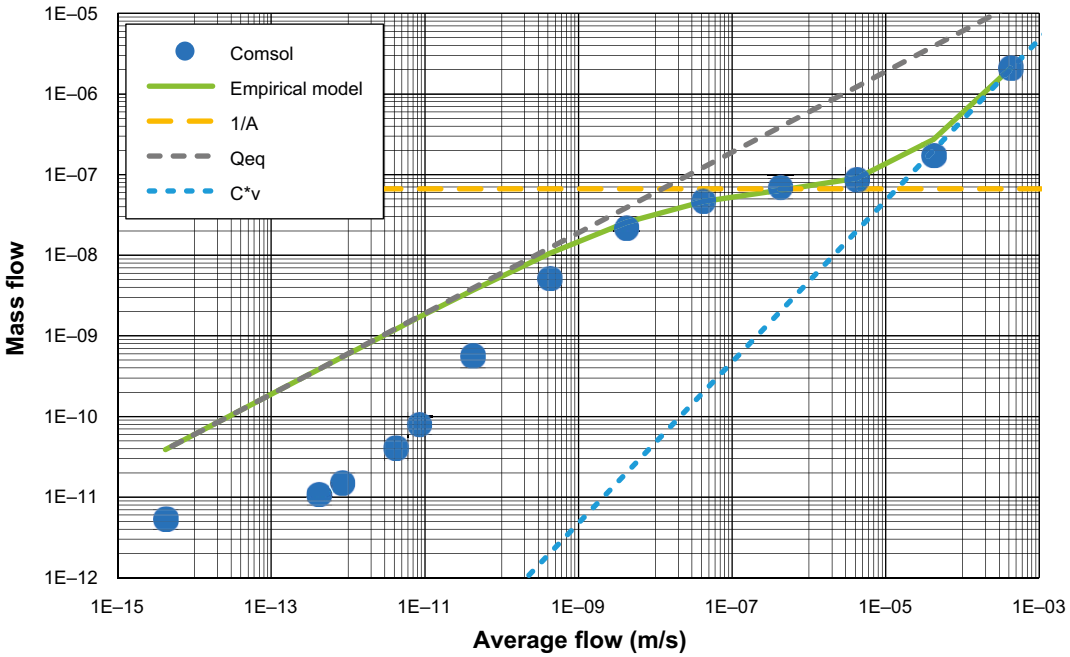

Figure 5-8. *Comparison between the computed mass flow (blue dots) and the empirical expression (4-2) (green line). The values of the parameters that best fit the results are reported in Table 5-2.*

Equation 4-3 fits the model results over a wider range of groundwater velocity cases when using the values of the four fitting parameters, *A, C, D* and *E* in Table 5-3. This expression differs in the term that depends on Q_{eq}, which in the modified expression appears as a linear dependence on the average velocity. In addition, a base diffusive flux, $E \cdot c$, is added to account for the diffusion flux between the source and the outlet boundary in the absence of flow (see also the results for the simplified model in Chapter 4).

In Figure 5-9 the resulting mass flows from the empirical model (green line) are plotted against the model results. The advective term, $C \cdot v_{in}$ (blue dashed-line), the diffusive term, $D \cdot v_{in}$ (grey dashed-line), the resistance term *1/A* (orange dashed-line) and the base diffusive flux E (purple dashed-line) are plotted to facilitate the interpretation.

Table 5-3. Fitted values of the constants in Equation (4-3).

Parameter	Fitted value	Units
A	1.5×10^{7}	s/m^3
C	4.75×10^{-3}	m^2
D	12	m^2
E	6×10^{-12}	m^3/s

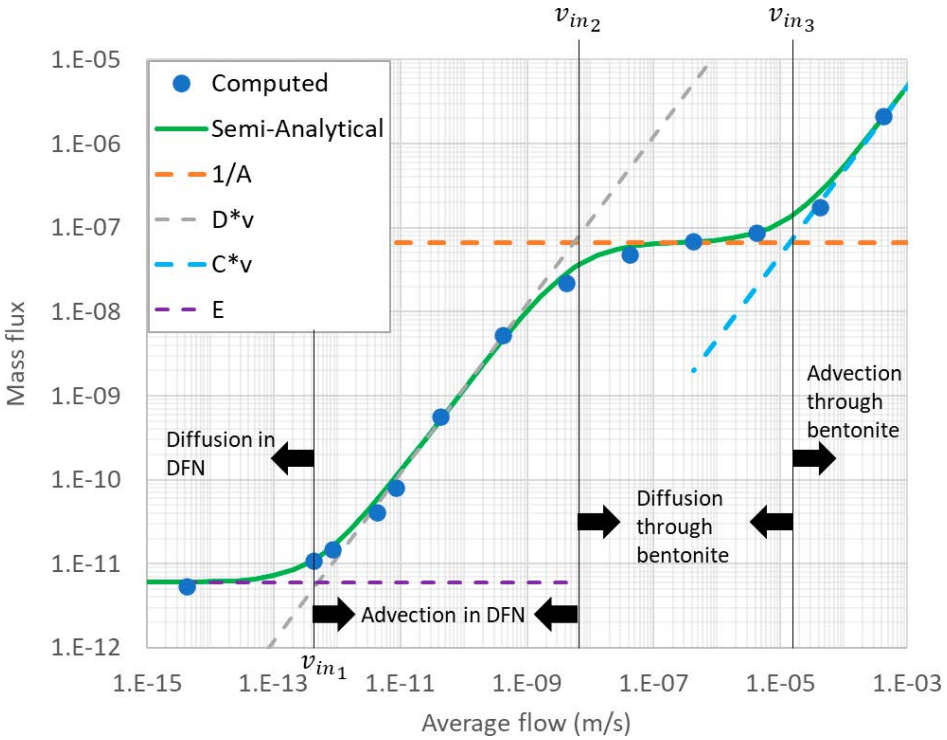

Figure 5-9. *Comparison between the computed mass flow (blue dots) and the empirical expression (4-3) (green line). The values of the parameters used to calculate the empirical expression are reported in Table 5-3. Four regions are defined according to the inflexion points of the curve.*

The empirical expression fits the numerical results over the whole range of flow values. From the lowest flow velocity to the highest, the following regions are defined:

- Diffusion in the DFN. When the water flow through the fractures is slow the water is almost stagnant, and then the transport is dominated by diffusion through the host rock. For fluid velocities lower than 5×10^{-13} m/s the resulting mass flow corresponds to a constant purely diffusive flow forced by the model boundary conditions. If the distance between the source and the boundary tends to infinity, this flow would approach zero.
- Advection in the DFN. This region corresponds to flow velocities between 5×10^{-13} m/s and 5.5×10^{-9} m/s. In this region, the empirical expression is dominated by the Q_{eq} term, and the mass flow increases linearly with the water velocity. The Q_{eq} is given by the magnitude of the water flow in the fracture around the backfill that advectively transports radionuclides diffusing into the fracture. However, the concept of Q_{eq} has previously been defined for infinitely large fractures, which is not the case for the model presented here. For small factures, the Q_{eq} is limited by the flow of water through the fractures connected to the vault and the linear relationship between the mass flow and the groundwater velocity, suggests that the critical factor in this velocity range is advective transport through the fracture network.
- Diffusion through the bentonite. This region corresponds to flow velocities between 5.5×10^{-9} m/s and 1.4×10^{-5} m/s. The release in this region is almost independent of the groundwater velocity evidencing that diffusion through the bentonite backfill is the key controlling factor. Transport is governed by the transport resistance of the backfill (*Res*).
- Advection through the bentonite. This region corresponds to flow velocities higher than 1.4×10^{-5} m/s. Here, the radionuclide release is characterized by the advective flow that is forced through the bentonite backfill at these high flow velocities. The release is driven by the water that enters the vault, flowing through the backfill and the waste as is illustrated in Figure 5-6c.

6 Results from the BHA model with boundary conditions from the regional model

This section contains the results from the model of the BHA and its surrounding DFN using boundary conditions coming from the regional model (see Section 3.4.3). With those boundary conditions, a single simulation was carried out to obtain a realistic flow field around the BHA. First, the results from the flow simulation are described. Second, the results of a steady state conservative transport simulation are analysed and compared with the results obtained from the BHA model with generic boundary conditions. Last, the results of transient transport simulations are presented. These simulations describe the release of ^{36}Cl, ^{93}Mo and ^{135}Cs from the BHA waste and include linear sorption in the bentonite backfill and first-order decay.

6.1 Groundwater flow

The input data for the BHA model were obtained from the regional hydrogeological simulations performed by Joyce et al. (2019) using the software Connectflow (Hartley and Holton 2004). The pressure field from the regional model was imported into Comsol and imposed as initial and boundary conditions in the BHA model (see Section 3.4.3 for details). The groundwater flow was solved in steady state.

The computed residual pressure in the discrete fracture network around the BHA (Figure 6-1) shows the main inflow and outflow areas. The inflow is concentrated along the southwest border, with a maximum at the top and bottom of the model domain. The main outflow areas are located at the northeast boundaries. The computed flow through the BHA is 0.073 m^3/y, which is 3.4 times larger than the one reported in Abarca et al. (2019) (0.0218 m^3/y). The differences between these flows are caused by the different representation of the host rock (it was treated as an ECPM in Abarca et al. (2019)), differences in the geometry of the repository (here, we only consider the BHA vault) and the different model dimensions. Among them, the main expected contributor to the flow reduction is the absence of the BHK vault. In the model of the whole repository, the BHK, backfilled with concrete, is 50 m away and parallel to the BHA. In that case, the BHK captures 1.1 m^3/y of the flow from the surrounding rock. This flow is two orders of magnitude higher than the flow through the BHA (Abarca et al. 2019). Therefore, it is not unreasonable that, a small part of that flow is forced from the fractures into the BHA in the absence of the other, more permeable, vault. The representation of the host rock has an effect, as illustrated by the comparison between the representation of the host rock as a DFN or as an ECPM in Appendix A. In that comparison the flow through the vault decreases with a DFN representation of the rock. Therefore, the different host representation cannot explain the decrease in flow through the BHA with respect to one reported in Abarca et al. (2019). The model dimensions are expected to have a negligible effect compared to the other two factors.

The magnitude of the Darcy velocity in the fractures is shown in Figure 6-2. The highest velocities are located near the boundaries, in areas where pressure gradients are high (Figure 6-1). The figure also shows the presence of non-connected fractures with small velocities. In general, fluid velocities are proportional to the transmissivity and the connectivity of the fractures: fractures well connected with the regional fracture system present higher velocities than the poorly connected fractures. Poorly connected fractures are found in the central part of the domain with fluid velocities lower than 1.0×10^{-11} m/s (green and blue fractures in Figure 6-2).

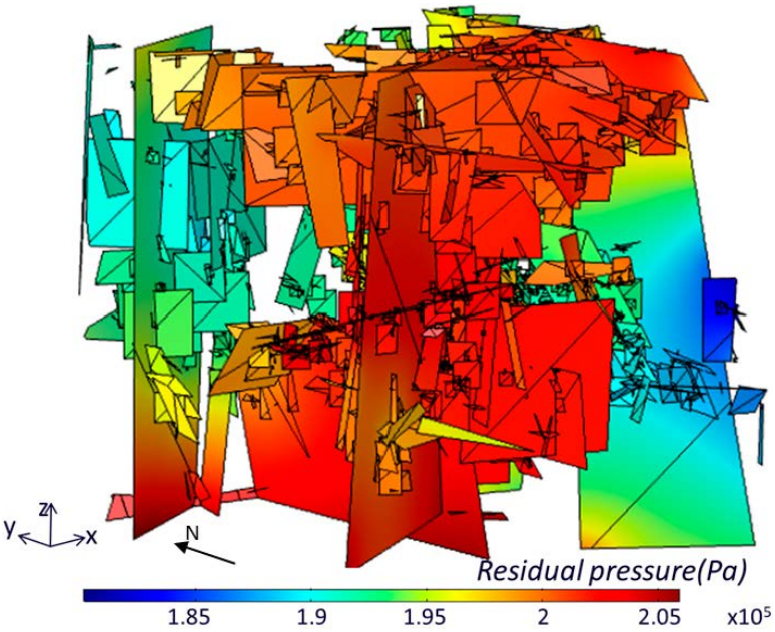

Figure 6-1. *Computed residual pressure distribution at the fractures for the BHA model with boundary conditions from the regional model. The y axis points North.*

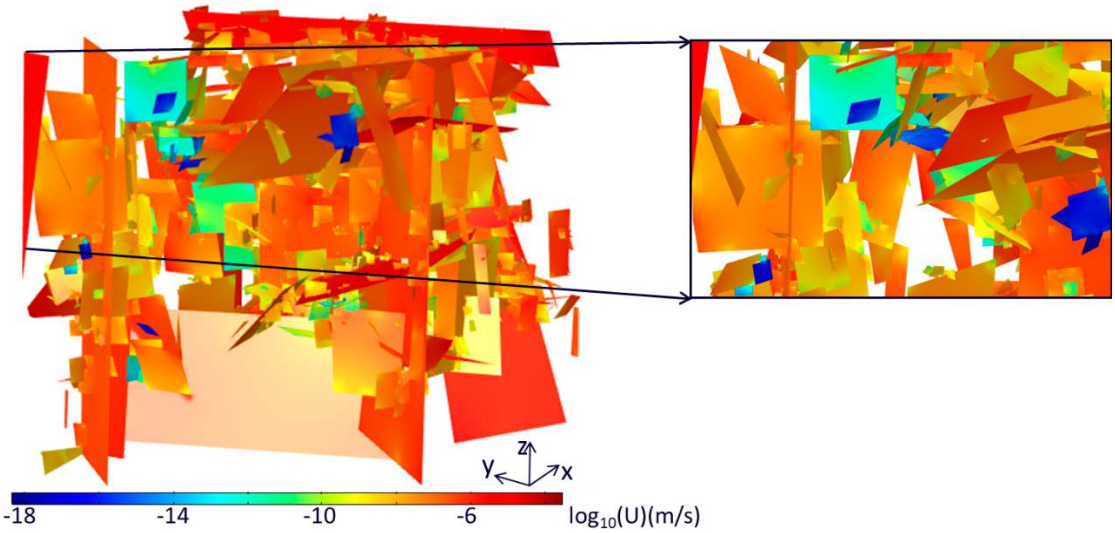

Figure 6-2. *Magnitude of the Darcy velocity at the fractures. Fractures with almost zero Darcy velocity are shown in blue.*

Figure 6-3, Figure 6-4 and Figure 6-5 illustrate the flow field at the BHA/rock interface. Figure 6-3 shows the residual pressure in the fractures intersecting the BHA vault. The pressure distribution determines the inflow and outflow areas. Water enters the vault through the fractures at the south-west interface and exits through the fractures at the north-east interface. Several minor fractures intersecting the vault do not have a significant pressure gradient and are dead-end zones with almost stagnant water. Figure 6-4 shows the Darcy velocity at the BHA/rock interface. The highest velocities, observed in the southern and northern part of the BHA, correspond to the main inflow and outflow areas, respectively. The fractures that are poorly connected do not influence the groundwater flow. Figure 6-5 shows the groundwater flow paths inside the BHA. The figure illustrates how most water enters the domain through a set of fractures intersecting the vault at the south-west interface. The water subsequently flows through the waste domain and leaves the vault through the fractures located in the north part of the vault. Within the vault the groundwater is channelled through the high permeable waste domain from south to north.

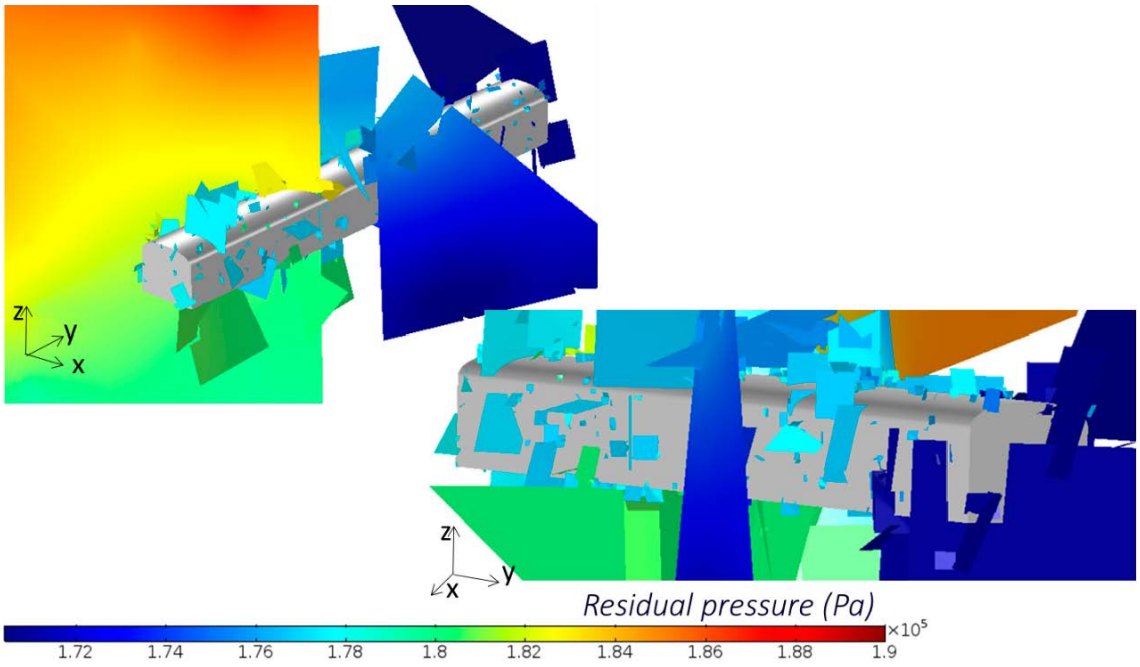

Figure 6-3. *Two views of the residual pressure in the fractures intersecting the BHA vault. The y axis points North.*

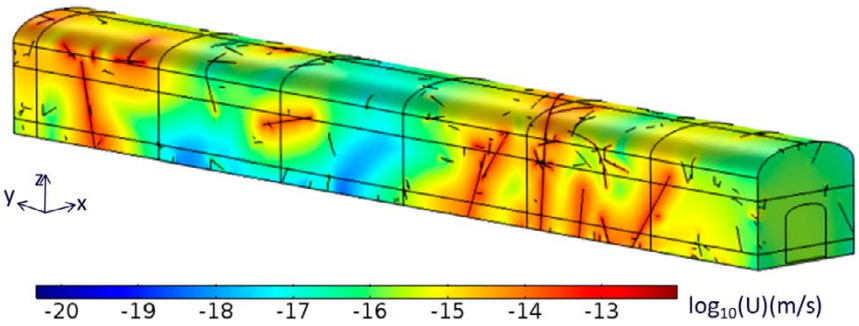

Figure 6-4. *Magnitude of the Darcy velocity on a logarithmic scale. The y axis points North.*

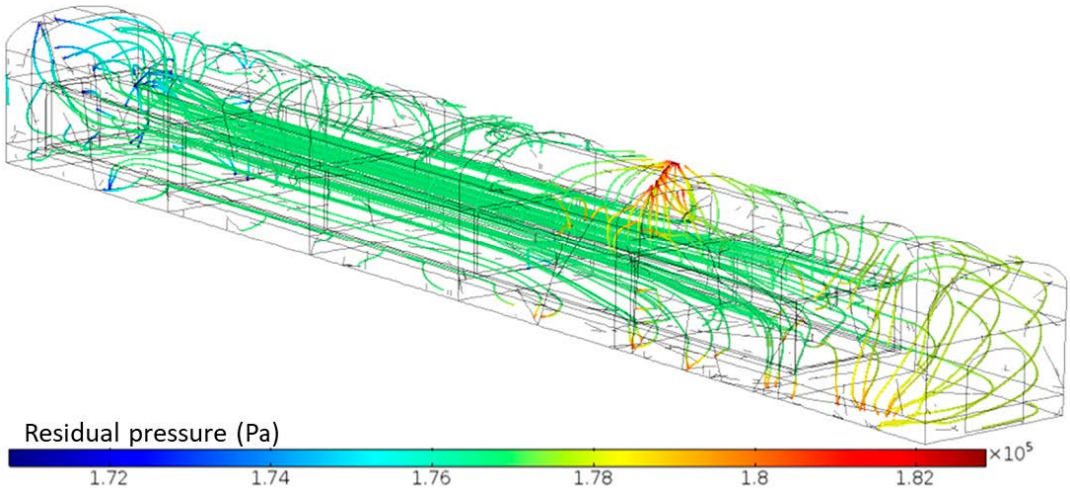

Figure 6-5. *Streamlines crossing the BHA vault from south to north coloured by their residual pressure. The main inflow is indicated by the high pressure and the main outflow by the low pressure at the rock/vault interface.*

6.2 Steady-state conservative transport

A single steady-state transport simulation was carried out to simulate the mass release of a conservative, non-decaying tracer from the waste to the geosphere under a realistic regional flow field. To that end, the transport was simulated using the groundwater flow field obtained from the flow simulation using regional boundary conditions described in the previous section (Section 6.1). The mass flow across the vault/rock interface was evaluated and plotted against the average groundwater flow at the interface in the same way as in Section 5.2 and the result is shown in Figure 6-6. The result falls on the empirical curve calculated to fit the results of the model with generic boundary conditions (Section 5.2). As shown in the figure, the flow conditions in the model with regional boundary conditions lie between the regions of Advection in DFN and Diffusion through bentonite defined in Section 5.2. Thus, the release in the model with regional boundary conditions is controlled by advection in the DFN and diffusion through the bentonite.

6.3 Transient reactive transport considering linear sorption and first order decay

This section presents the results of a transient transport simulation of a non-sorbing non-decaying tracer, ^{36}Cl, ^{93}Mo and ^{135}Cs. The transport simulations were carried out under the groundwater flow field obtained from the simulation using regional boundary conditions (Section 6.1). The model considers radioactive decay of the radionuclides and sorption of caesium in the bentonite backfill. The tracer and radionuclides concentrations were initially set to 1 mol/m^3 within the waste domain and zero elsewhere. The model simulates the evolution of that mass for 500 000 years which is the time required for the conservative tracer to leave the model domain. A set of simulation times, common for all radionuclides, are illustrated in the following sections. The times were chosen to facilitate the comparison of the behaviour of each of them.

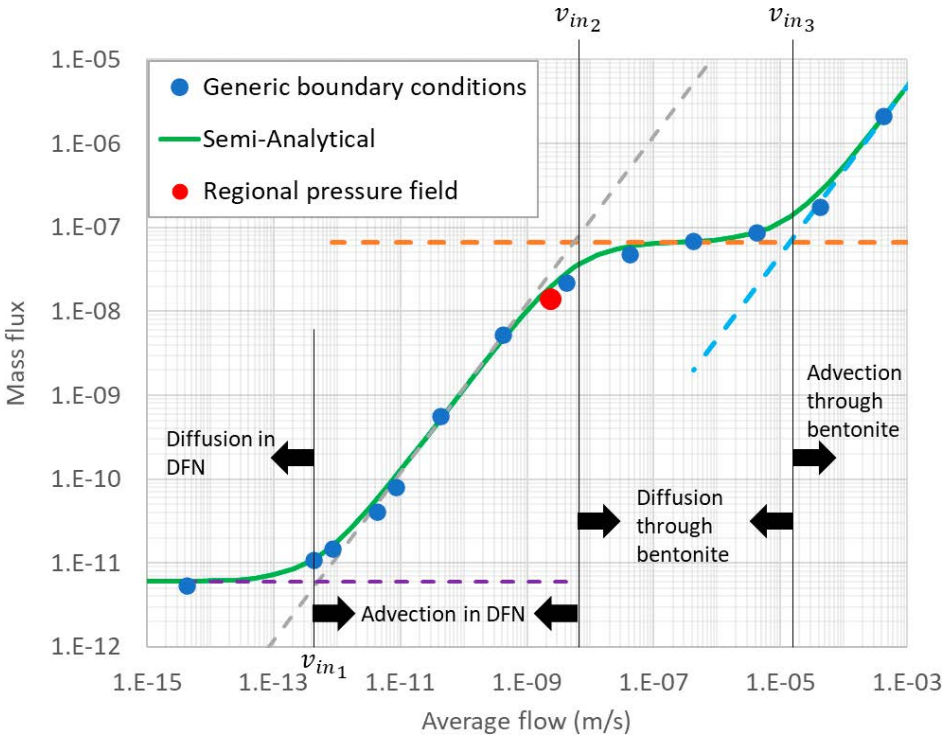

Figure 6-6. *Comparison between the mass flow and average flow obtained with the boundary conditions of the regional model (red dot) and the results of the simulations with generic boundary conditions(blue dots) and the empirical expression (4-3). with the values of the parameters reported in Table 5-3 (green line).*

6.3.1 Non-decaying conservative tracer

Figure 6-7 shows the spatial distribution of the tracer both in the vault and the fractures at three simulation times: 1 000 years, 200 000 years, and 500 000 years. The tracer initially diffuses out from the waste into the bentonite towards the fractured rock where it is released into the fractures. At the same time, the concentration in the vault also decreases due to mixing with the water entering the bentonite through fractures intersecting the vault. The most substantial dilution occurs at the water inlet areas located in the south parts of the vault.

As the tracer is released from the vault a tracer plume is formed in the fractures connected to the north-east vault boundary as most of the tracer follows the regional groundwater flow field. The tracer also diffuses into the dead-end fractures near the vault where it is stored and will later be released back as the concentration in the vault decreases with time. After 500 000 years of simulation 95 % of the tracer has left the model domain.

Figure 6-8 shows in orange the evolution of the tracer mass in the vault (Equation (3-34)), in grey the fractures (Equation (3-33)) and, in yellow, the accumulated mass that leaves the domain through the external boundaries (Equation (3-35)). The mass stored in the fractures is orders of magnitude lower than the mass stored in the vault.

Figure 6-9 (top left) shows the breakthrough curves of the tracer at the backfill/fracture interface and at the model boundaries. The time shift in the peaks of the two breakthrough curves gives an estimate of the residence time in the DFN. The shift is of the order of the output resolution for later times (50 years), but it is difficult to give a more precise estimate. By looking at the first arrival at the model boundaries, it can be approximated to be 30 years. This residence time is small compared to the residence time in the porous medium within the vault.

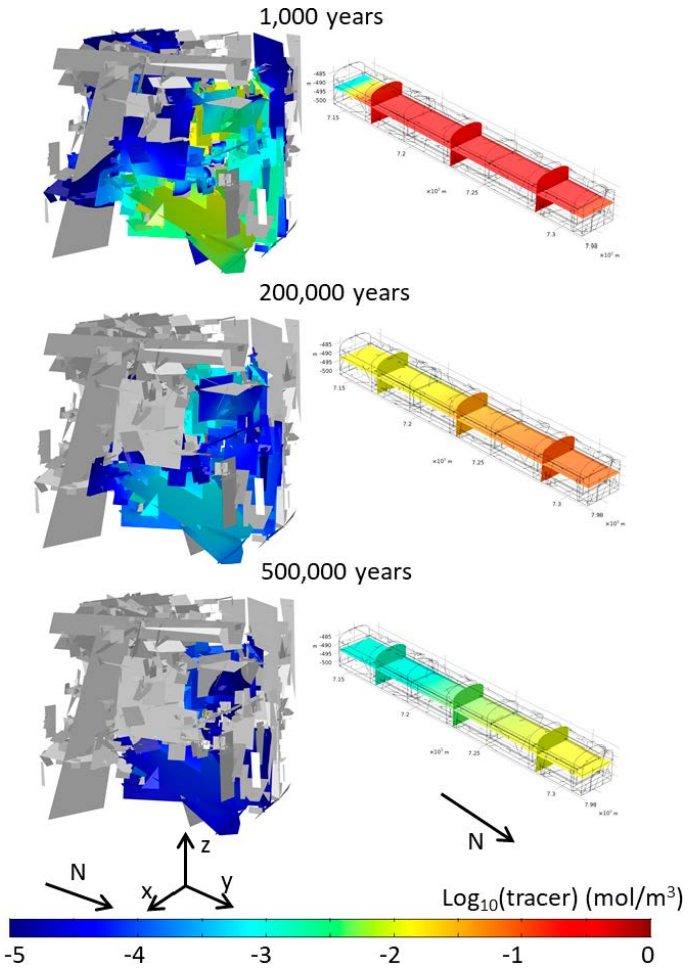

Figure 6-7. *Distribution of the non-decaying conservative tracer concentration in the fractures (left) and in the vault (right) at three simulation times. Only concentration values greater than 1×10^{-5} are shown in the fractured domain.*

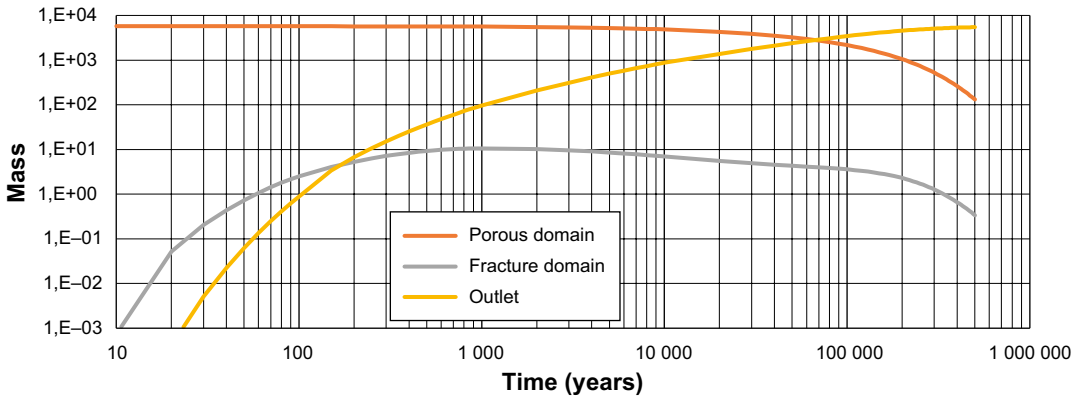

Figure 6-8. *Temporal evolution of the mass of tracer in the porous medium within the vault (orange), the fractures (grey) and the accumulative mass that has left the domain through its boundaries (yellow). The sum of the three components equals the initial mass of the tracer in the waste.*

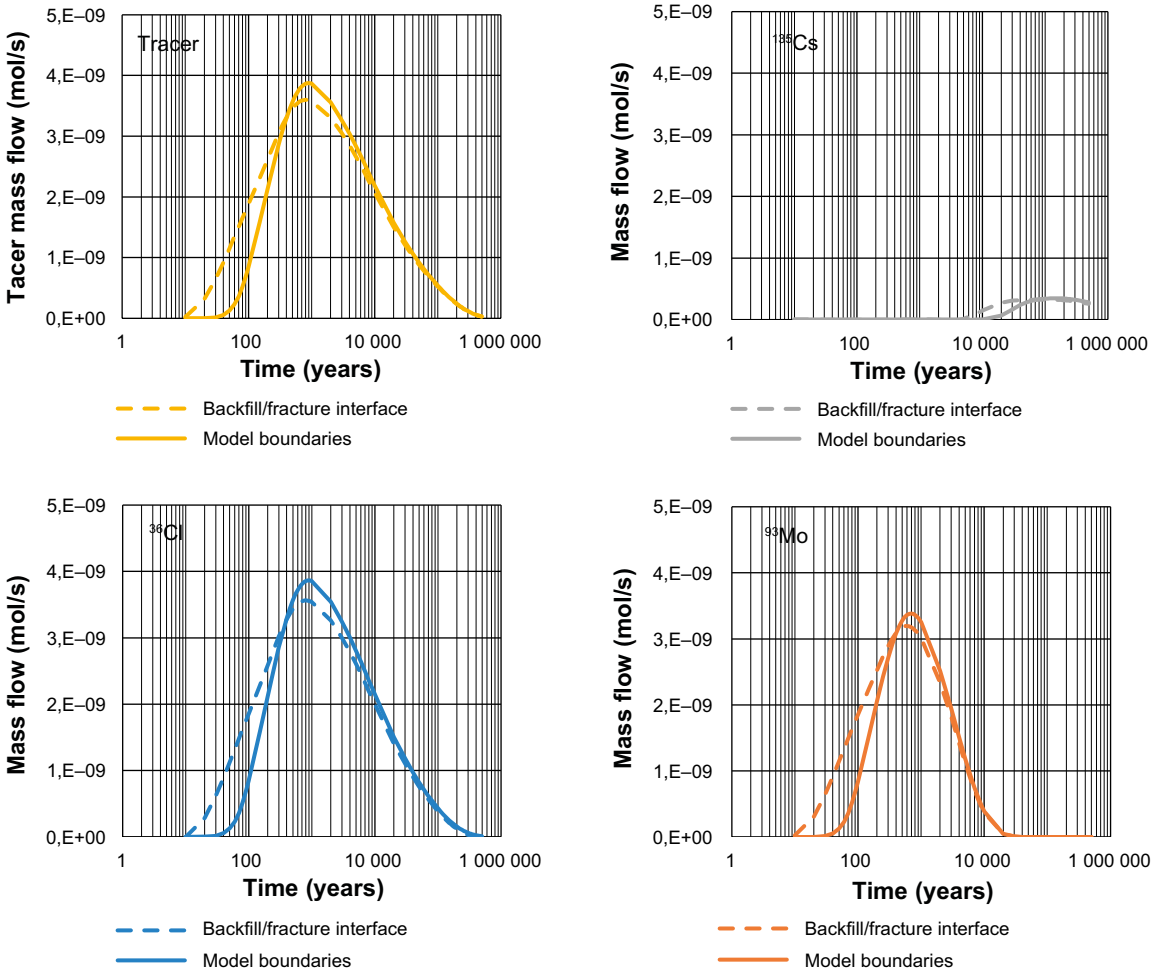

Figure 6-9. *Breakthrough curves of a non-reactive non-decaying tracer, ^{36}Cl, ^{93}Mo, and ^{135}Cs at the backfill/fracture interface and at the model boundaries.*

6.3.2 ^{36}Cl

The radionuclide ^{36}Cl closely follows the evolution of the non-decaying tracer. Figure 6-10 shows the behaviour of ^{36}Cl in both the vault and the fractures. The extension of the chloride plume is almost identical to the tracer plume for early simulation times. However, at later times the ^{36}Cl concentration decreases slightly due to radioactive decay. Even though the half-life of ^{36}Cl is long (301 000 years), visual differences between the tracer and chloride distribution can be observed for simulation times of 200 000 and 500 000 years. The difference is evident both in the vault and in the fractures (Figure 6-7 and Figure 6-10), note that the vault on the right side of Figure 6-10 has a different orientation than in Figure 6-7. After 500 000 years, only 0.7 % of the initial ^{36}Cl mass remains in the model domain. The rest of the mass has either left the domain through the external boundaries (77 %) or has disappeared by radioactive decay (22.3 %).

Figure 6-11 shows the evolution of the ^{36}Cl mass in the vault (orange), in the fractures (grey) and the cumulated mass that leaves the domain through the external boundaries (yellow). The dashed line shows the results for the tracer for comparison. The effects of decay start to become observable after 5 000 simulation years when the mass of ^{36}Cl in the vault is reduced compared to the corresponding tracer mass. The cumulative mass of ^{36}Cl leaving the domain is also reduced due to radioactive decay.

Figure 6-9 (bottom left) shows the breakthrough curves of ^{36}Cl at the backfill/fracture interface and at the model boundaries. Based on the time shift in the peaks of the two breakthrough curves and looking at the first arrival at the model boundaries, the residence time of ^{36}Cl in the DFN is approximately 30 years. This residence time is small compared with the residence time in the porous medium within the vault.

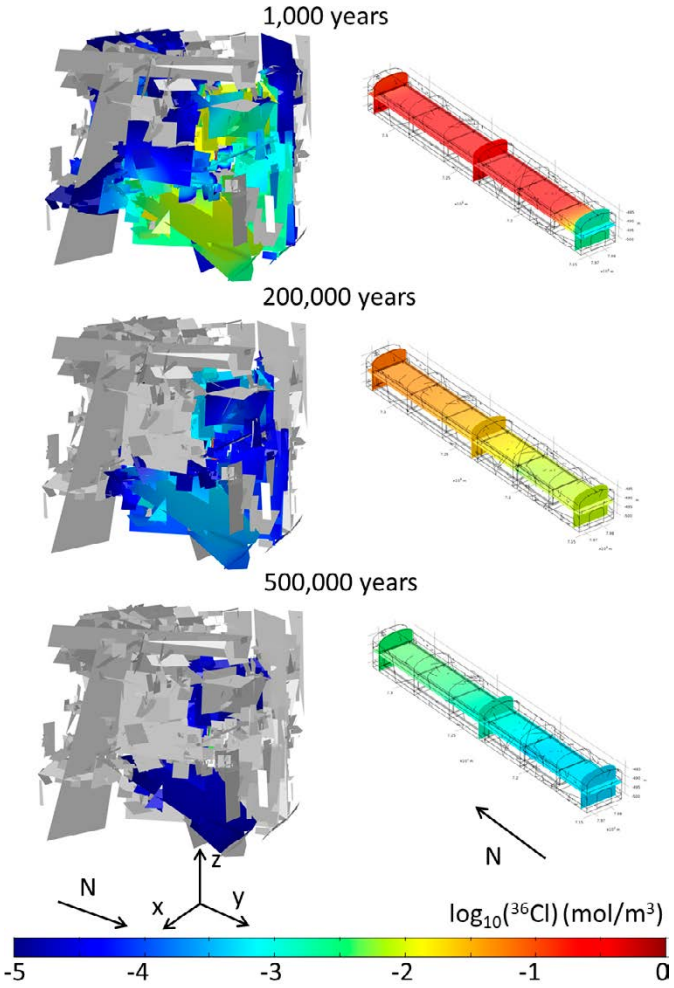

Figure 6-10. *Distribution of the ^{36}Cl concentration in the fractures (left) and in the vault (right) at three simulation times. Only concentration values greater than 1×10^{-5} are shown in the fractured domain.*

Figure 6-11. *Temporal evolution of the mass of ^{36}Cl in the porous medium within the vault (orange), the fractures (grey) and the cumulative mass that has left the domain through its boundaries (yellow). The dashed lines are the corresponding quantities for the non-decaying non sorbing tracer.*

6.3.3 ^{93}Mo

The radionuclide ^{93}Mo is characterized by a relatively short half-life (4 000 years). Figure 6-12 shows the behaviour of ^{93}Mo in both the vault and the fractures. The spatial distribution of the ^{93}Mo concentration after 1 000 years of simulation is similar to that of the tracer and ^{36}Cl. However, at 200 000 and 500 000 years, most of the ^{93}Mo has decayed because of its short half-life. After 500 000 years, less than 0.01 % of the initial ^{93}Mo mass remains in the model domain. Some of the mass has left the domain through the external boundaries (8 %) but most has decayed within the domain (91.5 %).

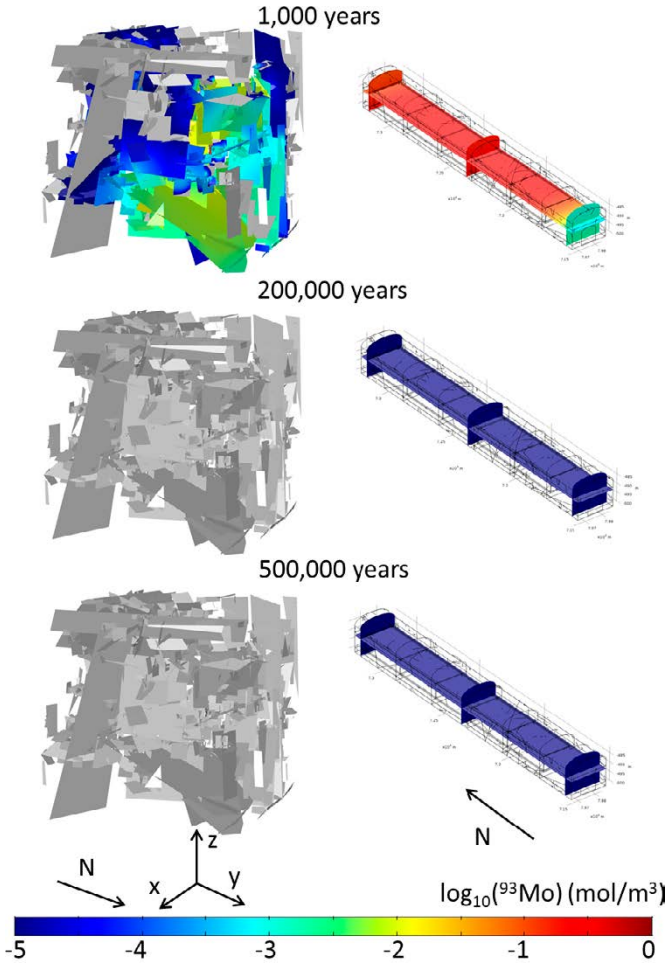

Figure 6-12. *Distribution of the ^{93}Mo concentration in the fractures (left) and in the vault (right) at three simulation times. Only concentration values greater than 1×10^{-5} are shown in the fractured domain.*

Figure 6-13 shows the evolution of the ^{93}Mo mass in the vault (orange), in the fractures (grey) and the cumulated mass that leaves the domain through the external boundaries (yellow). The cumulative outflow of ^{93}Mo reaches a steady-state after 20 000 years which shows that after 20 000 years the radionuclide has decayed before reaching the model boundaries. The dashed lines in Figure 6-13 shows the corresponding results for the tracer for comparison.

Figure 6-9 (bottom right) shows the breakthrough curves of ^{93}Mo at the backfill/fracture interface and at the model boundaries. Based on the time shift in the peaks of the two breakthrough curves and looking at the first arrival at the model boundaries, the residence time of ^{93}Mo in the DFN is approximately 30 years, similar to that of ^{36}Cl and of the tracer. This residence time is small compared with the residence time in the porous medium within the vault.

6.3.4 ^{135}Cs

The radionuclide ^{135}Cs is characterized by its large affinity to adsorb in the bentonite interlayers. Therefore, a high retardation in the backfill of the BHA vault is expected. The sorption of ^{135}Cs in bentonite is simulated using a linear sorption coefficient and the value of the distribution coefficient in the bentonite, K_d, used for caesium is 0.11 m^3/kg. ^{135}Cs also decays slowly, with a half-life of 2 300 000 years.

The sorption of ^{135}Cs in the bentonite accumulates the radionuclide in the backfill and delays its release from the vault. Figure 6-14 shows the spatial distribution of the ^{135}Cs concentration in both the vault and the fractures. Due the high sorption capacity in the bentonite, after 1 000 years of simulation, the caesium has not reached the geosphere. After 200 000 years, the extension of the ^{135}Cs plume in the fractures is similar to the extension of the non-adsorbing tracer. However, the concentration is lower than for the non-adsorbing tracer. After 500 000 simulation years, 83.3 % of the ^{135}Cs remains sorbed inside the vault, 2.7 % has left the model domain through the external boundaries, less than 0.5 % of the initial mass of caesium remains dissolved in the domain and 13.6 % has decayed.

Figure 6-15 shows the evolution of the mass of dissolved ^{135}Cs in the model domain. The mass of dissolved ^{135}Cs in the vault (orange line) initially decreases as ^{135}Cs becomes sorbed in the backfill. The sorption retards the transport of ^{135}Cs and, therefore, the arrival of ^{135}Cs to the model domain boundaries is delayed.

The cumulated ^{135}Cs mass that leaves the domain through the external boundaries (yellow solid line) is increasing at much later times compared with the corresponding quantity for the non-sorbing tracer. This difference is highlighted in Figure 6-15. In addition to the sorption in the bentonite, ^{135}Cs is also affected by decay. Although the half-life of this radionuclide is long, the retardation produced by the sorption enhances the effect of the radioactive decay. After 500 000 years of simulation, 83 % of the initial mass remains in the domain and therefore, the impact of the decay would increase for longer simulation times.

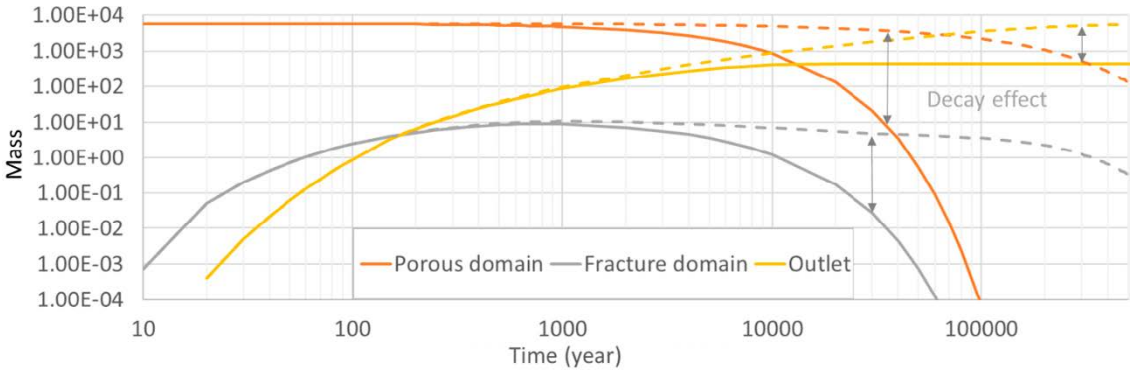

Figure 6-13. *Temporal evolution of the mass of ^{93}Mo in the porous medium within the vault(orange), the fractures (grey) and the cumulative mass that has left the domain through its boundaries (yellow). The dashed lines are the corresponding quantities for the non-decaying non sorbing tracer.*

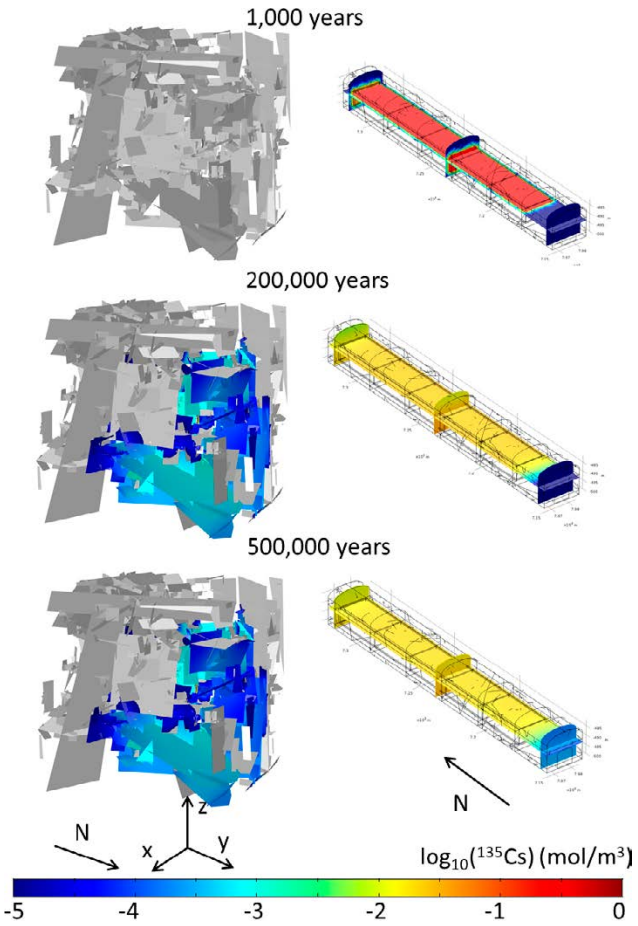

Figure 6-14. *Distribution of the ^{135}Cs concentration in the fractures (left) and in the vault (right) at three simulation times. Only concentration values greater than 1×10^{-5} are shown in the fractured domain.*

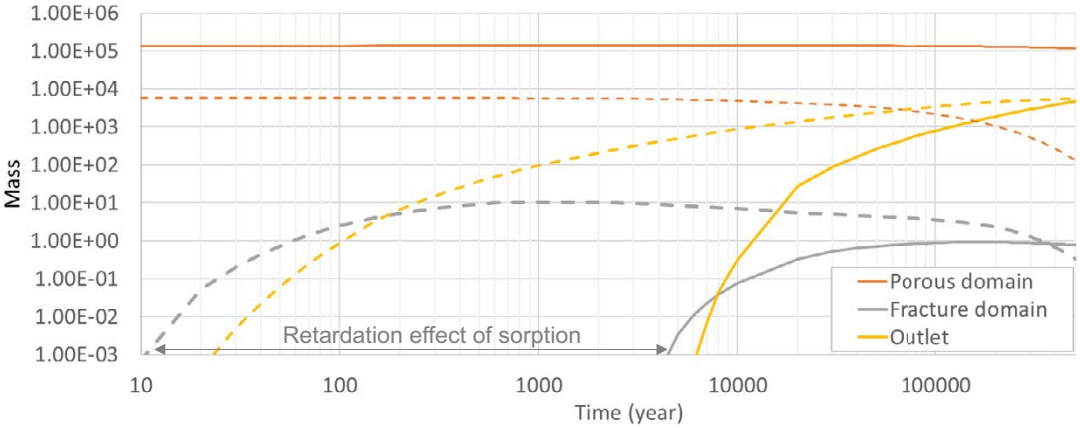

Figure 6-15. *Temporal evolution of the mass of ^{135}Cs in the porous medium within the vault (orange), the fractures (grey) and the cumulative mass that has left the domain through its boundaries (yellow). The dashed lines are the corresponding quantities for the non-decaying non sorbing tracer.*

Figure 6-9 (top right) shows the breakthrough curves of ^{135}Cs at the backfill/fracture interface and at the model boundaries. Based on the time shift in the peaks of the two breakthrough curves and looking at the first arrival at the model boundaries, the residence time of ^{135}Cs in the DFN is approximately 5 000 years, much larger than that of ^{36}Cl and of the tracer. The long residence time of ^{135}Cs in the DFN is due to the very low concentration released from the bentonite backfill to the rock and, therefore, the very slow diffusion through the fracture network.

7 Summary and conclusions

A model for radionuclide transport in the SFL near-field that consistently couples flow and mass transport to the far-field has been developed. This model includes the DFN of the fractured rock and the porous materials of the engineered barrier system with the objective of improving the system and process understanding at the interface between the rock and vaults. This interface is critical to defining the radionuclide source for the assessment models.

This report presents a simplified generic model and a vault-scale model of BHA. For the vault-scale BHA model both generic boundary conditions and more realistic boundary conditions extracted from the a regional-scale hydrogeological model (Joyce et al. 2019) has been applied. The mass transport simulations include linear sorption in the bentonite backfill and radioactive decay. The models are used to simulate the release from the waste to the geosphere of ^{36}Cl, one of the main contributors to the dose in SFL, ^{93}Mo as representative of a relatively rapidly decaying radionuclide and ^{135}Cs as representative of a long-lived radionuclide that is strongly sorbed in bentonite and a non-decaying non-sorbing tracer.

The simplified model is used to verify the implementation of the coupling between the fractured rock represented by a discrete fracture and the vault represented by a CPM. The results obtained from the simplified model are compared with the ones obtained with a corresponding model where the single fracture is represented as a 3D porous medium. The simplified model is based on the one reported in Wessely and Shahkarami (2019). This model is useful to understand how the release from the vault to the fractured rock changes with water flow velocity and the model has been used to calculate the release for a wide range of flow velocities. Also, for the vault-scale BHA model, the release from the vault has been calculated for a wide range of flow velocities by applying generic boundary conditions. For both models, the release from the vault as a function of the flow velocity follows the same trend.

For both models four regions can be differentiated according to the water inlet velocity.

- Diffusion in the DFN. When the water flow through a fracture or fracture network is slow the water is almost stagnant, and then the transport is dominated by diffusion through the fractures in the host rock. For sufficiently low fluid velocities the calculated mass flow corresponds to a constant purely diffusive flux forced by the model boundary conditions. If the distance between the source and the boundary tends to infinity, this flux would approach zero.
- Advection in the DFN. In this region the conceptual model for the mass release from the vault corresponds to the concept of Q_{eq} as defined in previous studies (Neretnieks 1980, Neretnieks et al. 1987). For both the simplified and the vault-scale models, the calculated release from the vault increases linearly with the water velocity within this region, which is not in agreement with the conceptual model as presented in Wessely and Shahkarami (2019). Their model contained a dependence on the square-root of the velocity instead of linear. The Q_{eq} is given by the magnitude of the water flow in the fracture or fractures around the backfill that advectively transport radionuclides diffusing into the fracture or fractures. However, the concept of Q_{eq} has previously been defined for infinitely large fractures, which is not the case of the model presented here. For small factures, Q_{eq} is limited by the flow of water through the fractures connected to the vault and the linear relationship between the mass flow and the groundwater velocity, suggest that the critical factor in this velocity range is the advective transport through the fracture network. The concept of Q_{eq} assumes that the fractures connected to the vault have sufficient capacity to carry all the solute that leaves the repository to ensure a very small concentration of solute in the fractures not directly connected to the vault. This assumption is valid when the fractures have a sufficient flow of water to dilute the solute concentration diffusing from the backfill. However, both in the simple and the vault-scale BHA models the fractures intersecting the vault do not have an infinite extent and water volume flowing through them is limited. In this case, the dilution is not as efficient as assumed by the Q_{eq} term. Therefore, the concentration gradient within the fractures connected to the vault is smaller than the anticipating by the Q_{eq} concept and the resulting mass release is reduced.

- Diffusion through the bentonite. In this region, transport is limited by the diffusion through the backfill, and therefore, the mass flow is almost independent of the water flow velocity. The mass release from the vault is, in this region, governed by the transport resistance of the backfill.
- Advection through the bentonite. For sufficiently high flow velocities the radionuclide release is characterized by the advective flow forced through the bentonite backfill. For both the simplified and the vault-scale models the calculated release from the vault increases linearly with the water velocity within this region.

From the observed relation between the release from the vault and the flow it is concluded that the conceptual model as presented in Wessely and Shahkarami (2019) does not seem to be applicable for the whole range of water velocities for the systems studied.

The simple expression for the release from a vault proposed in Wessely and Shahkarami (2019) is based on the Q_{eq} concept. The expression reproduces well the release at high groundwater velocities; however, it fails to represent the observed behaviour in the case of low groundwater flow velocities. A modification of the expression proposed by Wessely and Shahkarami (2019) that fits the model results over the whole range of groundwater velocities studied in this project is presented. The simulations presented in this report indicate that for a vault intersected by many small fractures the traditional Q_{eq} concept needs to be revised.

The vault-scale BHA model is also used to evaluate the radionuclide release under the regional groundwater flow field of the study area. To that end, it has been solved using regional hydraulic boundary conditions taken from the regional model described by Joyce et al. (2019). The result falls on the empirical curve obtained from the results of the model with generic boundary conditions (Section 5.2). The characteristic flow conditions situate the release between the regions of Advection in the DFN and Diffusion through bentonite. Thus, the release in the model with regional boundary conditions is controlled by the advection in the DFN and diffusion through the bentonite.

The vault-scale BHA model is used to simulate the release of four chemical species: a non-decaying non-sorbing tracer, ^{36}Cl, ^{93}Mo and ^{135}Cs for 500 000 years (Figure 7-1). The model considers radioactive decay of the radionuclides and sorption of caesium in the bentonite of the backfill. Results show that the residence time in the fractures is very small compared with the residence time in the vault and that the movement of the dissolved tracer in the vault is governed by diffusion whereas the movement in the fractures is governed by advection. The decay and adsorption to the bentonite of the radionuclides reduces the cumulative release from the vault. The calculated cumulative release after 500 000 years is 91.9 %, 73.9 %, 7.2 % and 3.28 % for the non-decaying non sorbing tracer, ^{36}Cl, ^{93}Mo and ^{135}Cs respectively

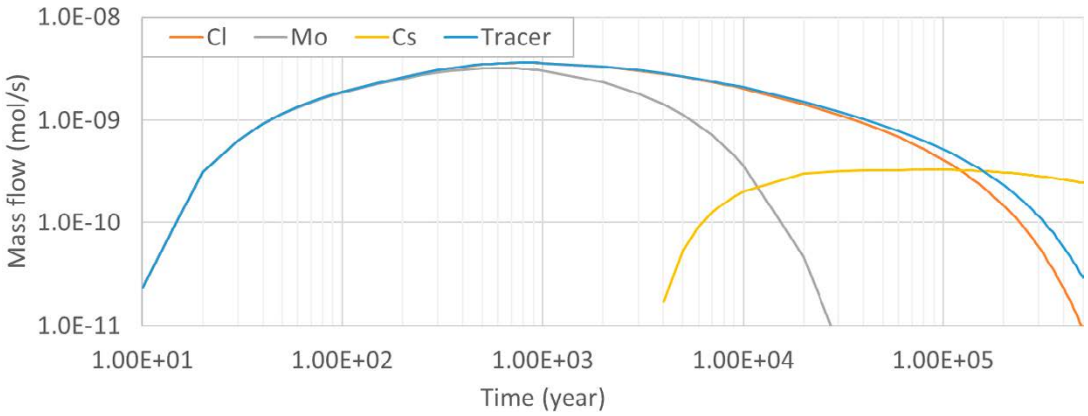

Figure 7-1. *Breakthrough curves evaluated at the backfill/fracture interface for the different dissolved species considered in the simulation.*

References

SKB's (Svensk Kärnbränslehantering AB) publications can be found at www.skb.com/publications.

Abarca E, Idiart A, de Vries L M, Silva O, Molinero J, von Schenck H, 2013. Flow modelling on the repository scale for the safety assessment SR-PSU. SKB TR-13-08, Svensk Kärnbränslehantering AB.

Abarca E, Sampietro D, Miret M, von Schenck H, 2016. Initial modelling of the near-field hydrogeology. Exploring the influence of host rock characteristics and barrier properties. Report for the safety evaluation SE-SFL. SKB R-16-02, Svensk Kärnbränslehantering AB.

Abarca E, Sampietro D, Molinero J, von Schenck H, 2019. Modelling of the near-field hydrogeology – temperate climate conditions. Report for the safety evaluation SE-SFL. SKB R-19-03, Svensk Kärnbränslehantering AB.

Bauer P, Attinger S, Kinzelbach W, 2001. Transport of a decay chain in homogenous porous media: analytical solutions. Journal of Contaminant Hydrology 49, 217–239.https://doi.org/10.1016/S0169-7722(00)00195-9

Bazrafkan S, Matthai S K, Mindel J E, 2014. The Finite-Element-Centered Finite-Volume Discretization Method (FECFVM) for multiphase transport in porous media with sharp material discontinuities. In Proceedings of the ECMOR XIV – 14th European Conference on the Mathematics of Oil Recovery, September 2014. European Association of Geoscientists & Engineers, 1–22. https://doi.org/10.3997/2214-4609.20141841

Bear J, 1972. Dynamics of fluids in porous media. New York: Elsevier.

Berkowitz B, 2002. Characterizing flow and transport in fractured geological media: A review. Advances in Water Resources 25, 861–884. https://doi.org/10.1016/S0309-1708(02)00042-8

Berkowitz B, Scher H, 1997. Anomalous transport in random fracture networks. Physical Review Letters 79, 4038–4041. https://doi.org/10.1103/PhysRevLett.79.4038

Berkowitz B, Scher H, 1998. Theory of anomalous chemical transport in random fracture networks. Physical Review E 57, 5858. https://doi.org/10.1103/PhysRevE.57.5858

Carrera J, Sánchez-Vila X, Benet I, Medina A, Galarza G, Guimerà J, 1998. On matrix diffusion: formulations, solution methods and qualitative effects. Hydrogeology Journal 6, 178–190.

Cho C M, 1971. Convective transport of ammonium with nitrification in soil. Canadian Journal of Soil Science 51, 339–350. https://doi.org/10.4141/cjss71-047

COMSOL, 2017. COMSOL Multiphysics. Reference manual, version 5.3. Burlington, MA: COMSOL Inc.

Darcy H, 1856. Les fontaines publiques de la ville de Dijon: exposition et application des principes à suivre et des formules à employer dans les questions de distribution d'eau: ouvrage terminé par un appendice relatif aux fournitures d'eau de plusieurs villes au filtrage des eaux et à la fabrication des tuyaux de fonte, de plomb, de tole et de bitume. Paris: Dalmont. (In French.)

Dentz M, Berkowitz B, 2003. Transport behavior of a passive solute in continuous time random walks and multirate mass transfer. Water Resources Research 39, 1111. https://doi.org/10.1029/2001WR001163

Diersch H-J, 2014. FEFLOW: Finite element modeling of flow, mass and heat transport in porous and fractured media. Berlin: Springer.

Elfwing M, Evins L Z, Gontier M, Grahm P, Mårtensson P, Tunbrant S, 2013. SFL concept study. Main report. SKB TR-13-14, Svensk Kärnbränslehantering AB.

Flemisch B, Berre I, Boon W, Fumagalli A, Schwenck N, Scotti A, Stefansson I, Tatomir A, 2018. Benchmarks for single-phase flow in fractured porous media. Advances in Water Resources 111, 239–258. https://doi.org/10.1016/j.advwatres.2017.10.036

Follin S, Hartley L, Rhén I, Jackson P, Joyce S, Roberts D, Swift B, 2014. A methodology to constrain the parameters of a hydrogeological discrete fracture network model for sparsely fractured crystalline rock, exemplified by data from the proposed high-level nuclear waste repository site at Forsmark, Sweden. Hydrogeology Journal 22, 313–331.

Gelhar L W, Axness C L, 1983. Three-dimensional stochastic analysis of macrodispersion in aquifers. Water Resources Research 19, 161–180.

Gelhar L W, Welty C, Rehfeldt K R, 1992. A critical review of data on field-scale dispersion in aquifers. Water Resources Research 28, 1955–1974.

Hadgu T, Karra S, Kalinina E, Makedonska N, Hyman J D, Klise K, Viswanathan H S, Wang Y, 2017. A comparative study of discrete fracture network and equivalent continuum models for simulating flow and transport in the far field of a hypothetical nuclear waste repository in crystalline host rock. Journal of Hydrology 553, 59–70.https://doi.org/10.1016/j.jhydrol.2017.07.046

Haggerty R, Gorelick S M, 1995. Multiple-rate mass transfer for modeling diffusion and surface reactions in media with pore-scale heterogeneity. Water Resources Research 31, 2383–2400. https://doi.org/10.1029/95WR10583

Haggerty R, McKenna S A, Meigs L C, 2000. On the late-time behavior of tracer test breakthrough curves. Water Resources Research 36, 3467–3479.

Harbaugh A W, Banta E R, Hill M C, McDonald M G, 2000. MODFLOW-2000, The U.S. Geological Survey modular ground-water model – User guide to modularization concepts and the ground-water flow process. Open-File Report 00–92, U.S. Geological Survey.

Hartley L J, Holton D, 2004. CONNECTFLOW (Release 8.0): technical summary document. Serco Report, ERRA/C/TSD02V01, Serco Assurance.

Hjerne C, Nordqvist R, Harrström J, 2010. Compilation and analyses of results from cross-hole tracer tests with conservative tracers. SKB R-09-28, Svensk Kärnbränslehantering AB.

Hyman J D, Karra S, Makedonska N, Gable C W, Painter S L, Viswanathan H S, 2015. dfnWorks: A discrete fracture network framework for modeling subsurface flow and transport. Computers & Geosciences 84, 10–19. https://doi.org/10.1016/j.cageo.2015.08.001

Jackson C P, Hoch A R, Todman S, 2000. Self-consistency of a heterogeneous continuum porous medium representation of a fractured medium. Water Resources Research 36, 189–202.

Jasinski L, Dabrowski M, 2015. Upscaling flow and transport properties in synthetic porous media. EGU General Assembly 2015, Vienna, 12–17 April 2015, id 11645.

Joyce S, Simpson T, Hartley L, Applegate D, Hoek J, Jackson P, Roberts D, Swan D, Gylling B, Marsic N, Rhén I, 2010a. Groundwater flow modelling of periods with temperate climate conditions – Laxemar. SKB R-09-24, Svensk Kärnbränslehantering AB.

Joyce S, Simpson T, Hartley L, Applegate D, Hoek J, Jackson P, Swan D, Marsic N, Follin S, 2010b. Groundwater flow modelling of periods with temperate climate conditions – Forsmark. SKB R-09-20, Svensk Kärnbränslehantering AB.

Joyce S, Appleyard P, Hartley L, Tsitsopoulos V, Woollard H, Marsic N, Sidborn M, Crawford J, 2019. Groundwater flow and reactive transport modelling of temperate conditions. Report for the safety evaluation SE-SFL. SKB R-19-02, Svensk Kärnbränslehantering AB.

Laaksoharju M, Smellie J, Tullborg E-L, Wallin B, Drake H, Gascoyne M, Gimeno M, Gurban I, Hallbeck L, Molinero J, Nilsson A-C, Waber N, 2009. Bedrock hydrogeochemistry Laxemar. Site descriptive modelling, SDM-Site Laxemar. SKB R-08-93, Svensk Kärnbränslehantering AB.

Lei Q, Latham J-P, Tsang C-F, 2017. The use of discrete fracture networks for modelling coupled geomechanical and hydrological behaviour of fractured rocks. Computers and Geotechnics 85, 151–176. https://doi.org/10.1016/j.compgeo.2016.12.024

Miller I, Lee G, Dershowitz W, 2001. MAFIC, Matrix / fracture interaction code with head and solute transport. User documentation, version 2.0. Redmond, WA: Golder Associates Inc.

Milliotte C, Jonoud S, Wennberg O P, Matthäi S K, Jurkiw A, Mosser L, 2018. Well-data-based discrete fracture and matrix modelling and flow-based upscaling of multilayer carbonate reservoir horizons. Geological Society, London, Special Publications 459, 191–210.https://doi.org/10.1144/SP459.7

Neretnieks I, 1980. Transport mechanisms and rates of transport of radionuclides in the geosphere as related to the Swedish KBS concept. In Underground disposal of radioactive wastes: Proceedings of a symposium on the underground disposal of radioactive wastes, Otaniemi, Finland, 2–6 July 1979. Vienna: IAEA, 315–338.

Neretnieks I, Arve S, Moreno L, Rasmuson A, Zhu M, 1987. Degradation of concrete and transport of radionuclides from SFR-repository for low- and intermediate level nuclear waste. SFR 87-11, Svensk Kärnbränslehantering AB.

Nick H M, Matthäi S K, 2011. A hybrid finite-element finite-volume method with embedded discontinuities for solute transport in heterogeneous media. Vadose Zone Journal 10, 299–312. https://doi.org/10.2136/vzj2010.0015

Odsæter L H, Kvamsdal T, Larson M G, 2019. A simple embedded discrete fracture–matrix model for a coupled flow and transport problem in porous media. Computer Methods in Applied Mechanics and Engineering 343, 572–601. https://doi.org/10.1016/j.cma.2018.09.003

Painter S, Cvetkovic V, Mancillas J, Pensado O, 2008. Time domain particle tracking methods for simulating transport with retention and first-order transformation. Water Resources Research 44. https://doi.org/10.1029/2007WR005944

Remy N, Boucher A, Wu J, 2009. Applied geostatistics with SGeMS: a user's guide. Cambridge: Cambridge University Press.

Renard P, de Marsily G, 1997. Calculating equivalent permeability: a review. Advances in Water Resources 20, 253–278. https://doi.org/10.1016/S0309-1708(96)00050-4

Silva O, Carrera J, Dentz M, Kumar S, Alcolea A, Willmann M, 2009. A general real-time formulation for multi-rate mass transfer problems. Hydrology and Earth System Sciences 13, 1399–1411.

SKB, 2010a. Model summary report for the safety assessment SR-Site. SKB TR-10-51, Svensk Kärnbränslehantering AB.

SKB, 2010b. Data report for the safety assessment SR-site. SKB TR-10-52, Svensk Kärnbränslehantering AB.

SKB, 2011. Long-term safety for the final repository for spent nuclear fuel at Forsmark. Main report of the SR-site project. SKB TR-11-01, Svensk Kärnbränslehantering AB.

SKB, 2014. Data report for the safety assessment SR-PSU. SKB TR-14-10, Svensk Kärnbränslehantering AB.

SKB, 2019. Post-closure safety for a proposed repository concept for SFL. Main report for the safety evaluation SE-SFL. SKB TR-19-01, Svensk Kärnbränslehantering AB.

Soler J M, Neretnieks I, Moreno L, Liu L, Meng S, Svensson U, Iraola A, Ebrahimi H, Trinchero P, Molinero J, Vidstrand P, Deissmann G, Říha J, Hokr M, Vetešnik A, Vopálka D, Gvoždik L, Polák M, Trpkošová D, Havlová V, Park D-K, Ji S-H, Tachi Y, Ito T, Gylling B, Lanyon G W, 2022. Predictive modeling of a simple field matrix diffusion experiment addressing radionuclide transport in fractured rock. Is it so straightforward? Nuclear Technology 208, 1059–1073.

Svensson U, 2001a. A continuum representation of fracture networks. Part I: Method and basic test cases. Journal of Hydrology 250, 170–186. https://doi.org/10.1016/S0022-1694(01)00435-8

Svensson U, 2001b. A continuum representation of fracture networks. Part II: application to the Äspö Hard Rock laboratory. Journal of Hydrology 250, 187–205. https://doi.org/10.1016/S0022-1694(01)00436-X

Svensson U, Ferry M, 2010. Darcy Tools version 3.4. User's guide. SKB R-10-72, Svensk Kärnbränslehantering AB.

Trinchero P, Poteri A, Gylling B, Selroos J-O, 2020. Modelling the water phase diffusion experiment at Onkalo (Finland): Insights into the effect of channeling on radionuclide transport and retention. Journal of Hydrology 590, 125399.

Vidstrand P, Rhén I, Zugec N, 2010. Groundwater flow modelling of periods with periglacial and glacial climate conditions – Laxemar, SKB R-09-25, Svensk Kärnbränslehantering AB.

von Schenck H, Kautsky U, Gylling B, Abarca E, Molinero J, 2015. Advancing the modelling environment for the safety assessment of the Swedish LILW repository at Forsmark. MRS Online Proceedings Library 1744, 223–228.

Wessely O, Shahkarami P, 2019. Development of radionuclide transport models for the near-field. Report for the safety evaluation SE-SFL. SKB R-19-05, Svensk Kärnbränslehantering AB.

Appendix A

Comparison between the representation of the host rock as a discrete fracture network or as an equivalent porous medium

This report considers a discrete representation of the fractured rock. However models where the host-rock is conceptualized using an equivalent continuous porous medium (ECPM) are often used for safety evaluation in the far and near-field (Vidstrand et al. 2010, Abarca et al. 2016, 2019).

Here, we present an exercise of comparison of groundwater flow simulations using the DFN approach and an ECPM. The ECPM was generated from the same DFN (Figure 3-10) used in the work described in Chapters 5 and 6. The upscaling was performed using DarcyTools (Svensson and Ferry 2010) with a geometric upscaling algorithm over a predefined grid. The ECPMs used have been generated using four grids. The full diagonal permeability tensor was computed. Figure A-1 shows the resulting permeability in the x direction for the upscaling performed over different grids (25, 12.5, 6.25 and 3.125 meters). The upscaling generates ECPMs with a range of permeabilities ranging from 1×10^{-12} to 1×10^{-20} m^2. The minimum permeability has been assigned to be the permeability of the matrix. The lower the upscaling grid size the higher the maximum permeability and the higher the variance of the permeability values. Although the larger upscaling sizes result in lower maximum values of the permeability, they increase the connectivity of the fracture network.

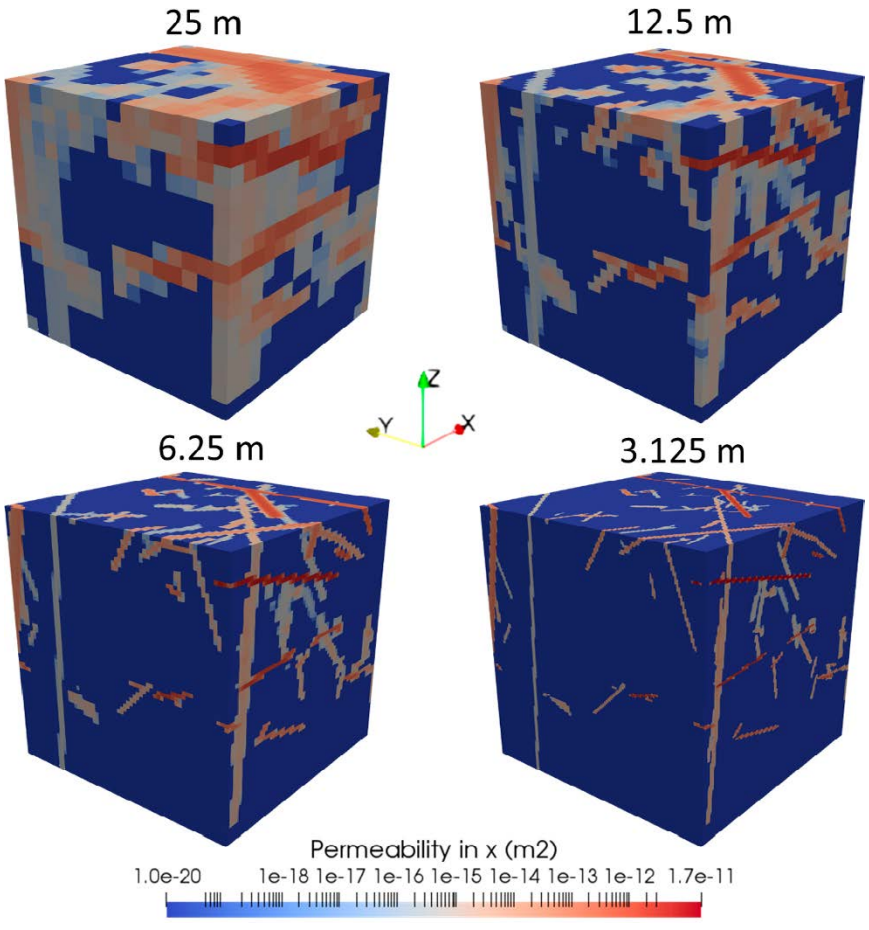

Figure A-1. *Host rock permeability (k_x) of the equivalent continuous porous medium generated in DarcyTools from the discrete fracture network used in the current project and for different grid sizes (25, 12.5, 6.25 and 3.125 meters).*

Figure A-2 shows the vertical distribution of the volume-weighted geometric mean of the permeability for the different upscaling grids. The volume-weighted geometric mean is computed for different xy planes depending on the grid resolution and plotted against the vertical elevation of the plane in Figure A-2. The higher the resolution of the upscaling grid, the lower the geometric mean and the higher the variance of the permeability (Figure A-3). The difference is four orders of magnitude between the more refined and the coarser grids. The ConnectFlow upscaled field generated by Joyce et al. (2019) and used for the near-field hydraulic calculations for the safety evaluation of SFL (Abarca et al. 2019) is included in the Figure A-2 for comparison. It is important to remark that the ConnectFlow and the DarcyTools upscaled fields are not created with the same DFN. In the case of the DarcyTools upscaled field, a subset of the DFN from ConnectFlow is used. This subset corresponds to all the fractures connected to the BHA and the network of fractures connected to those. For that reason, the comparison of the geometric mean between both types of upscaled fields is just illustrative. The resolution of the ConnectFlow upscaled field is not regular (see Figures 4-101 and 4-104 in Joyce et al. 2019). The grid size is 25 m in most of the domain, but it has a higher resolution around the repository (resolution of 5 m between depths of −475 and −525 m). As a result, the ConnectFlow upscaled field has a decrease in the geometric mean of the permeability in the more refined area.

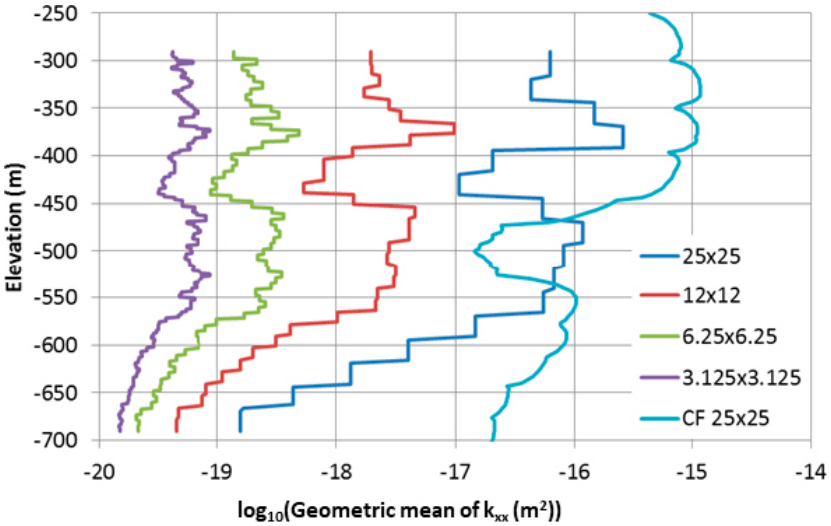

Figure A-2. *Vertical distribution of the volume-weighted geometric mean of the permeability. Legend refers to the upscaling grid size. The grid size in the ConnectFlow (CF) model is not regular. It is 25 m in most of the domain but the resolution increases to 5 m in the repository area between depths of −475 and 515 m.*

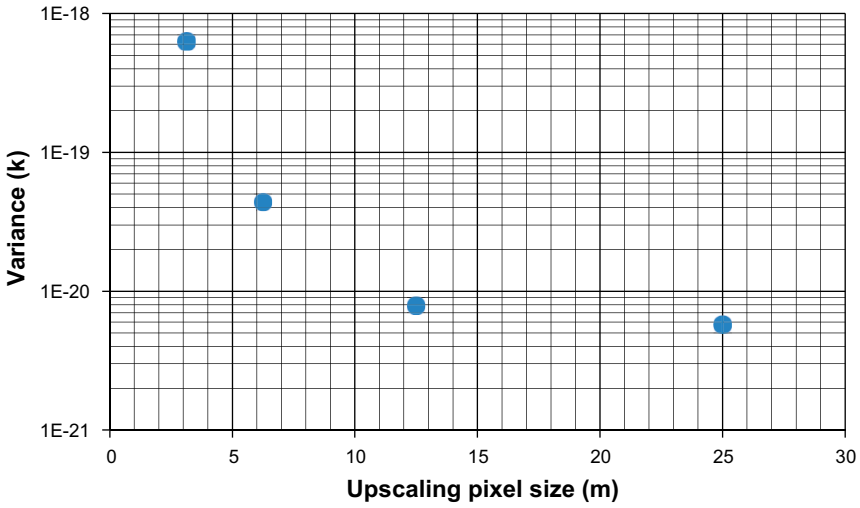

Figure A-3. *Variance of the permeability as a function of the pixel size for the ECPM models created with DarcyTools.*

However, the geometric mean is not representative of the hydraulic behaviour of the domain. In fact, if the equivalent permeability of the whole domain (in the x direction) is evaluated for the 4 grid resolutions in DarcyTools, the resulting values decrease with the grid resolution (Figure A-4), but they are of the same order of magnitude. This result confirms that there is an increase in the connectivity of the fracture network with increasing pixel size. The equivalent permeability is obtained from a simulation that considers a unidirectional flow with a known pressure gradient. Under these conditions, the equivalent permeability of the block can be obtained applying Darcy's law within following form

$$Q_i = \frac{k_{eq,i}S}{\mu}(\nabla p + \rho g \nabla D) \rightarrow k_{eq,i} = \frac{Q_i \mu}{S\,(\nabla p + \rho g \nabla D)}, \qquad \text{(A-1)}$$

where Q_i is the fluid flow (m^3/s) in the i direction, $k_{eq,i}$ (m^2) is the equivalent permeability in the i direction, S is the porous surface where the flow is evaluated (m^2), μ is the fluid viscosity (Pa·s), p is the pressure (Pa), ρ is the fluid density (kg/m^3), g is the acceleration due to gravity (m/s^2) and D is the depth (m).

The BHA vault is included in the model geometry of the cube generated in DarcyTools to replicate the model described in Section 3.4. Two approaches (DFN with Comsol and ECPM with DarcyTools) are used to compute the groundwater flow through the rock volume and through the BHA. The same underlying DFN is used in the Comsol and DarcyTools calculations. The modelled domain consists of a cube with a side length of 400 m, with the BHA vault located at the center (Figure A-5). A fixed pressure gradient between the y- to the y+ faces is assumed, with a pressure 9 810 Pa higher on the y- boundary. No flow was considered at the rest of the boundaries and the model was solved in steady state.

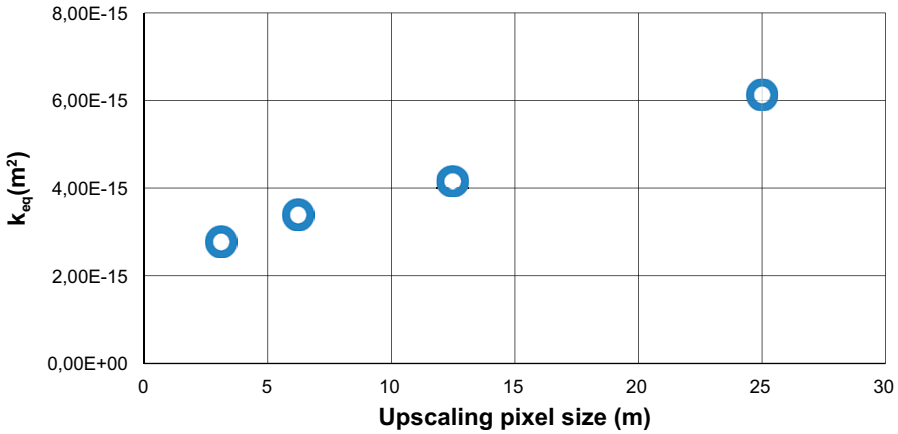

Figure A-4. *Equivalent permeability of the rock block in the x direction computed for upscaled grids with increasing resolution.*

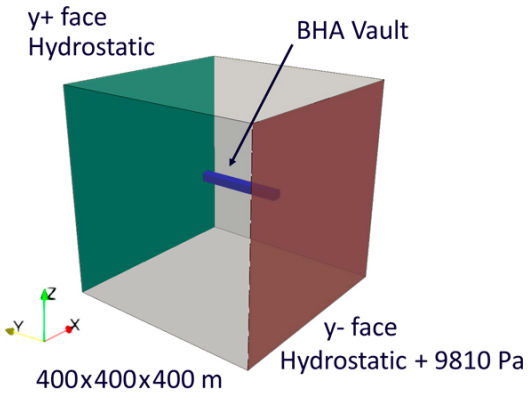

Figure A-5. *Model domain and boundary conditions in the DarcyTools model.*

Various mesh resolutions were tested in both the DFN and ECPM models. In the DFN model, the fractures were discretized with an irregular triangular mesh. Six meshes with a maximum element size of 76, 22, 14, 8, 3 and 1.5 m were simulated. DarcyTools represents the ECPM with a cartesian unstructured grid. Seven ECPM realizations with increasing resolution (cell size of 25, 12.5, 6.25, 3.125, 1.56, 0.78 and 0.39 m) were evaluated (see four of them in Figure A-1). In both models the resolution of the mesh in the BHA was maintained constant throughout the simulations. The maximum element length in the vault and its surroundings is 0.39 m in the ECPMs and around 1.5 m in the DFN model.

The performance of the models was tested by comparing the water inflow (m^3/y) entering the model domain. In both models, the amount of water entering the domain seems to converge when reducing the maximum element size (Figure A-6). However, the convergence behavior is different. The flow goes up with increasing resolution in the DFN model. This increase is related to the way the boundary conditions are imposed and the mesh resolution at those boundaries. The pressure field that is used as boundary conditions is obtained from an ECPM model, so it is not fully consistent with the DFN parameterization. However, the flow differences are under 6 % for the extreme element sizes with the DFN representation of the host rock. This suggest that this approach is robust. The domain inflow differs by 12 % between the two modelling approaches when the maximum element size is below 1.56 m in the ECPM model and 3 m in the DFN model. The differences in the domain inflow between the ECPM and the DFN models increases with the pixel size of the ECPM because larger upscaling pixel size overestimates the connectivity of the rock.

Regarding the water entering the vault (Figure A-7), the computed inflow increases in the ECPM model when the maximum element size is lower than 3.125 m. In those cases, the results of both modelling approaches (DFN and ECPM) strongly differ.

In the DFN model, the vault inflow tends to converge when reducing the mesh element size. The ECPM model follows the same trend when reducing the element size from 25 to 3.125 m. There is a good agreement (6 % variation) between the DFN with a maximum element size of 1.5 m and the ECPM with cells of 3.125 m (Figure A-7). However, unexpectedly, the water inflow increases in the ECPM model with element sizes lower than 3.125 m (1.56, 0.78 and 0.39 m). To analyse whether these results were a consequence of a numerical artefact, a set of changes in the DarcyTools model configurations were carried out.

The model configurations were tested in the ECPM model with a maximum element size of 1.56. The transition between the smaller cells of the vault and the ECPM was modified through the aspect ratio and the blurring factor of the mesh. Various solver parameters were tested. The background matrix permeability was reduced to 1×10^{-25} m^2 to check for a possible effect of the rock matrix. All these simulations resulted in similar vault and domain inflow values. So, no clear explanation has been found for this unexpected increase of water inflow with high-resolution upscaling. It may relate to a change in connectivity along a fracture due to upscaling when the element size is too small. As a result, the cells representing the fracture may become hydraulically disconnected.

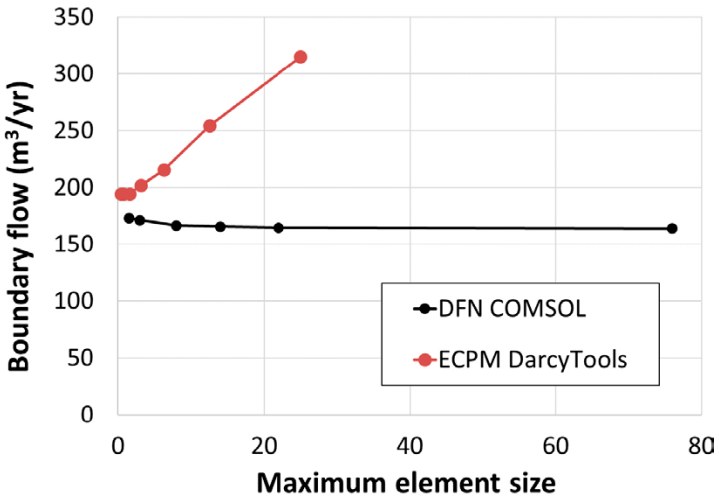

Figure A-6. *Water inflow (m^3/y) entering the domain for the DFN model (black) and for the ECPM realizations (red).*

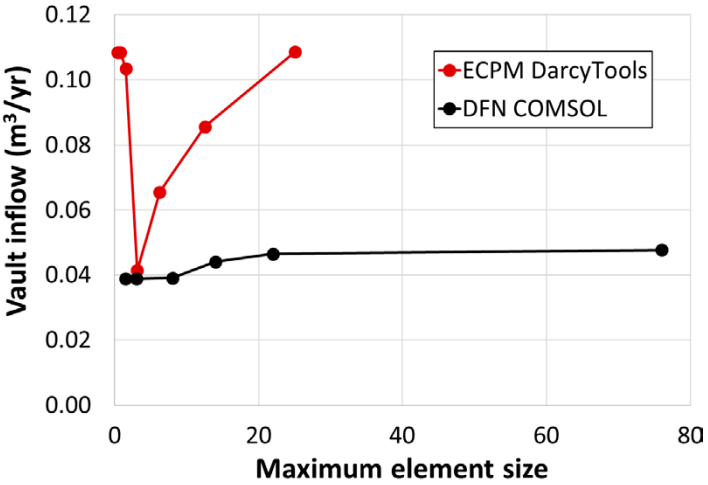

Figure A-7. *Water inflow (m^3/y) entering the vault border for the DFN model (black) and for the ECPM realizations (red).*

This may explain the increase in flow in the ECPM when the element size is reduced below 3.125 m. The equivalent permeability of the vault material in the transverse direction (x axis in Figure A-5) is of around 4.5×10^{-20} m^2. Therefore, if fractures become disconnected during the upscaling, the repository will be the most permeable material in the modelled domain for all the considered cases. Maybe there is a threshold in the upscaling cell size beyond which, i.e., for smaller cells, the upscaling disconnects the connectivity of the fractures.

The velocity field at the rock/BHA interface shows similar patterns with both approaches for the ECPM model with a maximum element size of 3.125 m and the DFN model for the maximum element size of 3 m (Figure A-8). High groundwater flow occurs where highly permeable fractures intersect the vault and when these fractures are connected with the regional network.

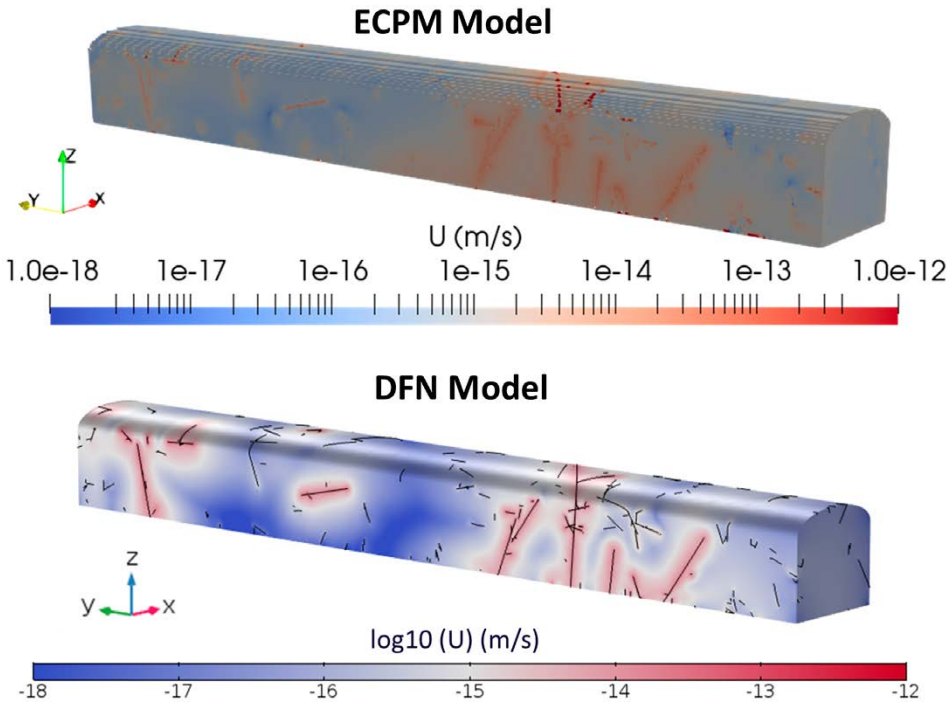

Figure A-8. *Magnitude of the Darcy velocity at the interface BHA/rock for the ECPM model with maximum element size of 3.125 m (top) and the DFN model for the maximum element size of 3 m (bottom).*

Appendix B

Validation of the implementation of the advective-dispersive transport equation with linear sorption and decay

The equations for radionuclide sorption and decay are implemented in Comsol Multiphysics using the physics interface transport of dissolved species in porous media. This appendix describes two benchmark exercises carried out to test the validity of the implemented equations for solving transport in porous media of a decay chain of radionuclides subject to linear adsorption with K_d. The results of the Comsol simulation are compared against the analytical solutions detailed in two papers (Cho 1971, Bauer et al. 2001).

B1 Benchmark 1. Convective transport of ammonium with nitrification in soil (Cho 1971).

B1.1 Problem description

This paper describes the convective transport of ammonium with nitrification and denitrification in soils. The advection-dispersion equation (ADE) with first-order reaction rates for nitrogen transformations is used. The test problem consists of a source of ammonium entering at the left border. The ammonium (NH_4^+) is degraded to NO_2^- and subsequently NO_2^- is degraded to NO_3^-. In addition to this process, the ammonium is adsorbed in the solid material. It is expected that the concentration of ammonium will decrease spatially from the origin. This decrease in ammonium will generate an increase in the NO_2^- and the degradation of it an increase in NO_3^-.

This process comprises first-order decay degradation. The solved equations are:

$$\begin{cases} R_1 \frac{\delta C_1}{\delta t} = D \frac{\delta^2 C_1}{\delta x^2} - v \frac{\delta C_1}{\delta x} - k_1 R_1 C_1 \\ R_2 \frac{\delta C_2}{\delta t} = D \frac{\delta^2 C_2}{\delta x^2} - v \frac{\delta C_2}{\delta x} + k_1 R_1 C_1 - k_2 R_2 C_2 \\ R_3 \frac{\delta C_3}{\delta t} = D \frac{\delta^2 C_3}{\delta x^2} - v \frac{\delta C_3}{\delta x} + k_2 R_2 C_2 - k_3 R_3 C_3 \end{cases} \quad \text{(B-1)}$$

where C_i is the concentration of the three components C_1 equals NH_4^+, C_2 equals NO_2^- and C_3 equals NO_3^- (mol/m^3), D is the dispersion term (m^2/s), v the pore velocity of water (m/s) q/θ, θ is the effective porosity and k_i is the degradation rate constant (1/s).

The model consists in a 220 cm length (L) 1D problem with a velocity of 0.1 cm/hr. Additional parameters are D = 0.18 cm^2/hr; k_1 = 0.01 hr^{-1}, k_2 = 0.1 hr^{-1} and k_3 = 0.

Finally, R_1 = 2, R_2 = R_3 = 1 where R_i is the retardation factor given by:

$$R_i = 1 + \frac{\rho K_d}{\theta} \quad \text{(B-2)}$$

Here, ρ is the bulk density and K_d the solid-water distribution ratio for the i^{th} chain member. A retardation factor of 2 means that the transport velocity of the solute is half of the advective velocity. On the other hand, R equal 1 means no adsorption.

Initially, the domain has no concentration of any of the transported species

$$C_i(x,0) = 0 \tag{B-3}$$

for NH_4^+, NO_2^- and NO_3^-. The boundary conditions are prescribed concentrations (Dirichlet type boundary condition) at the inlet (x=0) and outflow boundary conditions at the water outlet (x=L)

$$\begin{cases} C_1(0,t) = 1\frac{mol}{m^3}; C_2(0,t) = C_3(0,t) = 0\ \frac{mol}{m^3} \\ -\theta D_i \nabla C_i = 0\ \ at\ (L,t) \end{cases} \tag{B-4}$$

B1.2 Results

The results show that the concentration of NH_4^+ decreases with increasing depth, whereas NO_2^- and NO_3^- concentrations first increased and then decreased until they disappeared. The rate of movement of NH_4^+ is one half of that of NO_2^- or NO_3^- because of retardation effect.

Figure B-1 shows the comparison between the results of the simulation with COMSOL Multiphysics and the results detailed in the paper for a simulation time of 200 hours. The authors calculated these results using an analytical solution (Cho 1971) obtained by derivation from the equations detailed above. It can be observed that COMSOL Multiphysics can reproduce the sorption of pollutants in solids and first-order decay.

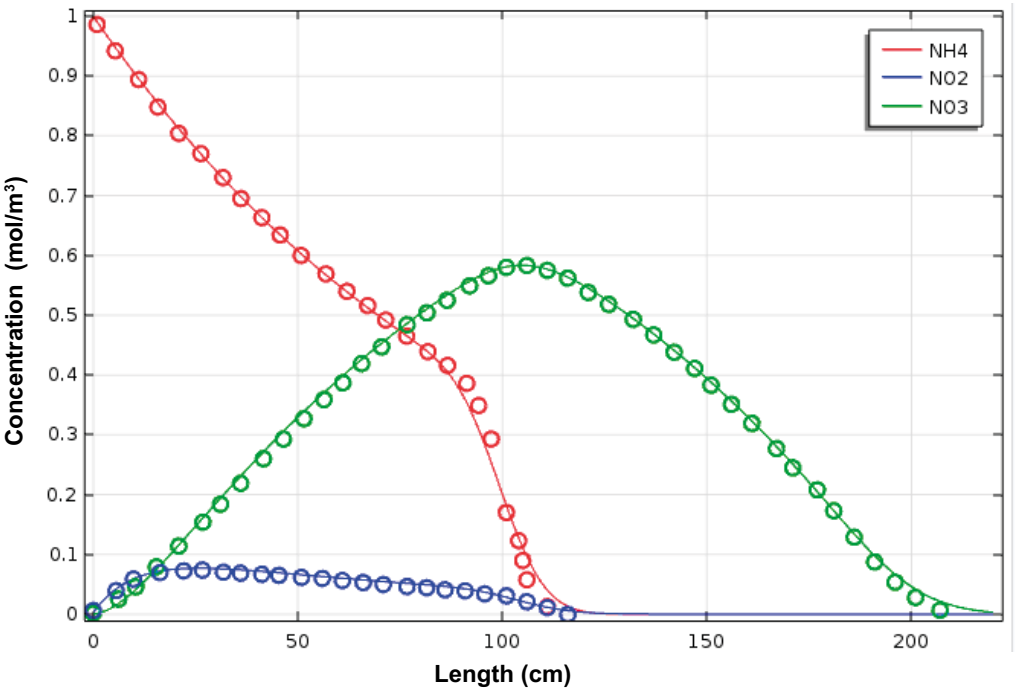

Figure B-1. *Comparison between model (lines) and reference (dots) results given in Cho et al. (1971) at t = 200 hours.*

B2 Benchmark 2. Transport of a decay chain in homogeneous porous media: analytical solutions (Bauer et al. 2001).

B2.1 Problem description

The referenced paper contains a set of analytical solutions for the transport of a general decay chain in homogeneous porous media derived with the aid of integral transforms. Steady-state flow in single and multiple porosity media are considered. The verification problem addressed here considers a series of radionuclides that are coupled by first-order decay processes forming a decay chain. Initially, the system does not contain any radionuclides. In addition, the radionuclide concentration entering the domain is zero for all, excepting C_1 which is set to 100 mmol/m^3. The solved equations proposed by the authors are:

$$\begin{cases} R_1 \frac{\delta C_1}{\delta t} = D \frac{\delta^2 C_1}{\delta x^2} - v \frac{\delta C_1}{\delta x} - k_1 R_1 C_1 \\ R_2 \frac{\delta C_2}{\delta t} = D \frac{\delta^2 C_2}{\delta x^2} - v \frac{\delta C_2}{\delta x} + k_1 R_1 C_1 - k_2 R_2 C_2 \\ R_3 \frac{\delta C_3}{\delta t} = D \frac{\delta^2 C_3}{\delta x^2} - v \frac{\delta C_3}{\delta x} + k_2 R_2 C_2 - k_3 R_3 C_3 \\ R_4 \frac{\delta C_4}{\delta t} = D \frac{\delta^2 C_4}{\delta x^2} - v \frac{\delta C_4}{\delta x} + k_3 R_3 C_3 - k_4 R_4 C_4 \end{cases} \quad \text{(B-5)}$$

where C_i is the concentration of the component i (mol/m^3), D is the dispersion term (m^2/s), v the pore velocity of water (m/s) q/θ, θ is the effective porosity and k_i is the decay constant (1/s).

The model domain is 3 000 m long (L). The problem is solved in 1D with a velocity of 1m/day. Additional parameters are D = 0.18 cm^2/hr, k_i equal to (7, 5, 4.5, 3.8) $\times 10^{-4} \times$ d^{-1} for k_1, k_2, k_3 and k_4 respectively. Finally, R equals 5.3, 1.9, 1.2 and 1.3 for R_1, R_2, R_3 and R_4, respectively where R_i is the retardation factor given by:

$$R_i = 1 + \left[\frac{1-\theta}{\theta}\right] \rho K_d \quad \text{(B-6)}$$

Here, ρ is the matrix density, θ is the porosity which is equal to 0.15 and K_d the solid-water distribution ratio for the ith chain member. K_d values can be obtained from the retardation factor resulting in 4.336×10^{-4}, 9.076×10^{-5}, 2.017×10^{-5} and 3.025×10^{-5} m^3/kg for chain members 1, 2, 3 and 4 respectively.

Initially, the domain has no concentration of any of the transported species

$$C_i(x, 0) = 0 \quad \text{(B-7)}$$

for i= 1, 2, 3 and 4.

The boundary conditions are prescribed concentration (Dirichlet type boundary condition) at the inlet (x=0) and outflow boundary condition at the water outlet (x=L)

$$\begin{cases} C_1(0,t) = 100 \frac{mmol}{m^3}; C_2(0,t) = C_3(0,t) = 0 \ \frac{mol}{m^3} \\ -\theta D_i \nabla C_i = 0 \ \ at \ (L,t) \end{cases} \quad \text{(B-8)}$$

B2.2 Results

The resulting concentration distributions for the four-member decay chain are shown in Figure B-2. One can see the concentrations of the chain members successively rising to a maximum and then declining. The maximum concentration of C_1 is at the boundary and it degrades over a short distance into C_2. In addition, the retardation of C_1 is higher than that of the other solutes. The combined effect of the low rate of propagation and decay generates this short distance degradation of C_1 into C_2. The maximum of each component is located further away from the inlet boundary depending of the position in the degradation chain. i.e. The maximum of C_3 is located further downstream than C_2.

Figure B-2 shows the comparison between the results at t = 3 000 days of the simulation with Comsol Multiphysics and the analytical solution presented in Bauer et al. (2001). It can be observed that Comsol Multiphysics is capable to reproduce the sorption of pollutants in solids and first-order decay.

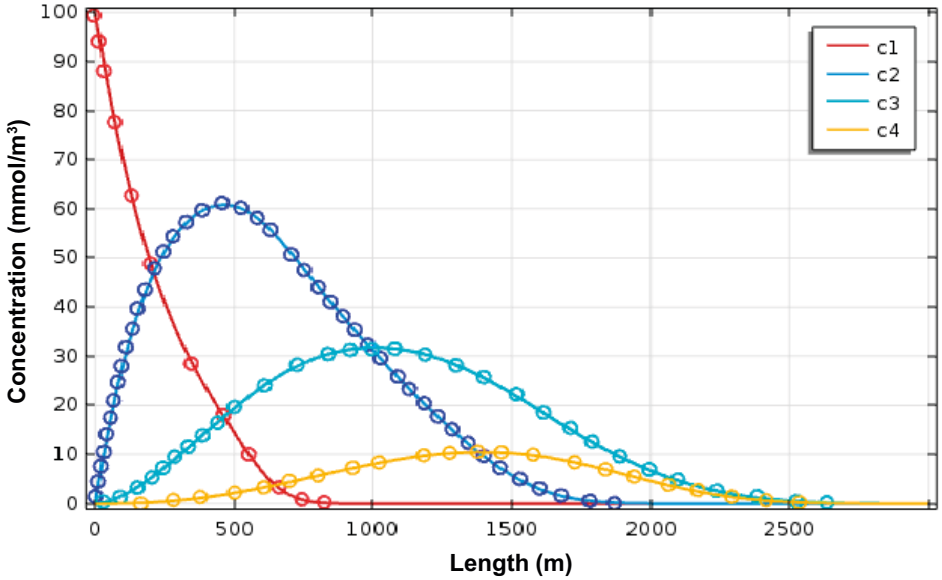

Figure B-2. *Comparison between a simulation with Comsol Multiphysics (lines) and the analytical solution (dots) proposed in Bauer et al. (2001) at t = 3 000 days.*

Arkitektkopia AB, Bromma, 2022

SKB is responsible for managing spent nuclear fuel and radioactive waste produced by the Swedish nuclear power plants such that man and the environment are protected in the near and distant future.

skb.se